FINITE ELEMENT ANALYSIS OF CONCRETE FRACTURE SPECIMENS

by

Linda D. Leibengood

David Darwin

Robert H. Dodds

A Report on Research Sponsored by

THE NATIONAL SCIENCE FOUNDATION

Research Grant PFR 79-24696

UNIVERSITY OF KANSAS

LAWRENCE, KANSAS

May 1984

50272-101

REPORT DOCUMENTATION PAGE	1. REPORT NO.	2.	3. Recipient's Accession No.

4. Title and Subtitle
Finite Element Analysis of Concrete Fracture Specimens

5. Report Date
May 1984

6.

7. Author(s)
Linda D. Leibengood, David Darwin, and Robert H. Dodds

8. Performing Organization Rept. No.
SM Report No. 11

9. Performing Organization Name and Address
University of Kansas Center for Research, Inc.
2291 Irving Hill Drive, West Campue
Lawrence, KS 66045

10. Project/Task/Work Unit No.

11. Contract(C) or Grant(G) No.
(C)
(G) NSF PFR 79-24696

12. Sponsoring Organization Name and Address
National Science Foundation
Washington, D.C. 20550

13. Type of Report & Period Covered

14.

15. Supplementary Notes

16. Abstract (Limit: 200 words)

The effects of the descending branch of the tensile stress-strain curve, fracture energy, grid refinement, and load-step size on the response of finite element models of notched concrete beams are studied. The width of the process zone and constraint of crack angles are investigated.

Nonlinearity is limited to cracking of the concrete. A limiting tensile stress criterion governs crack initiation. Concrete is represented as linear elastic prior to cracking. Cracks are modeled using a smeared representaion. The post-cracking behavior is controlled by the shape of the descending branch, fracture energy, crack angle, and element size. Unloading occurs at a slope equal to the initial modulus of the material.

Load-deflection curves and cracking patterns are used to evaluate the beam's response. Comparisons of the process zone size are made. All analyses are performed on a 200 x 200 x 800 mm concrete beam, with an initial notch length of 80 mm.

The fracture energy, tensile strength, and shape of the descending branch interact to determine the stiffness and general behavior of the specimen. The width of the process zone has a negligible influence on the beam's response. The importance of proper crack orientation is demonstrated. The model is demonstrated to be objective with respect to grid refinement and load-step size.

17. Document Analysis a. Descriptors
concrete, crack localization, cracking (fracturing), finite elements, fracture mechanics, fracture process zone, load-deflection, structural engineering, tension softening, unloading

b. Identifiers/Open-Ended Terms

c. COSATI Field/Group

18. Availability Statement	19. Security Class (This Report)	21. No. of Pages
Release unlimited	Unclassified	
	20. Security Class (This Page) Unclassified	22. Price

(See ANSI-Z39.18) *See Instructions on Reverse*

OPTIONAL FORM 272 (4-77)
(Formerly NTIS-35)
Department of Commerce

ACKNOWLEDGEMENTS

This report is based on a thesis submitted by Linda D. Leibengood to the Civil Engineering Department, University of Kansas, in partial fulfillment of the requirements for the degree of Master of Science in Civil Engineering.

The research was supported by the National Science Foundation under Research Grant PFR 79-24696. Additional support was provided by University of Kansas General Research Allocation 3131-X0-0038.

Numerical computations were performed on the Harris 500 computer at the Computer Aided Engineering Facility, School of Engineering, University of Kansas.

TABLE OF CONTENTS

LIST OF FIGURES

Chapter 1

INTRODUCTION

1.1 General

The variety of factors contributing to the nonlinear behavior of reinforced concrete make the development of a general constitutive model a difficult task. Cracking of the concrete in tension, compression softening, and the degradation of bond between the reinforcement and concrete are a few of the nonlinear behaviors that can be modeled.

The selection of a constitutive model is influenced by the type of problem being considered. If cracking dominates the response of a structure while compressive stresses remain small, the nonlinear compressive behavior of concrete may be neglected without adversely affecting predictions of structural response. Predictions may be indicative of either the microscopic or macroscopic behavior of the structure. Microscopic analyses provide evaluations of local crack response by estimating bond stresses, crack widths, dowel effects, etc. A discrete crack representation, which replicates the actual geometric discontinuity introduced by a crack, has been generally recommended for such analyses. Smeared cracking models treat cracks as stress discontinuities and less accurately model the crack opening and the high strain gradient near the crack tip. These deficiencies are less important if the analyst is primarily concerned with the general cracking patterns and overall load-deflection response of a structure. For such macroscopic analyses,

the smeared cracking model is the method of choice. Not only does the smeared model permit cracks to form and propagate in any direction, but most importantly it requires no change in topology as the analysis progresses.

The interaction of finite element modeling parameters with the constitutive model must also be understood. How sensitive is the predicted structural response to changes in grid refinement, load-step size, and element type? Systematic studies clarifying these interactions are required if an analyst is to minimize cost, while obtaining reasonable estimates of structural behavior. This study is part of a continuing effort to evaluate the effects of various modeling parameters on the predicted macroscopic response of a structure. The current work focuses on the effects of including a descending branch in the tensile stress-strain curve of concrete within a smeared crack model.

Early smeared cracking models reduced the stress transferred across a newly formed crack to zero, as soon as the limiting tensile stress or strain was attained. This sudden energy release at cracking was unrepresentative of actual material behavior and posed numerical stability problems for some solution methods. The inclusion of a descending branch in the tensile stress-strain curve provided one answer to these two distinct problems. As cracks form in a reinforced concrete structure, the reinforcing steel carries the total load at the cracks. However, the intact concrete between cracks is still capable of transferring some tensile stress. Thus, although the concrete stress is zero at a crack, the average con-

crete stress over some length is non-zero (Fig. 1.1). As additional load is applied to the structure, and a continuous distribution of cracks form, this average stress will decrease to zero. Most investigators (24,26,45) have modeled this behavior with a descending branch of the tensile stress-strain curve for concrete. In general, these more realistic models have predicted the response of actual structures better than models without a descending branch. However, the data is far from conclusive.

A number of researchers modeled the thin, simply supported two-way slab tested by McNeice (Fig. 1.2). The shape and extent of the descending branch, element type, and degree of mesh refinement affected the computed load-deflection response of the slab. In these early studies, the terminal point of the descending branch of the concrete tensile stress-strain curve was empirically determined and was held constant for changing branch shape or varying element size. To add to the confusion, some models without this "tension softening" produced load-deflection curves that closely matched the observed slab behavior. Bashur and Darwin (1), using no tension softening, represented cracking as a continuous process by numerically integrating through the depth of the slab. A good match over the entire load-deflection curve was achieved. Hand, Pecknold, and Schnobrich (19) used layered finite elements and represented the cracking as a step-by-step process. Although their predicted response deviated more from the experimental than Bashur's, their results were equally as good as those obtained with some models employing tension-softening (Fig. 1.3).

If tension-softening is to become a viable modeling option for the analyst, rational guidelines for its use are required. What shapes are most effective for the descending branch and why? How is the terminal point of the descending branch determined? In what instances is tension-softening applicable?

The existence of a descending branch for plain concrete specimens loaded in direct tension has been repeatedly verified (16,36,37). It follows that tension-softening could also be useful for modeling plain concrete structures. Should tension-softening procedures vary with the amount of reinforcement present? And if so, why?

The work of Hillerborg, Modeer, and Petersson (21) was instrumental in providing answers to some of these questions. Hillerborg, et al. applied fracture mechanics principles in developing their "fictitious crack" model. Cracks were discretely modeled, and were assumed to transfer some stress if only partially open. The area under the stress-displacement curve was shown to be equivalent to the energy required to form a unit area of crack surface, a quantity referred to as the fracture energy.

Bazant and Oh (6) extended Hillerborg, Modeer, and Petersson's work to a smeared cracking model. Triaxial stress-strain relations were derived which provide for a gradual reduction in the Poisson effect as a crack opens. Only Mode I behavior was considered, and the crack front was constrained to be one element wide. By restricting the width of the crack front, Bazant and Oh eliminated the need to consider unloading after crack formation. If

the process zone is several elements wide, cracks may form and then unload as the structure undergoes additional deformation. The assumption of a one element wide process zone simplifies the constitutive model but is not entirely realistic. In studying the cracking process in a mortar specimen, Mindess and Diamond (28) noted the formation of branching cracks. As additional load was applied, only one of the cracks continued to open and propagate. If this observed behavior is to be modeled, the width of the crack front can not be arbitrarily restricted, rather the model must permit cracks to form and then unload during subsequent loading of the structure.

The current work generalizes Bazant's approach to include unloading. Fracture specimens of plain concrete are used to study the effects of various modeling parameters on the computed macroscopic behavior of the structure. Crack patterns and load-deflection curves are used to evaluate the effects of changes in grid refinement, load-step size, fracture energy, and the shape of the descending branch. The effects of nonlinear zone size and the effects of imposing constraints on the crack angles are also examined.

1.2 Previous Work

Any model attempting to represent concrete behavior must include some method for modeling crack formation and propagation. The brittle, linear elastic, tensile response of concrete is its most distinctive and often dominant nonlinear behavior. Although the precise load at which a crack forms is often unimportant, the fact that a structure is cracked must be considered.

Two approaches have been used to represent cracks in a finite element mesh. Ngo and Scordelis (34) predefined discrete cracks in a beam in an effort to study local bond, steel, and concrete stresses. Discrete cracking models introduce a geometric discontinuity in a mesh by separating elements at the boundaries. Nilson (35) permitted crack propagation by separating common nodes of adjacent elements when the average stress exceeded the tensile strength.

Although conceptually simple, the use of discrete cracking models has been limited by the problems associated with a changing structural topology. As cracks propagate and nodes are added to a mesh, the bandwidth of the stiffness matrix increases. If the solution process is to remain efficient, some method for automatically minimizing the bandwidth or new equation solving algorithms are required. Both approaches have been used (33,42). Mufti (30,31) double noded potential crack paths. This solution is useful if crack paths are predictable or if the analyst is willing to restrict potential paths to predefined element boundaries. Saouma (42) permitted cracks to propagate in any direction by adding new elements as well as nodes to the mesh. The bandwidth was then automatically minimized.

The early problems associated with the changing topology required by discrete cracking led to the development of the smeared crack model. Rashid (39) treated concrete as a linear elastic, orthotropic material. After cracking, the material stiffness normal to the crack was eliminated. This effectively simulated the in-

troduction of many finely spaced cracks perpendicular to the direction of maximum principal stress. Smeared cracking introduces no geometric discontinuity in the mesh, only a stress discontinuity. Because of this, cracks may form in any direction while the initial grid remains unchanged.

Both the smeared and discrete models have been continually refined in attempts to more realistically represent concrete behavior. Provisions have been made for modeling aggregate-interlock and dowel action as well as post-cracking behavior. A comprehensive review of cracking models may be found in Reference 46. The remainder of this review will focus on the methods used to represent post-cracking behavior for both stress-controlled and fracture mechanics based models.

1.2.1 Stress Controlled, Smeared Cracking Models

Scanlon (44,45) introduced the use of a descending branch of the tensile stress-strain curve to account for the stress carrying capacity of the intact concrete lying between two cracks*. Finite element models composed of rectangular, layered, orthotropic plate elements were used to estimate the deflections of reinforced concrete slabs. The steel was assumed to be linear elastic and the concrete was treated as linear elastic until cracking. Cracks were forced to form vertically, and a secant solution method was em-

---

* With these early models, the use of a descending branch was referred to as "tension stiffening" rather than tension softening. The "stiffening" term was used because models with a descending branch were relatively stiffer than models with a sudden reduction in stress to zero once the tensile strength had been attained.

ployed. The two-way slab tested by McNeice (23) was modeled with the cracked concrete modulus reduced to 20, 10, 5, or 0 percent of its initial value (Fig. 1.4a). In addition, a stepped descending branch was considered (Fig. 1.4b). The slab with no tension softening significantly overestimated the observed deflections. All of Scanlon's models employing tension softening overestimated the cracking load. Beyond this point, the stepped descending branch produced the closest match with the experimental curve (Fig. 1.5)

Lin and Scordelis (26) also investigated slab and steel behavior using layered elements and tension softening. The steel was considered to be elastic-plastic, as was the concrete in compression. Again, the McNeice slab was one of the structures analyzed. Although Lin's model used more realistic material representations than Scanlon's, the two models were equally unsuccessful at predicting deflections when tension softening effects were neglected. Lin used a tangent approach and a cubic descending branch. The terminal point of the concrete tensile stress-strain curve was "intuitively assumed" to be roughly five times the strain at crack formation. The presence of tension softening influenced the structure's post-cracking response but had little effect at ultimate load (Fig. 1.6). When the terminal point of the tension softening curve was held constant and the grid refined, a stiffer slab response was predicted.

Gilbert and Warner (18) compared the convergence properties and accuracy of models utilizing different descending branch shapes and solution techniques. Slabs were modeled with layered

elements and an elastic-plastic representation for the compressive concrete was used. Preliminary analyses were conducted to calibrate the terminal points of the tension softening curves. The assumed end point of a descending branch was adjusted until reasonable agreement between predicted and experimental results was achieved. The area under the tensile stress-strain curve was then varied with an element's proximity to the steel. The McNeice slab was modeled using four different softening representations (Fig. 1.7). Three of these used a descending branch to account for the contribution of the intact concrete lying between two cracks. Scanlon's stepped secant approach, Lin's cubic descending branch, and a piecewise linear curve that contained vertical drops in stress at specified strain levels were considered. The fourth model increased the stiffness of the steel while reducing the concrete stiffness normal to the crack plane immediately to zero. The model using Lin's descending branch overestimated the slab stiffness after cracking (Fig. 1.8). Predictions from the three remaining models nicely matched the experimental results over the entire load-deflection curve. The model employing the modified steel representation required an average of 2.7 iterations/load step to achieve convergence, with Scanlon's secant approach requiring 4.6 iterations/step, the discontinuous method 8.3 iterations/step, and Lin's model 8.7 iterations/step.

Kabir (24) combined a linear tension softening representation with a more complex constitutive model to investigate the behavior of reinforced concrete slabs and shells. His model con-

sidered the effects of load history, shrinkage, and creep as well as the nonlinear compressive response of the concrete. An orthotropic, equivalent uniaxial strain model originally developed by Darwin and Pecknold (11,12) was chosen to represent the nonlinear compressive behavior. McNeice's slab was the problem selected to verify the concrete representation. The shape of the load-deflection curve generated by Kabir's model was similar to that of Lin's, with the computed response too stiff after initial cracking. Van Greunen (47,48) then extended Kabir's work to include geometric nonlinearities as well as provisions for modeling temperature and prestress effects. He elected to use Gilbert and Warner's modified steel representation after verifying that this model produced a load-deflection curve that nicely agreed with McNeice's experimental results for all load levels. The tension softening effect was an incidental consideration in both Kabir and Van Greunen's work. Consequently, their studies simply confirmed the results of other investigators but did nothing to address the many questions remaining about the phenomenon.

1.2.2 Fracture Mechanics Models

The brittle, tensile response of concrete has prompted many researchers to apply fracture mechanics methods to study concrete cracking (4,5,7,17,40,41,42). Experimental efforts have primarily focused on measuring the fracture toughness and energy release rates of paste, mortar, and concrete specimens. Notched, bend specimens 3-12 inches deep are typically used to measure the K_c

and G_c fracture parameters. For small specimens, such as the 3x4x16 inch beams tested by Kaplan (25), the stress concentration effect of the notch is negligible and the beam fails when the maximum stress on the net section reaches the modulus of rupture. However, if comparatively large specimens are tested, K_c and G_c appear to be independent of specimen geometry (43,49).

Recently, investigators have become interested in quantitatively and qualitatively describing the development of the fracture process zone. The material in the process zone is microcracked and transfers less stress at increasing levels of strain, a phenomenon referred to as softening. Studies employing various monitoring methods and specimen types have all concluded that this process zone is narrow (estimates range from several tenths of a millimeter to several millimeters) and long (9,28,29,36). It is the existence of this relatively large process zone that renders linear elastic fracture mechanics (LEFM) inapplicable to concrete structures of moderate size.

LEFM assumes the stress field near the crack tip is linear-elastic, and consequently that the stress at the crack tip is infinite. Obviously, no material is capable of sustaining infinite stress and therefore a nonlinear region develops at the crack tip. LEFM may still be applied if this region is small relative to the in-plane dimensions of a structure. Concrete structures rarely fulfill this requirement. At the same time, the nonlinear fracture theories developed for ductile materials cannot be indiscriminately applied to concrete. The fracture zone is generally small in duc-

tile materials and comparatively large in concrete. In addition, ductile materials yield and deform plastically prior to microcracking. Consequently, the boundaries of the fracture process zone and the nonlinear zone are far apart. In contrast, concrete exhibits little plastic deformation in tension and starts to soften immediately after microcracks form. Because of this, the boundaries of the concrete nonlinear and fracture process zones are virtually identical.

The early analytical models assumed that LEFM principles and methods were directly applicable to concrete. These fracture mechanics models used a critical energy release rate, G_c, or a critical stress intensity factor, K_{Ic}, as the criteria governing crack propagation (4,5,41,42). For a known crack geometry, the G or K_I associated with an assumed increase in crack length was computed. If this newly computed G exceeded G_c (or $K_I > K_{Ic}$), the crack extended (4,5,41,42). This process was repeated until the structure reached equilibrium. In these early models, no provision was made for stress transfer normal to a crack.

Rostam and Bysckov (40) and Salah El-Din and El-Adawy Nassef (41) used a discrete crack, fracture mechanics based model to compute moment-crack length relationships for singly reinforced beams. Constraints along the crack path were released as the crack extended. This solution to the changing topology problem is adequate for structures that exhibit only Mode I behavior. Both studies used constant strain triangle (CST) elements to model the crack tip.

Modeer (29) used the fictitious crack model, originally proposed by Hillerborg (20), to study crack propagation in concrete bend specimens and reinforced T-beams with predefined cracks. Four-node isoparametric and CST elements were selected for the study. Rod elements, capable of transferring axial load only, connected elements on opposite sides of a crack. Crack formation was governed by a strength criterion, while the post-cracking behavior of the rod elements was controlled by an assumed stress-displacement relationship. The area under this stress-displacement curve represented the energy required to form a unit area crack surface, a quantity referred to as the fracture energy, G_f.

Petersson (36) continued Modeer's efforts to validate the fictitious crack approach. Three-point bend specimens of varying depth and crack length were modeled and the predicted behavior was compared to reported test data and observations. Petersson's analyses indicated that both the extent of the process zone and the stress distribution within this zone were affected by the total depth of the specimen. The predicted increase in the depth of the process zone with increasing beam depth was not surprising. More interesting was the observation that the stress distribution in the fracture zone more closely matched the linear-elastic solution as the beam depth was increased. This result is consistent with the size effects documented in numerous tests. Different stress-displacement relations were used to control post-cracking behavior and were found to affect the computed macroscopic response of a specimen.

The previously mentioned studies restricted their consideration to structures containing single, predefined cracks. In addition, no attempt was made to accurately model the strain singularity at the crack tip. Saouma (42) developed a model that addressed both of these limitations. A computer procedure was developed to automatically generate singular elements around a crack tip. A special solution algorithm was then implemented to minimize the effects of new nodes and elements added to the mesh. Because the direction of crack extension was now unrestricted, both Mode I and Mode II behavior could be modeled. K_I and K_{II} were computed from the displacements of the singularity elements at the crack tip and related through interaction equations to a single K value. A crack advanced when this computed fracture parameter reached a limiting value.

Saouma's work was predicated on the assumption that LEFM was applicable to concrete. Because this is rarely the case, Catalano and Ingraffea (7) adapted the fictitious crack approach to Saouma's model. As a crack propagated, interface elements were automatically inserted in the crack. Stresses in these interface elements were regulated by an assumed stress-crack opening displacement (COD) relationship. Petersson's use of matrix methods to solve for the forces acting across a crack required that his assumed stress-displacement relationships be linearized. Catalano faced no such restriction and used a nonlinear stress-COD curve. Gerstle, et al. (17) successfully used this model to investigate the behavior of 3-point bend and tension-pull specimens.

Bazant and Cedolin (4,5) were the first to combine the simpler smeared crack representation with a fracture mechanics constitutive model. A precracked tensile panel was modeled with progressively refined grids and the load required for crack extension was computed. The crack in the unreinforced panel was modeled by a one element wide band of quadrilaterals composed of constant strain triangles. The crack advanced when the computed energy release rate exceeded a critical value. The material was then assumed to transfer no shear stress and no stress normal to the crack. A limiting tensile stress criterion has traditionally been used to predict crack extension in smeared cracking models. Bazant and Cedolin recognized that estimates of the load required for crack extension based on a strength criterion were highly dependent on the degree of mesh refinement employed. As smaller elements were used, a sharper crack was introduced in the structure and stresses in elements in front of the crack tip increased dramatically. In the limit, a model that employs a limiting tensile stress criterion predicts that any finite load is sufficient to advance the crack. In contrast, the computed energy release rate, G, converged to a constant value as the grid was refined. Energy release rates computed using the blunt band approach agreed well with values calculated using a discrete model and fell within several percent of the exact elasticity solution. The blunt crack band approach was later extended to include reinforced concrete. It was discovered that some provision for modeling bond-slip was required if G was to converge to a constant value with increasing mesh refinement. If no

bond-slip was permitted, the steel bars became progressively shorter and stiffer as the element size was reduced. In the limit, the infinitely stiff reinforcement prevented the crack from opening at all.

More recently, Bazant and Oh (6) adapted the fictitious crack approach to a smeared cracking model. Triaxial stress-strain relations providing for a gradual reduction in both the normal stress and in the Poisson effect as a crack opened were derived. No provision was made for unloading after crack formation and consequently the width of the crack front was restricted to a single element. A compliance approach was used, with only Mode I behavior considered. The post-cracking response was controlled by a linear descending branch. The softening modulus or slope of the linear descending branch was a function of the fracture energy, tensile strength, and crack band width. This model successfully matched the experimental results for fracture specimens of various sizes.

1.3 Objective and Scope

This study extends the tension softening model proposed by Bazant and Oh (6) to include unloading. The effects of various finite element modeling parameters on the computed macroscopic response of plain concrete structures are examined. The load-deflection behavior, degree of crack localization, and process zone development form the primary means of evaluating the predicted responses. Comparisons with discrete models employing identical stress-strain relationships are also made.

A limiting tensile stress criterion is used to govern crack initiation. Cracks are modeled with a smeared representation, with the tensile response assumed to be linear-elastic prior to cracking. Post-cracking behavior is controlled by the selected shape of the descending branch, the fracture energy, the element width, and the crack angle. Unloading at material points which have exceeded the maximum tensile stress occurs at a slope equal to the initial modulus of the material.

Finite element analyses are performed on 3-point bend specimens. Four descending branch shapes are considered: linear, discontinuous, Petersson's concrete, and a Dugdale model. Additional analyses are performed to evaluate the sensitivity of the specimen's response to changes in fracture energy, load-step size, and the degree of mesh refinement. Finally, the effects of varying the width of the nonlinear zone and of restricting the angles at which microcracks develop are studied.

Chapter 2

NUMERICAL PROCEDURES

2.1 General

This chapter outlines the constitutive model and solution procedures selected for use in this study. A linear elastic compressive response is assumed. In tension, the material is treated as linear elastic until microcracks form, and is then assumed to soften under increasing strain. After developing the concrete representation, the finite elements used for structural modeling are discussed. Finally, the pertinent aspects of the iterative solution process are presented. The proposed model was implemented in the POLO-FINITE system (14,15,27), which was used to generate the numerical results discussed in Chapter 3.

2.2 Concrete Material Model

The tensile cracking of the concrete is the only nonlinear behavior considered in the current study. A smeared representation is used to model the cracks, while a strength criterion controls crack formation. Bazant and Oh's (6) compliance formulation provides the basis for the constitutive model developed in this section. Bazant and Oh considered only Mode I behavior and permitted no unloading after microcrack formation. Their work will first be reviewed and then extended to include provisions for unloading.

Consider a cube of concrete, with many finely spaced microcracks normal to the first principal stress axis, subjected to principal stresses σ_1, σ_2, and σ_3 (Fig. 2.1a). The material between the microcracks is treated as linear elastic, with uncracked material properties E and ν. In contrast, the "material" within the microcracks is assumed to be in a uniaxial state of stress, with a strain that is dependent only on the stress transferred normal to the cracks. It is useful to think of the microcracks as being lumped together, with the cracked cube then consisting of two linear elastic blocks connected by ligaments having a limited stress transferring capability (Fig. 2.1b). If $\varepsilon_f = \delta_f/w$, where δ_f = the summation of the openings of the individual microcracks and w represents the width of the fracture process zone, then

$$\begin{Bmatrix} \varepsilon_1 \\ \varepsilon_2 \\ \varepsilon_3 \end{Bmatrix} = \begin{bmatrix} E^{-1} & -\nu E^{-1} & -\nu E^{-1} \\ & E^{-1} & -\nu E^{-1} \\ \text{sym} & & E^{-1} \end{bmatrix} \begin{Bmatrix} \sigma_1 \\ \sigma_2 \\ \sigma_3 \end{Bmatrix} + \begin{Bmatrix} \varepsilon_f \\ 0 \\ 0 \end{Bmatrix} \tag{2.1}$$

An expression relating σ_1 and ε_f is required. Bazant and Oh selected a linear relationship,

$$\varepsilon_f = \frac{(f_t' - \sigma_1)}{C_f} \tag{2.2}$$

where $C_f = -f_t'/\varepsilon_0$, f_t' = the concrete tensile strength, and ε_0 represents the strain at which the microcracks no longer transfer stress (Fig. 2.2a). An energy approach provides an objective means for calculating ε_0. The fracture energy, G_f, represents the work

done in generating a crack surface of unit area, i.e.,

$$G_f = w \int_0^{\varepsilon_0} \sigma_1 \, d\varepsilon_f \tag{2.3}$$

Thus,

$$\varepsilon_0 = \frac{2G_f}{wf_t'} \tag{2.4}$$

for the σ_1-ε_f curve defined by Eq. (2.2). Similarly, the area under the uniaxial stress-strain curve for the first principal stress direction must equal G_f/w (Fig. 2.2b). Consequently,

$$E_t^{-1} = E^{-1} - C_f^{-1} \tag{2.5}$$

where E_t is the slope of the descending branch. Substituting Eq. (2.2) into Eq. (2.1),

$$\begin{Bmatrix} \varepsilon_1 \\ \varepsilon_2 \\ \varepsilon_3 \end{Bmatrix} = \begin{bmatrix} E_t^{-1} & -\nu E^{-1} & -\nu E^{-1} \\ & E^{-1} & -\nu E^{-1} \\ \text{sym} & & E^{-1} \end{bmatrix} \begin{Bmatrix} \sigma_1 \\ \sigma_2 \\ \sigma_3 \end{Bmatrix} + \begin{Bmatrix} \varepsilon_0 \\ 0 \\ 0 \end{Bmatrix} \tag{2.6}$$

or

$$\begin{Bmatrix} \varepsilon_1 \\ \varepsilon_2 \\ \varepsilon_3 \end{Bmatrix} = \begin{bmatrix} \mu^{-1}E^{-1} & -\nu E^{-1} & -\nu E^{-1} \\ & E^{-1} & -\nu E^{-1} \\ \text{sym} & & E^{-1} \end{bmatrix} \begin{Bmatrix} \sigma_1 \\ \sigma_2 \\ \sigma_3 \end{Bmatrix} \tag{2.7}$$

in which

$$\mu^{-1} = \frac{E}{-E_t} \left(\frac{\varepsilon_{1u}}{\varepsilon_0 - \varepsilon_{1u}}\right) \tag{2.8}$$

Although Bazant and Oh did not specifically make the point, ε_{1u} represents the strain that would exist in the first principal direction for zero stress in the second and third principal directions. This quantity was originally defined by Darwin and Pecknold (11,12) and was termed the "equivalent uniaxial strain."

In the current model, the equivalent uniaxial strain in direction i, ε_{iu}, $= \sigma_i/E_i$, where σ_i and E_i represent the stress and secant Young's modulus for direction i, respectively.

Simplifying Eq. (2.8),

$$\mu^{-1} = E\left(\frac{\varepsilon_{1u}}{\sigma_1}\right) = \frac{E}{E_1} = \frac{E}{E_i} \tag{2.9}$$

The compliance relating ε_1 to σ_1 is then equal to the inverse of the secant modulus of the equivalent uniaxial stress-strain curve, E_1.

Now consider the case where the material unloads in the cracked direction, while σ_2 and σ_3 remain constant. Two phenomena contribute to the decrease in strain, $\Delta\varepsilon_1$, associated with the stress drop, $\Delta\sigma_1$: the intact concrete elastically unloads and the microcracks close (Fig. 2.3). Consequently, the changes in the principal strains associated with unloading are expressed by

$$\begin{Bmatrix} \Delta\varepsilon_1 \\ \Delta\varepsilon_2 \\ \Delta\varepsilon_3 \end{Bmatrix} = \begin{bmatrix} E^{-1} & -\nu E^{-1} & -\nu E^{-1} \\ & E^{-1} & -\nu E^{-1} \\ \text{sym} & & E^{-1} \end{bmatrix} \begin{Bmatrix} \Delta\sigma_1 \\ 0 \\ 0 \end{Bmatrix} + \begin{Bmatrix} \Delta\varepsilon_{cr} \\ 0 \\ 0 \end{Bmatrix} \tag{2.10}$$

where $\Delta\varepsilon_{cr}$ refers to the change in strain due to the closing of the microcracks, $\Delta\delta_f/w$. Some method for determining the amount of crack closure must be developed if this component is to be considered. For the current study, the cracks are assumed to remain open ($\Delta\varepsilon_{cr} = 0$), with all of the unloading attributed to the elastic material.

For the general unloading case,

$$E_1 = \frac{(\sigma_1 - \Delta\sigma_1)}{(\varepsilon_1 - E^{-1}\Delta\sigma_1 - \Delta\varepsilon_{cr})} \tag{2.11}$$

and

$$\begin{Bmatrix} \varepsilon_1 \\ \varepsilon_2 \\ \varepsilon_3 \end{Bmatrix} = \begin{bmatrix} E_1^{-1} & -\nu E^{-1} & -\nu E^{-1} \\ & E^{-1} & -\nu E^{-1} \\ \text{sym} & & E^{-1} \end{bmatrix} \begin{Bmatrix} \sigma_1 \\ \sigma_2 \\ \sigma_3 \end{Bmatrix} \tag{2.12}$$

Eq. (2.12) is identically equal to Eq. (2.7). Thus, the compliance matrix shown in Eq. (2.12) correctly represents all post-cracking behavior considered in this study. As Bazant and Oh noted, this formulation provides for a gradual reduction in the Poisson effect as the microcracks open. Limiting our consideration to a 2-dimensional stress state, and inverting Eq. (2.12) to put the material representation in a form suitable for use in a finite element program

$$\begin{Bmatrix} \sigma_1 \\ \sigma_2 \end{Bmatrix} = \frac{1}{1-\nu^2 E_1/E} \begin{bmatrix} E_1 & \nu E_1 \\ \text{sym} & E \end{bmatrix} \begin{Bmatrix} \varepsilon_1 \\ \varepsilon_2 \end{Bmatrix} \tag{2.13}$$

In summary, before cracking the concrete is assumed to be an isotropic, linear elastic material. For a general plane stress state, the total stresses at a Gauss point are related to the total strains computed for some applied load by the expression

$$\begin{Bmatrix} \sigma_x \\ \sigma_y \\ \tau_{xy} \end{Bmatrix} = \frac{E}{1-\nu^2} \begin{bmatrix} 1 & \nu & 0 \\ & 1 & 0 \\ \text{sym} & & (1-\nu)/2 \end{bmatrix} \begin{Bmatrix} \varepsilon_x \\ \varepsilon_y \\ \gamma_{xy} \end{Bmatrix} \tag{2.14}$$

The principal stresses are then evaluated, and microcracks will form perpendicular to the direction of the maximum principal stress when this stress exceeds the tensile strength of the concrete.

After cracking, the concrete is assumed to be an orthotropic, incrementally linear elastic material with principal axes fixed normal and parallel to the microcracks. The intact concrete between the microcracks is assumed to remain linear and elastic with material properties E and ν, while the microcracked material is assumed to be in a state of uniaxial stress. If Eq. (2.13) is modified to permit the formation of two orthogonal cracks, the expression relating total stresses and strains in the cracked coordinate system becomes

$$\begin{Bmatrix} \sigma_1 \\ \sigma_2 \\ \tau_{12} \end{Bmatrix} = \frac{1}{1-\nu^2 E_1 E_2/E^2} \begin{bmatrix} E_1 & \nu E_1 E_2 E^{-1} & 0 \\ & E_2 & 0 \\ \text{sym} & & (1-\nu^2 E_1 E_2/E^2)\beta G \end{bmatrix} \begin{Bmatrix} \varepsilon_1 \\ \varepsilon_2 \\ \gamma_{12} \end{Bmatrix} \quad (2.15)$$

in which E_1 and E_2 represent the secant moduli of the equivalent uniaxial stress-strain curves for the directions normal to the first and second cracks, β = a shear stiffness retention factor, $G = 0.5E/(1+\nu)$, and subscripts 1 and 2 refer to the material or cracked axes.

The inclusion of the βG term can serve to model aggregate interlock effects by permitting shear transfer along the crack face. Because some shear stiffness is retained, the principal stress and strain axes will rotate as additional load is applied. A β value of zero is used in the current study. As a result, no stress transfer is permitted along a crack, and the principal stress axes are stationary following crack initiation.

2.3 Finite Elements

Linear isoparametric (4-node) elements are used to model all the concrete specimens considered in this study. Isoparametric elements have several advantages over the simpler constant strain triangle (CST) elements commonly used in finite element analyses of concrete structures. Fewer elements are required to obtain accurate solutions, thereby reducing the preparation and computation time required to solve a problem. Nayak (32) estimated that for a 2-D linear analysis, one 4-node element is equivalent to eight CST's. In addition, isoparametric elements distribute the residual loads over a larger portion of the structure. This may accelerate the solution process by reducing the number of iterations required to reach equilibrium.

A Gauss numerical integration procedure is used to evaluate the stiffness of isoparametric elements. These Gauss points are optimum locations for computing stresses and strains. A four point quadrature rule is sufficient to exactly compute the stiffness of a 4-node element (Fig. 2.4) in linear analysis, while a nine point rule is required to exactly integrate the 8-node (quadratic) element (Fig. 2.5). Four point quadrature represents reduced integration for the 8-node element and has been successfully employed in many nonlinear plasticity analyses. A complete discussion of the isoparametric formulation can be found in Ref. 51.

Dodds, et al. (13) discovered that the stiffness characteristics of quadratic elements integrated using a four point rule make them unsuitable for use in smeared cracking models. The eigenvalue of a stiffness matrix is proportional to the energy generated when an element is deformed in the shape of the corresponding eigenvector. Rigid body motions generate no strain energy and consequently have zero eigenvalues. Each time a crack forms in a quadratic element integrated using four point quadrature, an additional zero eigenvalue is generated. If these new zero energy modes are activated as additional load is applied to the structure, the computed behavior becomes unpredictable. An additional zero eigenvalue is generated for the 4-node element only when all Gauss points in an element crack at precisely the same angle. New zero energy modes are introduced for the fully integrated 8-node element when more than six of the element's nine Gauss points crack at identical angles. Cracks forming in an element generally have slightly different orientations. Because of this, either the 4-node or fully integrated 8-node isoparametric elements may be confidently used in combination with a smeared cracking model. Only the four-node element is used in this study.

2.4 Solution Procedures

2.4.1 General

A Newton-Raphson procedure is used to solve the set of nonlinear equilibrium equations. Load is applied to the structure in a series of steps consisting of imposed nodal displacements. The

equilibrium equations are assumed to be linear within an iteration and are solved for the incremental nodal displacements. Strains and stresses at sampling points in the elements are then computed based on the estimated nodal displacements. The stresses are corrected to reflect any cracking or softening of the material and the tangent stiffness matrix at each Gauss point is recomputed as required. The difference between the load required to maintain the structure in its current deformed shape and the total applied load constitutes the residual load. The structure stiffness matrix is reassembled prior to the application of the residual forces. The solution then iterates until the residual loads fall below some prescribed tolerance. In this study, total equilibrium conditions are used in computing the residual forces. Because of this, no errors accumulate from one step to the next.

The user may modify the standard Newton-Raphson procedure by electing to reconstruct the structure stiffness only for selected iterations. If the stiffness matrix is updated frequently, the residual forces are more accurately distributed and the number of iterations required for convergence is reduced. Stiffness updates are expensive. Consequently, the analyst attempts to optimize the frequency of the updates with the number of additional iterations required for convergence. Cedolin and Dei Poli (8) found that stiffness updates were needed before each iteration, if a convergent solution to some cracking problems was to be obtained. For this study, stiffness updates were performed before each load step and each iteration.

The major computational steps required to analyze a structure for each increment of applied load are outlined below.

1) Compute the incremental equivalent nodal loads, $\{\Delta P\}$, associated with the applied load increment for the step. For the first iteration of a load step, set the residual nodal loads, $\{R\}$, equal to the incremental applied loads, $\{R\} = \{\Delta P\}$.

2) Update the total nodal loads applied to the structure, $\{P_{NEW}\} = \{P_{OLD}\} + \{\Delta P\}$.

3) Using the current material properties, compute the tangent constitutive matrix, $[D_T]$, for each Gauss point in an element.

4) Using the updated $[D_T]$ matrices, recompute the stiffness matrices for elements that are newly cracked, or initially unloading or reloading. Assemble and triangulate the structure stiffness matrix, $[K_T]$.

5) Use the triangulated stiffness to solve for the incremental nodal displacements, $\{\Delta U\} = [K_T]^{-1}\{R\}$. Update the total nodal displacements, $\{U_{NEW}\} = \{U_{OLD}\} + \{\Delta U\}$.

6) Evaluate the incremental and total strains at each Gauss point in the structure.

7) Using the current material properties, compute the secant constitutive matrix, $[D_S]$, for each Gauss point in an element. Update the total stresses at each Gauss point based on the total strains and loading history, $\{\sigma\} = [D_S]\{\varepsilon\}$.

8) Compute the internal nodal forces, $\{IF\}$, necessary to maintain each element in its deformed configuration, $\{IF\} = \int_V [B^T]\{\sigma\}\, dv$. Assemble these into a structural nodal vector, $\{IF_S\}$.

9) Evaluate the residual nodal load vector for the structure, $\{R\} = \{P_{NEW}\} - \{IF_S\}$

10) Apply the prescribed convergence tests to determine if the residual loads have reached an acceptable level. If the convergence criteria are met, go to 1 and repeat the process for the next increment of applied load; if not, go to 3 and begin the next iteration.

The criteria used to terminate the solution process in this study,

$$||\{R\}|| < 0.001 * ||\{P\}|| \tag{2.16}$$

is an average measure of the equilibrium of the structure. $\{R\}$ represents the residual load vector and $\{P\}$ refers to the applied total load vector. Eq. (2.16) compares the Euclidean norms (square root of the sum of the squares) of the residual and applied load vectors. This convergence test forces the solution to iterate until no additional cracking or new unloading occurs.

2.4.2 Special Techniques

Special techniques used to implement the formulation outlined in Section 2.2 will be discussed in this section. First, the procedure used to determine the terminal point of the equivalent uniaxial stress-strain curve will be outlined. Next, the methods used to incorporate unloading in the model will be treated. Finally, the use of the tangent rather than the secant structure stiffness matrix for estimating nodal displacements will be discussed.

As indicated by Eq. (2.3), ε_0, the terminal point of the tensile stress-strain curve, is a function of f_t', E, the assumed descending branch shape and the width of the crack front. The concrete tensile strength, Young's modulus, and the shape of the descending branch are input by the user for each element. Bazant and Oh used the expression

$$w = \frac{h}{\cos \alpha} \tag{2.17}$$

to compute the crack front width, w. α represents the crack angle, which must be less than or equal to 45 degrees. All elements are assumed to be square, with a width of h. The relationship used in this study,

$$w = \frac{h}{\max(\sin \alpha, \cos \alpha)} \tag{2.18}$$

simply modifies Bazant's expression to permit consideration of any crack angle. Note that the minimum crack front is one element wide. This assumption is reasonable for the linear, isoparametric elements used for this study. The four-node element generally cracks at all four Gauss points or doesn't crack at all. Cracking in an element relieves stresses in adjacent elements but not stresses within the element itself.

From another perspective, w represents the width of the region into which the crack localizes. If several adjacent elements crack, some of the elements may unload as the structure undergoes additional deformation. The crack front then refers to the width of

those elements that have remained on the envelope of the equivalent uniaxial stress-strain curve, i.e. that have not unloaded. For the problems considered in this study, the crack localized into a single element. Consequently, the computation of w based on the width of a single element is justified.

With an expression to compute w, all of the pieces necessary to evaluate ε_0 are present. ε_0 is computed when microcracks first form at a point. The determination of the terminal point completes the definition of the equivalent uniaxial stress-strain curve. The equivalent uniaxial strain perpendicular to the crack, ε_{iu}, is set equal to the maximum principal stress/E, and the stress transferred normal to the crack, σ_i, is then computed from the newly defined curve. The new secant modulus normal to the crack, E_i, is then simply $\sigma_i/\varepsilon_{iu}$.

After cracking, the material axes remain fixed perpendicular and parallel to the crack. The stresses in material coordinates are computed using Eq. (2.15), and the current equivalent uniaxial strains are evaluated. The stress normal to the crack is then corrected based on the total equivalent uniaxial strain. A determination as to whether or not the material normal to the crack is unloading must be made at this time. For this study, the material was assumed to unload when,

$$\Delta\varepsilon_{iu} = \varepsilon_{iu}^{new} - \varepsilon_{iu}^{beg} < 0 \qquad (2.19)$$

ε_{iu}^{new} and ε_{iu}^{beg} refer to the total equivalent uniaxial strains for the current iteration and the value at the start of the load step, respectively.

When a point first microcracks, ε_{iu}^{beg} is initialized to the peak equivalent uniaxial strain. A cumulative rather than an incremental value of $\Delta\varepsilon_{iu}$ is used in an effort to distinguish between real and spurious unloading. The signs of the incremental values of $\Delta\varepsilon_{iu}$ often oscillate due to the corrective iterations to remove residual loads. Thus, although $\Delta\varepsilon_{iu}$ may be negative for an iteration, the total change in the equivalent uniaxial strain for the load step may be positive. If this is the case, it is incorrect to assume that the material unloads.

If the material is unloading, from what point on the envelope does this unloading occur? Consider two adjacent elements, one microcracked, and one that is still linear elastic (Fig. 2.6a). For simplicity, assume the elements have a single Gauss point. At the end of the previous load step, the microcracks in element A were opening. A small increment of load is then applied to the structure. On iteration one, the microcracks in A continue to open, while in B the tensile strength of the concrete is exceeded and new microcracks form (Fig. 2.6a). The equivalent uniaxial stress-strain curves for the directions normal to the cracks are shown for both elements in Fig. 2.6b. ε^1 indicates the equivalent uniaxial strain for iteration one and σ^1 the stress assumed to be transferred across the crack. The residual loads are applied to the structure and new equivalent uniaxial strains are computed. These new equivalent

uniaxial strains are labeled as ε^2 on the curves in Fig. 2.6b. Note that the microcracks in element B are opening while the material in element A is unloading. If just enough load to microcrack element B had been applied, ε^1 for element A would be reduced and would represent the correct point on the envelope from which to unload, ε_u. As indicated in the figure, ε_u lies between the equivalent uniaxial strains computed for the previous and current iterations, but lies closer to ε^1. If instead, a larger increment of load is applied, the maximum principal stress computed for element B greatly exceeds the concrete tensile strength (Fig. 2.6c). ε_u for element A again lies between ε^1 and ε^2 but in this instance lies closer to ε^2. On the average,

$$\varepsilon_{env} = \frac{\varepsilon_{i-1} + \varepsilon_i}{2} \tag{2.20}$$

in which ε_{env} is the envelope strain from which unloading occurs and ε_i and ε_{i-1} are the equivalent uniaxial strains for the current and previous iterations. If ε_{env} is less than the equivalent uniaxial strain at the beginning of the load step, ε_{env} is set equal to ε_{iu}^{beg}.

As mentioned in Section 2.4, the tangent stiffness matrix is used to estimate the nodal displacements for the structure, while a secant constitutive matrix, $[D_S]$, is used to relate the total strains to the total stresses at individual Gauss points.

One accepted form of the tangent [D] matrix for an in-

crementally linear, orthotropic material is

$$\begin{Bmatrix} d\sigma_1 \\ d\sigma_2 \\ d\tau_{12} \end{Bmatrix} = \frac{1}{1-\nu^2} \begin{bmatrix} E_1 & \nu\sqrt{E_1 E_2} & 0 \\ & E_2 & 0 \\ \text{sym} & & (1-\nu^2)\beta G \end{bmatrix} \begin{Bmatrix} d\varepsilon_1 \\ d\varepsilon_2 \\ d\gamma_{12} \end{Bmatrix} \qquad (2.21)$$

in which $d\varepsilon_1$, $d\varepsilon_2$, and $d\gamma_{12}$ represent the differential strains, $d\sigma_1$, $d\sigma_2$, and $d\tau_{12}$ represent the differential stresses, and E_1 and E_2 represent the tangent stiffnesses in the direction of the material axes (11,12). To prevent stability problems, β in Eq. (2.21) is set to 0.001.

Because the concrete is assumed to be linear elastic in both tension and compression, the secant and tangent [D] matrices are identical prior to cracking. After cracking, the tangent modulus of elasticity is negative. The use of a negative modulus may produce numerical problems or incorrect results. To avoid this, the tangent modulus normal to the cracks is set to zero when microcracks form. If the material subsequently unloads, the modulus is reset to its initial elastic value.

By using the tangent rather than the secant [D] matrix to compute the element stiffnesses, the number of iterations required for convergence is reduced. In addition, far fewer element stiffnesses need to be recomputed. $[D_S]$ continually changes while $[D_T]$ changes only when a point initially cracks, unloads, or reloads.

Chapter 3

NUMERICAL RESULTS AND DISCUSSION

3.1 General

A numerical study was conducted to evaluate the effects of various modeling parameters on the computed response of concrete fracture specimens. All analyses were performed on a notched beam, using the constitutive model and solution procedures outlined in Chapter 2.

Four different tension softening representations were considered. The assumed shapes of the descending branch of the tensile stress-strain curve are shown in Fig. 3.1 and are referred to by the terms linear, bilinear, discontinuous, and Dugdale in later discussions. These branch shapes match the actual behavior of concrete to varying degrees. The bilinear model most accurately represents the general shape of a concrete tensile stress-strain curve, while the Dugdale model is more appropriate to represent the behavior of ductile, yielding materials.

In addition to studying the effects of the assumed tension softening curve, variations in response associated with different fracture energies, degrees of grid refinement, and load-step size were investigated. Analyses were also performed to evaluate the effects of constraints imposed on the permitted crack angle and the effects of nonlinear zone size.

This chapter first discusses the general procedures used in modeling the 3-point bend specimen. The numerical results are then presented and models compared on the basis of load-deflection behavior, degree of crack localization, and process zone length. Comparisons are also made to a discrete crack model that uses identical stress-strain relationships. Finally, the implications of these findings for general structural modeling are discussed.

3.2 Notched Beam Properties and Modeling Details

A notched bend specimen, originally analyzed by Petersson (36), was selected for study. The beam was 200 mm (7.9 in.) wide, 200 mm (7.9 in.) deep, and 800 mm (31.5 in.) long, with a notch length of 80 mm (3.15 in.). The fracture energy was assumed to be 100 N/m (0.57 lb/in), the tensile strength 4 MPa (0.58 ksi), Young's modulus 40000 MPa (5,800 ksi), and Poisson's ratio 0.2. Additional analyses were performed using the discontinuous tension softening model and fracture energy values of 50 N/m (0.29 lb/in) and 200 N/m (1.14 lb/in).

The specimen was modeled as shown in Fig. 3.2. The hatched area represents the nonlinear part of the model. This nonlinear region is isolated and enlarged in Fig. 3.3. The linear elastic portions of the beam were substructured and condensed to reduce computation time.

It has been argued (2,3,6) that, due to stability considerations, a crack will localize into a single element. To test this statement, as well as to the verify the unloading portions of

the constitutive model, a three element wide nonlinear zone was used in the majority of the analyses. Meshes with nonlinear regions one element wide were also considered. Square elements were used throughout the nonlinear zone to eliminate any potential bias due to finite element shape. Two degrees of mesh refinement were considered: 40 and 160 elements through the depth. In all cases, a notch was introduced by "precracking" elements, that is reducing to zero both the tangent and secant moduli of elasticity normal to the crack. The geometric result is a crack with an initially blunt notch tip of diameter equal to one element width and a length equal to the specified number of elements.

Load was applied to the structure by imposing displacements at the nodes indicated in Fig. 3.2. The element directly below these nodes was linear. Unless otherwise noted, all load steps taken in an analysis are shown on the load-deflection curves.

It is useful at this point to explain the notation adopted to describe the results of the numerical study. A Gauss point is considered to reside in the fracture process zone once the strain associated with the peak tensile stress has been exceeded. Thereafter, the secant modulus of elasticity is always less than Young's modulus. Material within the process zone unloads when the equivalent uniaxial strain normal to the microcracked direction decreases as additional load is applied to the structure.

When crack patterns are presented, only the portion of the nonlinear zone indicated in Fig. 3.3 is reproduced. On these figures, a dot at a Gauss point location symbolizes a microcracked

point that is unloading. A "C" denotes a point where the stress transferred across the microcracks is compressive. Points still capable of carrying some stress perpendicular to the microcracked direction are represented by thin solid lines. Thick solid lines indicate cracks that are no longer capable of transferring any normal stress, i.e. $\varepsilon > \varepsilon_0$. In all cases, the microcrack angles are measured from the horizontal axis.

3.3 Numerical Examples

3.3.1 Effect of Tension Softening Representation

Analyses were conducted to compare the performance of the linear, bilinear, discontinuous, and Dugdale tension softening representations. A grid with 40 elements through the depth and a three element wide nonlinear zone was used for each analysis. All elements in the nonlinear region were 5 mm square. The load-deflection curves for the four tension softening models (each with the same fracture energy) are shown in Fig. 3.4. The process zone lengths (measured from the initial notch tip) at selected displacements are compared in Fig. 3.5.

Both the peak load and the imposed displacement corresponding to the peak load vary with the assumed descending branch shape. The discontinuous model exhibits the most flexible behavior on the ascending branch of the load-deflection curve, while the bilinear, linear and Dugdale models produce successively stiffer responses.

The stiffnesses (both secant and tangent) of the structure are a function of the process zone length. As shown in Fig. 3.5, for any displacement greater than 20 μm, the process zone is longest in the discontinuous model. The process zones in the remaining three models are identical in length until the imposed displacement reaches 60 μm. Beyond this point, for any displacement, the process zone becomes progressively shorter in the bilinear, linear, and Dugdale models. Note that this sequence - discontinuous, bilinear, linear, and Dugdale - corresponds to the order of the most flexible to the stiffest specimen.

The process zone lengths and load-deflection curves for the bilinear, linear, and discontinuous models are similar at two stages in the loading process, when the structure is initially loaded and when the imposed displacement reaches 180 μm. At a displacement of 180 μm, the remaining ligament is small and the compression zone beneath the applied load slows the extension of the process zone. In general, the smaller the differences in process zone lengths, the smaller the variations in the load predictions for the four models.

Although the predicted load-deflection response of the beam varies with the assumed descending branch shape, several common trends in the cracking behavior are observed. The crack patterns for the four models are presented in Fig. 3.6-3.9. Patterns for five stages in the loading process are shown. In all four models, elements outside the center band crack. Generally, these side elements unload almost immediately and the crack localizes into the center column of elements.

If a crack is to localize, the model must not only permit unloading but also provide for stress relief, i.e. a drop in stress with increasing strain that allows adjacent elements to unload. In particular, the Dugdale representation maintains the stress transferred normal to the microcracks at the peak tensile stress until the terminal strain, ε_0, is exceeded. Thus, no relief is provided to the side elements and only isolated points unload before the terminal strain is exceeded in points at the base of the process zone (Fig. 3.9).

For the discontinuous model, the stress transferred across the microcracks drops to 60% of the peak value at the instant microcracks form. This sudden decrease in stress prevents cracking in adjacent elements (Fig. 3.8). The process zone is initially 5 mm wide, and only broadens to 10 mm when the vertical extent of the zone exceeds 52.5 mm. When the linear, bilinear, or Dugdale models are considered, the process zone widens to encompass the entire width of the nonlinear region (15 mm).

For each tension softening representation, the width of the process zone is affected by the size of the load steps selected for the analysis. If smaller steps are taken, the center microcracks may open and the side elements unload without first reaching the peak stress. The interaction between the tension softening model, load-step size, and the process zone width is discussed in Section 3.3.4.

For the Mode I problem considered, the microcracks were expected to form almost vertically. However, because the sampling points in the linear isoparametric elements are located off center, small shear stresses exist at the Gauss points. The presence of these small shear stresses produces principal stress axes that have an oblique orientation. Therefore, the Gauss points cracked at angles ranging from 65 to 80 degrees as the process zone grew to a depth of 25 mm.

The cracking behavior of the linear model (Fig. 3.6) is typical of all four models. As the process zone extends upward from the base of the notch, microcracks form at angles of 81.3, 69.8, 81.5, 68.6, and 81.3 degrees along a line 1.44 mm to the left or right of the beam centerline. The inability of the 4-node element to accurately model the shear stress distribution in the beam produces the alternating crack angles.

In addition to the cracking and unloading of side elements, and the formation of microcracks at alternating angles, two other cracking phenomena are common to all four models. First, as the process zone extends vertically, the microcrack angles become progressively flatter. Secondly, at some distance behind the tip of the process zone, transverse microcracks develop when the strain corresponding to the peak tensile stress is slightly exceeded. The distance between the tip of the process zone and the region where these transverse or "secondary" cracks are initiated decreases as the process zone lengthens. Both of these phenomena are products of the stress gradients that exist near crack tips. It is useful at this point to review the characteristics of this stress field.

Irwin (22) used methods developed by Westergard (50) to derive expressions describing the stress field near a sharp crack tip subjected to Mode I deformation. If σ_x and σ_y represent the stresses in directions perpendicular and parallel to the crack, respectively, then

$$\sigma_x = \frac{K_I}{(2\pi r)^{\frac{1}{2}}} \cos\frac{\theta}{2}\left[1 + \sin\frac{\theta}{2}\sin\frac{3\theta}{2}\right] \tag{3.1}$$

and

$$\sigma_y = \frac{K_I}{(2\pi r)^{\frac{1}{2}}} \cos\frac{\theta}{2}\left[1 - \sin\frac{\theta}{2}\sin\frac{3\theta}{2}\right] \tag{3.2}$$

where K_I = the stress intensity factor and r and θ are the polar coordinates describing the location of a point in the stress field relative to the crack tip (Fig. 3.10). From Eq. (3.1) and (3.2), it is clear that points near the crack tip are subjected to biaxial tension. As r approaches zero, both σ_x and σ_y approach infinity. When K_I and r are held constant, the variations in σ_x and σ_y as a function of θ are shown in Fig. 3.11. Note that the two stresses are exactly equal along a line directly above the crack tip. The difference between σ_x and σ_y reaches a maximum when θ equals 69 degrees. At this point, σ_y is 29% of σ_x.

Unlike Irwin's sharp crack, the crack in the notched beam is blunt. Also, only the tip of the process zone and the location of Gauss points transferring zero stress are well defined. At any point in the loading process, the location of the "effective" crack tip between the two locations is not known. Values of θ and r for a

specific Gauss point cannot be assigned for use in Eq. (3.1) and (3.2). Because of this, Irwin's expressions simply provide an indication of the qualitative response to be expected in the beam.

Clearly, σ_y near the effective crack tip is not infinite. However, stresses in the vertical as well as the horizontal direction are elevated. Based on this, development of the transverse cracks throughout the center column is expected.

As the remaining ligament is reduced, the distance between the effective crack tip and the Gauss points at the tip of the process zone decreases. σ_x and σ_y become nearly equal as the crack more nearly resembles the idealized sharp crack. This equalizing of the vertical and horizontal stresses has two effects on the cracking behavior of the notched beam. When small shear stresses are combined with nearly equal stresses in the x and y directions, the principal axes deviate greatly from the structure's x-y coordinate axes. The resulting primary microcracks form at comparatively flat angles. When the remaining ligament has been reduced to 35 mm, primary microcracks at the process zone tip form at angles of 40-50 degrees. Because σ_y is nearly equal to σ_x, little additional load is required to raise σ_y to the tensile strength. Thus, the transverse cracks form quickly and the lag between the process zone tip and the region where transverse cracks develop is reduced.

Transverse cracks have been observed experimentally, at the University of Kansas (10), in slices of cement paste specimens that were dried, fractured, and then viewed with a scanning electron microscope. The transverse crack widths typically ranged from 0.3

to 3 μm when the paste specimens were not loaded. If the slices were removed from specimens that had been subjected to compressive load, the observed crack widths generally varied from 0.6 to 7 μm, but ranged as high as 10 μm. To put the size of these cracks in perspective, Petersson (36) noted that cracks first become visible to the naked eye when they reach widths of 25 to 50 μm.

The constitutive model discussed in Chapter 2 provides a means for estimating crack widths in elements containing smeared cracks. Restating Eq. (2.12), the total strain normal to the secondary microcracks, ε_2, is simply

$$\varepsilon_2 = \sigma_2 E_2^{-1} - \nu\sigma_1 E^{-1} \tag{3.3}$$

where σ_2 and σ_1 are the stresses normal and parallel to the second microcracked direction respectively, E_2 = the secant modulus of the equivalent uniaxial stress-strain curve for the direction perpendicular to the primary microcracks, E = Young's modulus, and ν = Poisson's ratio. The strain in the linear elastic or intact portions of the concrete, ε_{IN}, is known.

$$\varepsilon_{IN} = \sigma_2 E^{-1} - \nu\sigma_1 E^{-1} \tag{3.4}$$

The difference between Eq. (3.3) and (3.4) represents the strain contribution of the microcracked material. Multiplying by the gage length, w, the crack width C_w, becomes

$$C_w = w \times (E_2^{-1} - E^{-1})\, \sigma_2 \tag{3.5}$$

The transverse crack widths computed for the various tension softening models typically vary from 0.1 to 9 μm (12.5 μm maximum), when the imposed displacement on the beam reaches 180 μm. These values are consistent with the experimental findings mentioned above. Although they may initially unload, the secondary cracks throughout the center band open when the displacement imposed on the beam exceeds 110 μm. At no point in the process zone do the cracks form exactly vertically. As mentioned earlier, this deviation from the vertical increases as the process zone lengthens. Since a realistic vertical crack was not introduced in the specimen, the primary as well as the secondary cracks may open in an attempt to simulate a single, more nearly vertical crack.

It should be noted that points at the base of the process zone completely lose their ability to transfer normal stress only in the Dugdale and linear models, for the loading levels considered. Under additional displacement, the terminal strain at points in the discontinuous and bilinear models would also be exceeded. Only with the Dugdale model is the peak of the load-deflection curve coincident with the total loss of normal stiffness in points at the base of the process zone. When the terminal strain is reached at additional points, the descending branch of the Dugdale load-deflection curve drops vertically.

3.3.2 Discrete vs. Smeared Crack Representation

The fracture specimen examined in this study was originally analyzed by Petersson (36). He used a discrete crack model and grids having 40 elements through the depth to study the notched beam. Different stress-displacement relationships controlling the post-peak tensile response were considered. The linear, bilinear, and Dugdale analyses discussed in Section 3.3.1 replicated three of Petersson's analyses. The current smeared crack models employed equally refined meshes and identical tensile stress-strain relationships to those used by Petersson. The load-deflection responses of smeared and discrete models using the same tension softening representations are compared in Fig. 3.12-3.14.

In all cases, a good match between the smeared and discrete models is achieved on the ascending branch of the load-deflection curve. The peak loads predicted by the fictitious crack model range from 97-99% of the corresponding smeared crack values. The descending branches for each of the smeared crack analyses are stiffer than their discrete crack counterparts. However, the shapes of the two linear and two bilinear descending branches are similar.

Two differences exist between the discrete and smeared models that may account for the discrepancies observed in the descending branch responses. In the smeared model, elements outside the center column or band are permitted to crack. Also, the discrete cracks are constrained to form vertically at the specimen midline, while the smeared microcracks develop at unrestricted angles slightly off the beam centerline.

A number of modeling schemes were developed to determine the importance of these differences. First, a model having a one element wide nonlinear zone, rather than the three element wide band, was studied. The restriction of microcrack development to the center column permitted the effects of cracking in the side elements to be examined. Next, a model was developed which constrained cracks to form vertically and horizontally. Again, cracking was limited to the center band of elements. This analysis isolated the influence of the microcrack angles on the predicted structural response. Finally, the transverse cracks were prevented from forming in a model having unconstrained cracks and a nonlinear zone one element wide. This allowed the role of the transverse cracks to be studied. All analyses discussed in this section were performed on specimens modeled with 40 elements through the depth and a linear tension softening representation. The linear tension softening model has been used by previous investigators (6,36) and permits additional comparisons to be made between models employing discrete and smeared crack representations. The load-deflection behavior of the various models are presented in Fig. 3.15. The fracture process zone lengths at selected displacements are compared in Fig. 3.16.

Load-deflection curve "A", in Fig. 3.15, was produced by Petersson's discrete crack model. The finite element results, symbolized by squares, closely match Petersson's results and were obtained by using a model with a one element wide nonlinear zone and cracks constrained to form vertically and horizontally. Curves "B" and "C" were generated using models with three element and one element wide nonlinear zones and unconstrained microcrack angles.

Load-deflection curve "D", having no descending branch, was generated by a model which prohibited secondary microcrack formation. No constraint was placed on the primary crack angles and a nonlinear zone one element wide was used.

The load-deflection curves for the linear models with three and one element wide nonlinear zones and unconstrained cracks are virtually identical until the imposed displacement reaches 130 μm. For larger displacements, the model with the narrower nonlinear zone is slightly stiffer. At imposed displacements greater than 120 μm, the vertical extent of the process zone is greater in the side elements than in the center column (Fig. 3.6). When the nonlinear zone is restricted to a single element, the stresses in the side elements still exceed the concrete tensile strength. However, because these side elements are prevented from cracking, the process zone can not grow until points in the center band microcrack. This produces a slightly stiffer structure.

The similar responses of the models having one and three element wide nonlinear zones were expected. As noted in Section 3.3.1, the side elements crack and unload almost immediately. In the case of the linear model, Gauss points in the side elements consistently traverse less than 0.4% of the distance from the peak to the terminal strain before unloading. Consequently, virtually no energy is absorbed by the formation of these additional microcracks. Because the side elements are able to unload after microcracking, the width of the nonlinear region has a negligible effect on the overall response of the specimen. In contrast, the angles at which

microcracks develop clearly influence the behavior of the beam. When the primary cracks are constrained to form vertically, the descending branch of the load-deflection curve drops to coincide with Petersson's linear results.

When the process zone lengths for the different models are examined (Fig. 3.16), it is evident that differences in crack angle, not differences in process zone length, are responsible for the change in stiffness of the descending branch. The process zones in the unconstrained models with three and one element wide nonlinear zones, and in the model with constrained cracks differ by no more than 5 mm (the width of a single element) at any value of imposed displacement. Although the process zone lengths are essentially the same, the loads that the beams carry may vary substantially. At a displacement of 150 μm, the process zone lengths in the two models with unconstrained cracks differ by 2.5 mm. Although the process zone is 3.6% longer in the specimen modeled with a nonlinear zone three elements wide, the loads carried by the two beams differ by less than 0.6%. At the same time, the process zones in the model with constrained cracks and in the model with unconstrained cracks and the wider nonlinear zone also differ by 2.5 mm, a difference of 3.4%. In this case, the model with the cracks constrained to form vertically and horizontally supports 17% less load than the specimen with unconstrained cracks. This qualitative behavior is typical for large displacements.

The crack patterns for the three models are presented in Fig. 3.6, 3.17, and 3.18. The microcrack angles and general cracking behavior of the two models having unconstrained cracks but nonlinear regions of different width are very similar. In both cases, the transverse microcracks form and open to widths of 1 to 12 μm at an imposed displacement of 180 μm.

Two differences in the response of beams having constrained and unconstrained cracks are readily apparent. First, no transverse cracks develop at process zone lengths less than 15 mm in the vertical crack model; and second, once transverse cracks form, they unload rather than open. The behavior of these horizontal, secondary microcracks supports the theory that both the primary and secondary cracks in the unconstrained model open to simulate a single, more realistic vertical crack.

When the secondary microcracks are not allowed to develop, the structure becomes notably stiffer (Fig. 3.15). In general, the primary microcracks form at flatter angles when secondary cracking is prohibited. Crack angles in models permitting and restricting transverse crack formation are essentially the same (within 2 degrees) until the imposed displacement reaches 90 μm. At larger imposed displacements, the crack angles vary by 10-15 degrees. The increased flatness of the primary cracks is partially responsible for the beam's stiffer response. However, more important is the fact that the model has no means for approximating a steeper crack once the transverse cracks are prohibited. The process zone extends until microcracks, oriented at an angle of 19.5 degrees, develop.

This occurs at an imposed displacement of 140 μm. The microcracked element at the process zone tip is then sufficiently stiff to retard further extension of the process zone.

These analyses clearly indicate the need to correctly estimate the angles of microcrack formation, if accurate predictions of structural response are to be made. Variations in crack angles may cause the stiffness and ductility of a concrete structure to be overestimated. The precise angles at which cracks develop in a structure are rarely known apriori. Consequently, constraining cracks to form at preselected angles is not an objective modeling procedure.

3.3.3 Fracture Energy Effects

Analyses were conducted to study the sensitivity of the beam's response to variations in the assumed fracture energy. A mesh with 40 elements through the depth and a nonlinear zone three elements wide was used in each analysis. No constraints were placed on the crack angles and the discontinuous tension softening representation was employed. As discussed in Section 3.3.1, the discontinuous model gives rapid crack localization. The fracture energy analyses provided an opportunity to examine the performance of this tension softening representation. Fracture energies of 50, 100, and 200 N/m were considered. The load-deflection responses of the three models are shown in Fig. 3.19. The process zone lengths at various imposed displacements are compared in Fig. 3.20. Crack patterns are presented in Fig. 3.8, 3.21, and 3.22.

As the fracture energy, G_f, increases, both the peak load and the displacement associated with the peak load increase. However, the rise in the peak load is not proportional to the change in the fracture energy. As the fracture energy doubles from 50 to 100 N/m, the maximum load carried by the specimen increases by 14.9%. When the fracture energy is again doubled (to 200 N/m), the predicted peak load rises by 11.4%. Instead of drastically changing the maximum load the structure can carry, increases in fracture energy broaden the peak of the load-deflection curve. At high fracture energies, the structure maintains the same load while undergoing considerable deformation, i.e., the concrete responds like a tough material. Although the load-deflection curves for the three models deviate radically on the descending branch, the ascending branches are somewhat similar. This is expected. When the microcracks begin to open, the stress transferred by the three models is almost equal. As the cracks widen, the stress transferring capability, and consequently the stiffness of the specimens deviate.

Similarly, the process zone lengths in the three models are identical for displacements of 60 μm or less. Beyond this point, the process zone grows most quickly when the fracture energy is 50 N/m, and extends most slowly when G_f is 200 N/m.

In all cases, the process zone is initially 5 mm wide. Points within the side elements nearest the center column sporadically crack as the process zone extends. Although the process zone widens to 10 mm in these regions, it relocalizes into a

single element as it continues to develop vertically. In the low energy model (G_f = 50 N/m), the process zone expands to 15 mm when the remaining ligament is reduced to 25 mm (12.5% of the beam depth). At this point, the propagation of the process zone in the center column is retarded as it reaches the compressive region directly below the applied load. The process zone then branches and continues to extend vertically (Fig. 3.21).

At process zone lengths less than 57.5 mm, the crack angles in the three models vary by no more than 3 degrees. For longer process zones, the differences in crack angle range from 5 to 10 degrees. In all cases, the crack angles alternate and become flatter in upper sections of the process zone. Transverse cracks form throughout the center column and open slightly. This response is similar to that in the unconstrained crack models previously discussed.

Two aspects of behavior are limited to the low energy model; microcracks at the base of the process zone totally lose their ability to transfer normal stress, and the process zone branches into two distinct segments as the remaining ligament becomes small. Such a response would be observed in the models with fracture energies of 100 N/m and 200 N/m if additional displacement was applied to the specimen.

What are the implications of these fracture energy findings for general structural modeling? Clearly, the computed response of the notched beam is dependent on the assumed fracture energy as well as the concrete tensile strength, descending branch

shape, and the angles of microcrack formation. Fortunately, the macroscopic response (load-deflection curve and length of process zone) of the specimen is relatively insensitive to small changes in fracture energy. This is especially true when G_f becomes moderately large. Because of this, only a reasonable estimate of the fracture energy for concrete in a structure is required for analysis.

3.3.4 Effects of Load Increment Size

The formation of microcracks is a loading dependent phenomenon. Both the orientation and the number of cracks that develop in a structure are affected by the size of the load increments used for the analysis. As demonstrated in Reference 13, when load is applied in small increments, microcracked elements may relieve stresses in adjacent elements, thereby preventing them from cracking. The current model, with its provisions for tension softening and unloading, should minimize the effects of load-step size. When the normal stress is not forced to zero after microcracks form, the consequences of prematurely microcracking elements are reduced. An element can either unload or soften slightly, but continues to transfer large stresses perpendicular to the microcracked direction.

In this section, attention is focused on two questions relating to load-step size.

1) How sensitive is the response of the notched beam to the relative size of load steps used for an analysis?

2) Can sufficiently small load steps be taken to restrict the width of the process zone to a single element?

Of the tension softening models capable of representing the behavior of plain concrete, the discontinuous and linear models represent two extremes in terms of their ability to provide stress relief immediately after microcracks form. Because of this, only these two tension softening representations were used to study the effects of load-step size. The linear and discontinuous problems originally discussed in Section 3.3.1 were reanalyzed using smaller load steps. All other modeling parameters remained unchanged. A grid with 40 elements through the depth and a nonlinear zone three elements wide was analyzed. No constraints were placed on the angles of microcrack formation. Results obtained with the discontinuous model are discussed first.

In the small step analysis of the discontinuous model, load steps were selected so that the center cracks had an opportunity to widen and the side elements to unload without cracking. At most, primary cracks formed at 2 Gauss points during iteration 1 of a load step and 4 Gauss points (1 element) cracked over the course of a step. The load-deflection responses obtained from finite element computations utilizing small and large load steps are compared in Fig. 3.23. Eighteen load steps were used in the large step analysis, 43 in the small step computations. The load-deflection responses for the two analyses are virtually identical.

The process zone lengths are equal for all but two points of comparison, where they differ by only 2.5 mm. Although smaller steps are required at large displacements, it is possible to limit the process zone to the center column of elements. Thus, the process zone has a constant width of 5 mm for the small step analysis while it expands to 10 mm over some portions of the beam when large steps are used to perform the computations.

With the exception of the cracking of side elements, the crack patterns for the small (Fig. 3.24) and large (Fig. 3.8) step analyses are almost indistinguishable. The crack angles differ by less than 1.5 degrees for process zone lengths of 57.5 mm or less. At process zone lengths greater than 52.5 mm, microcracks consistently develop in the side elements when larger load steps are used. The formation of these cracks causes the stresses in the specimen to be redistributed somewhat differently than those in a beam where cracks only develop in the center column.

In addition, even if cracks unload immediately after they develop, some energy is absorbed in their formation. The minimum amount of energy absorbed varies with the tension softening model. In the case of the linear model, almost all of the energy absorbed in initiating a crack may be recovered upon unloading, while with the discontinuous model the minimum nonrecoverable energy is indicated by the shaded area in Fig. 3.25.

The slight differences in the strain energy and stress distributions in the models with and without cracked side elements are reflected by growing differences in the crack angles of points

in the upper region of the process zone. When the length of the process zone exceeds 57.5 mm, the deviation in crack angles for the two analyses ranges from 4 to 6 degrees, and in one instance reaches 10.7 degrees. However, the average difference in crack angle for the two sets of computations is only 1.3 degrees, with the microcracks in the small step analysis forming at slightly flatter angles. Clearly, these small differences in crack behavior had no impact on the macroscopic response of the structure.

To further test the objectivity of the model with respect to load increment size, a similar analysis was performed using the linear descending branch. A model with a three element wide nonlinear zone and unconstrained cracks, originally discussed in Section 3.3.1, and a model with constrained cracks and a nonlinear zone three elements wide were analyzed. The analysis of the constrained crack model was performed to determine if the non-vertical microcrack angles affected the ability of the elements in the center column to protect the side elements from cracking. Once this question was answered, the analysis was terminated. The results of this study are not shown.

Unlike the analysis of the discontinuous model, small enough steps could not be taken to prevent elements outside the center band from cracking. This was true both when the cracks were constrained to form vertically and horizontally and when no constraints were placed on crack angle. The linear model is simply not capable of consistently relieving stresses in adjacent elements quickly enough to prevent their cracking. In both the constrained

and unconstrained models, the process zone first broadens when its length reaches 22.5 mm.

In the small step analysis of the unconstrained crack model, steps were initially sized so that the development of the process zone was limited to the center column. When this was no longer possible, the load increments were selected so that only two Gauss points in the center band cracked during the course of a step. Ninety-eight steps were used in the small step analysis, 18 steps in the large step computations. The load-deflection curves generated by the two analyses are shown in Fig. 3.26.

No differences between the load-deflection responses of the small and large step analyses are discernible at displacements less than 145 μm. At larger displacements, the small step curve is slightly stiffer. At most, the predicted loads from the two analyses differ by 4%.

The extent of the process zone is identical for the two sets of computations at all but one point of comparison. At a deflection of 130 μm, the process zone is half an element longer when large load increments are used for the analysis. Although the side elements crack, the smaller steps do reduce the width of the process zone (Fig. 3.27). When large load steps are used, the process zone is consistently 15 mm wide. With the small load increments, the process zone is initially 5 mm wide and broadens first to 10 mm, and then to 15 mm as it extends vertically. Unlike the discontinuous model, once the process zone widens, it does not relocalize.

The small step analysis permits the process zone development to be examined closely. Two consistent patterns in the cracking behavior are observed once the process zone widens to 15 mm. Fig. 3.28a indicates the order in which Gauss points in the side column of elements crack. Fig. 3.28b shows the sequence of microcrack formation along the boundary between the center and left side columns. As indicated in the figures, the lower right Gauss point is the first point within a side element to crack; this point cracks before the point located at the same depth in the center column. This vertical extension of the process zone first in the side elements, and then in the center column was also noted in the large step computations.

When large load increments are used in the analysis, several points outside the center band crack simultaneously. This rarely occurs when smaller load steps are used. As a result, the strain paths and the associated stress states at the Gauss points differ as different load increments are selected for the finite element computations. The small differences in the stress state at the process zone tip produce microcracks that form at slightly different orientations. On the average, microcracks in the small step analysis form at angles that are 3.2 degrees flatter than those in the large step analysis. The differences in crack angle increase as the process zone lengthens. At the later stages of loading, when the load-deflection curves start to deviate, crack angles computed using large and small step analyses typically differ by 4 to 12 degrees and may vary by as much as 17 degrees. These differences in

crack angle are responsible for the variations in stiffness of the load-deflection curves.

The formation and response of the transverse cracks predicted by the small and large step analyses are consistent. In both cases, transverse cracks form in the side elements at the Gauss points closest to the center column, when the process zone depth exceeds 40 mm. While the transverse cracks in the center column continue to open slightly, those in the side elements unload as the structure is subjected to additional load.

3.3.5 Effects of Grid Refinement

A valid finite element model produces convergent load-deflection curves as a mesh is refined. Bazant and Oh designed their constitutive model to be objective with respect to grid refinement. To check the sensitivity of the model employed in this study to changing element size, a mesh with four times as many elements through the depth, 160, was analyzed. All elements in the one element wide nonlinear zone were 1.25 mm square. A linear tension softening representation was used and microcracks were constrained to form vertically and horizontally.

The differences in the computed load-deflection responses of the coarse (40 elements through the depth) and fine (160 elements through the depth) grids are negligible (Fig. 3.29). The refined mesh permits the process zone length to be more accurately estimated. At any point in the analysis, the difference between the process zone lengths in the two models is less than the potential error in the estimates made with the coarse grid (Fig. 3.30).

As the element width is decreased from 5 to 1.25 mm, a sharper crack tip is introduced in the specimen. Thus, Irwin's expressions, which predict that both σ_x and σ_y approach infinity along a line directly above a sharp crack tip, should be more representative of the fine mesh response than they are of the coarse mesh behavior. This proves to be the case. Not only does the process zone start to develop at a smaller imposed displacement (10 rather than 20 μm) in the fine mesh, but the lag between the formation of the primary and secondary microcracks is reduced. At displacements greater than 100 μm, the primary and secondary cracks form simultaneously in the model with 160 elements through the depth. When the coarser mesh is used, this does not happen consistently until the displacement imposed on the beam reaches 140 μm.

One final difference between the transverse crack behavior in the two models is observed. In the coarser grid, no transverse cracks form at process zone depths less than 15 mm. When the finer mesh is analyzed, transverse cracks start to develop when the process zone length exceeds 1.25 mm (i.e. just reaches the second element).

In both models, the secondary cracks unload as the structure continues to deform. As discussed in Section 3.3.2, the behavior of the secondary cracks depends on the angles at which the primary microcracks form. If the primary cracks are exactly vertical, the secondary cracks unload. Otherwise, the transverse cracks open as the structure undergoes additional deformation.

The differences in the behavior of the transverse cracks in the coarse and fine meshes are consistent with the fact that a sharper crack is effectively introduced in the fine mesh. Although they must be permitted to form, the transverse cracks have little impact on the overall behavior of the beam. As a result, the load-deflection responses of the two grids are similar and the constitutive model may be considered objective with respect to grid refinement.

3.4 Concluding Remarks

This chapter presented the results of a number of finite element studies designed to investigate the effects of modeling the tension softening behavior of concrete. Rather than attempting to match a wide range of experimental data, this study examined the effects of various modeling parameters on the computed macroscopic response of a plain concrete fracture specimen. The sensitivity of the specimen's response to changes in fracture energy, load-increment size, and mesh refinement were examined. In addition, the effects of four descending branch shapes, the width of the nonlinear zone, and the angles at which microcracks developed were studied.

Load-deflection curves and general cracking patterns provided the primary means for evaluating the beam's response. Comparisons were also made on the basis of the horizontal and vertical extent of the process zone.

The results of the study indicate that the assumed concrete fracture energy, tensile strength, and post-peak tensile response all interact to influence the general behavior of a concrete structure. While the optimum combination of these three parameters is not currently known, several general trends were noted.

As the slope of the descending branch of the tensile stress-strain curve became less severe, the maximum load supported by the notched beam increased. Associated with this larger peak load, was a more brittle post-peak response. Once the maximum load was attained, the beam lost stiffness more rapidly.

Increases in the concrete fracture energy acted primarily to toughen rather than strengthen the specimen. Doubling the fracture energy increased the load capacity of the beam by roughly 10 to 15%. Also, the peak of the load-deflection curve broadened. While the peak load did not change substantially, the ability of the specimen to sustain this load while undergoing additional deformation did increase noticeably.

Variations in the width of the nonlinear zone had no significant impact on the behavior of the beam. Provided the constitutive model permits unloading, and the tension softening model is able to relieve stresses in elements adjacent to an opening crack, cracks quickly localize into a region one element wide. Only minimal energy is absorbed in generating the microcracks that subsequently unload.

Similarly, the model was found to be objective with respect to both load-step size and grid refinement. The mesh refinement results are consistent with those of Bazant and Oh and follow logically from the scaling of ε_0 based on fracture energy.

Finally, the microcrack angles in a structure must be correctly estimated if accurate predictions of structural response are to be made. Variations in crack angles within individual elements due to variations in strain between Gauss points may cause the stiffness and ductility of a structure to be overestimated, if they do not correctly represent local response. In turn, predictions of the load carrying capacity and failure mode of a structure containing misoriented cracks may be incorrect. Two possible solutions can be offered to this problem. One alternative is to regulate the behavior at all Gauss points within an element based on the average behavior of the points. Another possibility is to use center-point rather than 2x2 integrated 4-node elements. Both of these alternatives require additional study.

Chapter 4

SUMMARY AND CONCLUSIONS

4.1 Summary

The effects of the descending branch of the tensile stress-strain curve, fracture energy, grid refinement, and load-step size on the response of finite element models of notched concrete beams are studied. The width of the process zone and constraint of crack angles are also investigated.

The constitutive model used in the study extends Bazant and Oh's (6) strain softening, smeared crack compliance formulation to include unloading. Cracking of the concrete in tension is the only nonlinear behavior modeled. Load-deflection curves and general cracking patterns provide the primary means for evaluating the specimen's response. Variations in process zone size are noted. Also, comparisons with discrete crack models employing identical stress-strain relationships are made.

Cracks are modeled with a smeared representation. A limiting tensile stress criterion governs crack initiation. The tensile response is linear elastic prior to cracking. The post-cracking behavior is regulated by a descending branch of user-specified shape using one of four representations: linear, bilinear, discontinuous, or a Dugdale model. The terminal point of the descending branch is a function of the fracture energy, crack angle, element size, and descending branch shape. Unloading occurs at a slope equal to the initial modulus of the material. The concrete is treated as linear elastic in compression.

All analyses are performed on a 200 x 200 x 800 mm notched concrete beam, with an initial notch length of 80 mm, originally analyzed by Petersson (36). Four-node linear isoparametric elements are used. Two levels of grid refinement are considered. The notch consists of "precracked" elements, with both the tangent and secant moduli of elasticity normal to the crack reduced to zero before displacement is imposed on the beam.

4.2 Conclusions

The results of the finite element studies discussed in this report support the following conclusions.

1. The post-peak concrete tensile behavior controls the load-deflection response of the structure. As the slope of the descending branch of the tensile stress-strain curve becomes less severe, the process zone extends more slowly, and the load capacity of the specimen increases. The slope of the stress-strain curve immediately following the peak is most critical in determining the stiffness of the beam.
2. Increasing the fracture energy primarily toughens, not strengthens, the specimen. Doubling the fracture energy increases the load capacity of the beam by 10-15%. The range of deformation over which the specimen sustains loads near the peak load is increased significantly.
3. The macroscopic response of the beam is insensitive to small changes in fracture energy. For a fixed tensile strength, the sensitivity continues to drop with increases in fracture energy.

4. The width of the nonlinear zone has a negligible effect on the behavior of the beam. If the constitutive model permits unloading, and the tension softening model is capable of relieving stresses in elements adjacent to an opening crack, the crack quickly localizes into a region one element wide. Minimal energy is absorbed in forming the microcracks that subsequently unload.
5. The process zone width is a function of both the descending branch shape and the size of the load increments used in the analysis. Tension softening representations that quickly reduce the stress transferred across newly formed cracks produce narrower process zones. Decreasing the load-step size also reduces the process zone width. Cracks in the center column relieve stresses in adjacent elements and protect them from cracking. If the tension softening model does not reduce the stress transferred normal to the microcracks quickly enough, load cannot be applied in small enough increments to limit the process zone to a one element wide band.
6. Cracks throughout the process zone form at non-vertical angles. The sampling points in the 2x2 integrated four-node elements are located off-center. Small shear stresses exist at the Gauss points, producing principal tensile stresses that are oriented at oblique angles. The deviation of the cracks from the vertical increases as the process zone lengthens.

7. Since the 2x2 integrated linear isoparametric element poorly represents the shear stress distribution in the beam, cracks within an element develop at alternating angles.
8. Transverse (secondary) cracks form throughout the center column of elements. There is a gap between the process zone tip and the region where transverse cracks develop. This gap shortens as the process zone lengthens. The stress transferred across the secondary cracks remains high, and the crack widths small, even at large beam displacements. When the primary cracks are constrained to form vertically, the horizontal secondary cracks unload. Otherwise, the transverse cracks throughout the center column open. Both the primary and secondary cracks may open in an attempt to simulate a single, more nearly vertical crack.
9. The crack angles in a structure must be properly represented if reliable predictions of structural response are to be made. Misoriented cracks may cause the stiffness and ductility of a structure to be overestimated. In turn, predictions of the load capacity and failure mode may be in error.
10. The Bazant-Oh (6) formulation with provisions for unloading is objective with respect to grid refinement and load-step size.

4.3 Recommendations for Further Study

A number of areas remain to be examined. These are briefly outlined below.

1. The current model represents unloading as an elastic rebound of the material "between" the microcracks. Modifying the unloading curve to include crack closure would produce a more realistic constitutive model. How sensitive structural response is to the unloading representation should be examined.
2. Schemes to improve the model's ability to properly represent the angles at which microcracks form should be investigated. Two possibilities were suggested by this study; using center-point rather than 2x2 integrated 4-node elements, or using average strain values to control the behavior of an element.
3. No provisions were made for modeling aggregate interlock in this study. The inclusion of a non-zero shear retention factor introduces another energy component to be considered. The interaction between tension-softening and aggregate interlock should be examined. A study of a mixed-mode fracture specimen, paralleling the one described in this report, is recommended.
4. The optimum combination of fracture energy and descending branch shape to be used in modeling concretes of normal quality is still not known. Comparisons with experimental data are required.

5. A structure where multiple cracks form and propagate should be thoroughly studied. A shear beam would be one such structure.
6. Analyses should be performed to determine if the model is objective with respect to process zone size. The process zone width was limited to a maximum of three elements in the models used for this study. Additional analyses should be performed on specimens modeled with differing degrees of grid refinement and nonlinear zones sufficiently wide to allow the process zone to find its own width.

REFERENCES

1. Bashur, Fuad K. and Darwin, David, "Nonlinear Model for Reinforced Concrete Slabs," Journal of the Structural Division, ASCE, Vol. 104, No. ST1, Jan. 1978, pp. 157-170.

2. Bazant, Zdenek P., "Fracture in Concrete and Reinforced Concrete," Preprints of William Prager Symposium on Mechanics of Geomaterials: Rocks, Concretes, Soils, 1983, pp. 281-316.

3. Bazant, Zdenek P., "Instability, Ductility, and Size Effect in Strain-Softening Concrete," Journal of the Engineering Mechanics Division, ASCE, Vol. 102, No. EM2, Apr. 1976, pp. 331-344.

4. Bazant, Zdenek P. and Cedolin, Luigi, "Fracture Mechanics of Reinforced Concrete," Journal of the Engineering Mechanics Division, ASCE, Vol. 106, No. EM6, Dec. 1980, pp. 1287-1306.

5. Bazant, Zdenek P. and Cedolin, Luigi, "Blunt Crack Band Propagation in Finite Element Analysis," Journal of the Engineering Mechanics Division, ASCE, Vol. 105, No. EM2, Apr. 1979, pp. 297-315.

6. Bazant, Zdenek P. and Oh, Byung H., "Crack Band Theory for Fracture of Concrete," Materiaux et Constructions, Vol. 16, No. 93, May-June 1983, pp. 155-177.

7. Catalano, David and Ingraffea, Anthony R., "Concrete Fracture: A Linear Elastic Fracture Mechanics Approach," Department of Structural Engineering Report 82-1, Cornell University, Ithaca, N.Y., 1982.

8. Cedolin, Luigi and Dei Poli, Sandro, "Finite Element Studies of Shear-Critical R/C Beams," Journal of the Engineering Mechanics Division, ASCE, Vol. 103, No. EM3, June 1977, pp. 395-410.

9. Cedolin, Luigi, Dei Poli, Sandro and Iori, Ivo, "Experimental Determination of the Fracture Process Zone in Concrete," Cement and Concrete Research, Vol. 13, No. 4, July 1983, pp. 557-567.

10. Darwin, David and Attiogbe, Emmanuel K., "Load Induced Cracks in Cement Paste," Proceedings of the Fourth Engineering Mechanics Division Specialty Conference, Recent Advances in Engineering Mechanics and their Impact on Civil Engineering Practice Vol. II, American Society of Civil Engineers, New York, N.Y., 1983, pp. 1051-1054.

11. Darwin, David and Pecknold, David A., "Nonlinear Biaxial Stress-Strain Law for Concrete," Journal of the Engineering Mechanics Division, ASCE, Vol. 103, No. EM2, Apr. 1977, pp. 229-241.

12. Darwin, David and Pecknold, David A., "Inelastic Model for Cyclic Biaxial Loading of Reinforced Concrete," Civil Engineering Studies Structural Research Series No. 409, University of Illinois at Urbana-Champaign, Urbana, Ill., July 1974, 169 pp.

13. Dodds, Robert H., Darwin, David, Smith, Jerry L. and Leibengood, Linda D., "Grid Size Effects with Smeared Cracking in Finite Element Analysis of Reinforced Concrete," Structural Engineering and Engineering Materials SM Report No. 6, University of Kansas Center for Research, Inc., Lawrence, Ks., Aug. 1982, 118 pp.

14. Dodds, Robert H. and Lopez, Leonard A., "Generalized Software System for Non-Linear Analysis," Advances in Engineering Software, Vol. 2, No. 4, Oct. 1980, pp. 161-168.

15. Dodds, Robert H., Lopez, Leonard A. and Pecknold, David A., "Numerical and Software Requirements for General Nonlinear Finite Element Analysis," Civil Engineering Studies Structural Research Series No. 454, University of Illinois at Urbana-Champaign, Urbana, Ill., Sept. 1978, 195 pp.

16. Evans, R.H. and Marathe, M.S., "Microcracking and Stress-Strain Curves for Concrete in Tension," Materiaux et Constructions, Vol. 1, No. 1, Jan.-Feb. 1968, pp. 61-64.

17. Gerstle, Walter H., Ingraffea, Anthony, R. and Gergely, Peter, "The Fracture Mechanics of Bond in Reinforced Concrete," Department of Structural Engineering Report 82-7, Cornell University, Ithaca, N.Y., June 1982, 144 pp.

18. Gilbert, R. Ian and Warner, Robert F., "Tension Stiffening in Reinforced Concrete Slabs," Journal of the Structural Division, ASCE, Vol. 104, No. ST12, Dec. 1978, pp. 1885-1900.

19. Hand, Frank R., Pecknold, David A. and Schnobrich, William C., "Nonlinear Layered Analysis of RC Plates and Shells," Journal of the Structural Division, ASCE, Vol. 99, No. ST7, July 1973, pp. 1491-1505.

20. Hillerborg, Arne, "A Model for Fracture Analysis," Report TVBM-3005, Division of Building Materials, University of Lund, Sweden, 1978, 13 pp.

21. Hillerborg, Arne, Modeer, Matz and Petersson, Per-Erik, "Analysis of Crack Formation and Crack Growth in Concrete by Means of Fracture Mechanics and Finite Elements," Cement and Concrete Research, Vol. 6, No. 6, Nov. 1976, pp. 773-782.

22. Irwin, G.R., "Analysis of Stresses and Strains Near End of Crack Traversing Plate," Journal of Applied Mechanics, ASME, Vol. 24, No. 3, Sept. 1957, pp. 361-364.

23. Jofriet, Jan C. and McNeice, Gregory M., "Finite Element Analysis of Reinforced Concrete Slabs," Journal of the Structural Division, ASCE, Vol. 97, No. ST3, Mar. 1971, pp. 785-806.

24. Kabir, A.F., "Nonlinear Analysis of Reinforced Concrete Panels, Slabs and Shells for Time Dependent Effects," Report No. UC SESM 76-6, University of California, Berkeley, Cal., Dec. 1976, 219 pp.

25. Kaplan, M.F., "Crack Propagation and the Fracture of Concrete," Journal of the American Concrete Institute, Vol. 58, No. 5, Nov. 1961, pp. 591-609.

26. Lin, Cheng-Shung and Scordelis, Alexander C., "Nonlinear Analysis of RC Shells of General Form," Journal of the Structural Division, ASCE, Vol. 101, No. ST3, Mar. 1975, pp. 523-538.

27. Lopez, Leonard A., Dodds, Robert H., Rehak, Daniel R. and Urzua, Jorge, "POLO-FINITE: A Structural Mechanics System for Linear and Nonlinear Analysis," Issued as a technical report by: Civil Engineering Systems Laboratory, University of Illinois at Urbana-Champaign, and Department of Civil Engineering, University of Kansas, Lawrence, Ks., 1980, 600 pp.

28. Mindess, Sidney and Diamond, Sidney, "A Preliminary SEM Study of Crack Propagation in Mortar," Cement and Concrete Research, Vol. 10, No. 4, July 1980, pp. 509-519.

29. Modeer, Matz, "A Fracture Mechanics Approach to Failure Analyses of Concrete Materials," Report TVBM-1001, Division of Building Materials, University of Lund, Sweden, 1979, 102 pp.

30. Mufti, A.A., Mirza, M.S., McCutcheon, J.O. and Houde, J., "A Study of the Behavior of Reinforced Concrete Elements," Structural Concrete Series No. 70-5, McGill University, 1970.

31. Mufti, A.A., Mirza, M.S., McCutcheon, J.O. and Houde, J., "A Study of the Nonlinear Behavior of Structural Concrete Elements," Proceedings, The Speciality Conference on Finite Element Methods in Civil Engineering, Montreal, Canada, June, 1972.

32. Nayak, G.C., "Plasticity and Large Deformation Problems by the Finite Element Method," Ph.D. Thesis, University of Wales, Swansea, 1971.

33. Ngo, D., "A Network-Topological Approach to the Finite Element Analysis of Progressive Crack Growth in Concrete Members," Ph.D. Thesis, University of California, Berkeley, Cal., 1975.

34. Ngo, D. and Scordelis, Alexander C., "Finite Element Analysis of Reinforced Concrete Beams," Journal of the American Concrete Institute, Vol. 64, No. 3, Mar. 1967, pp. 152-163.

35. Nilson, Arthur H., "Nonlinear Analysis of Reinforced Concrete by the Finite Element Method," Journal of the American Concrete Institute, Vol. 65, No. 9, Sept. 1968, pp. 757-766.

36. Petersson, Per-Erik, "Crack Growth and Development of Fracture Zones in Plain Concrete and Similar Materials," Report TVBM-1006, Division of Building Materials, University of Lund, Sweden, 1981, 174 pp.

37. Petersson, Per-Erik, "Fracture Energy of Concrete: Method of Determination," Cement and Concrete Research, Vol. 10, No. 1, Jan. 1980, pp. 79-89.

38. Petersson, Per-Erik, "Fracture Energy of Concrete: Practical Performance and Experimental Results," Cement and Concrete Research, Vol. 10, No. 1, Jan. 1980, pp. 91-101.

39. Rashid, Y.R., "Ultimate Strength Analysis of Prestressed Concrete Pressure Vessels," Nuclear Engineering and Design, Vol. 7, No. 4, Apr. 1968, pp. 334-344.

40. Rostam, S. and Bysckov, E., "Cracks in Concrete Structures," Report No. I15, Structural Research Laboratory, Technical University of Denmark, 1971.

41. Salah El-Din, A.S. and El-Adawy Nassef, M.M., "A Modified Approach for Estimating the Cracking Moment of Reinforced Concrete Beams," Journal of the American Concrete Institute, Vol. 72, No. 7, July 1975, pp. 356-360.

42. Saouma, Victor, "Automated Nonlinear Finite Element Analysis of Reinforced Concrete: A Fracture Mechanics Approach," Ph.D. Thesis, Cornell University, Ithaca, N.Y., 1980.

43. Saouma, Victor E., Ingraffea, Anthony R. and Catalano, David M., "Fracture Toughness of Concrete: K_{Ic} Revisited," Journal of the Engineering Mechanics Division, ASCE, Vol. 108, No. EM6, Dec. 1982, pp. 1152-1166.

44. Scanlon, Andrew, "Time Dependent Deflections of Reinforced Concrete Slabs," Ph.D. Thesis, University of Alberta, Edmonton, Canada, Dec. 1971.

45. Scanlon, Andrew and Murray, David W., "Time-Dependent Reinforced Concrete Slab Deflections," Journal of the Structural Division, ASCE, Vol. 100, No. ST9, Sept. 1974, pp. 1911-1924.

46. Task Committee on Finite Element Analysis of Reinforced Concrete Structures, State-of-the-Art Report on Finite Element Analysis of Reinforced Concrete, American Society of Civil Engineers, New York, N.Y., 1982, 545 pp.

47. Van Greunen, Johannes, "Nonlinear Geometric, Material and Time Dependent Analysis of Reinforced and Prestressed Concrete Slabs and Panels," Report No. UC SESM 79-3, University of California, Berkeley, Cal., Oct. 1979, 275 pp.

48. Van Greunen, Johannes and Scordelis, Alexander C., "Nonlinear Analysis of Prestressed Concrete Slabs," Journal of the Structural Division, ASCE, Vol. 109, No. 7, July 1983, pp. 1742-1760.

49. Walsh, P.F., "Fracture of Plain Concrete," Indian Concrete Journal, Vol. 46, No. 11, Nov. 1972, pp. 469-470, and 476.

50. Westergaard, H.M., "Bearing Pressures and Cracks," Journal of Applied Mechanics, ASME, Vol. 6, No. 2, June 1939, pp. A49-A53.

51. Zienkiewicz, O.C., The Finite Element Method, McGraw-Hill, London, 1977, 787 pp.

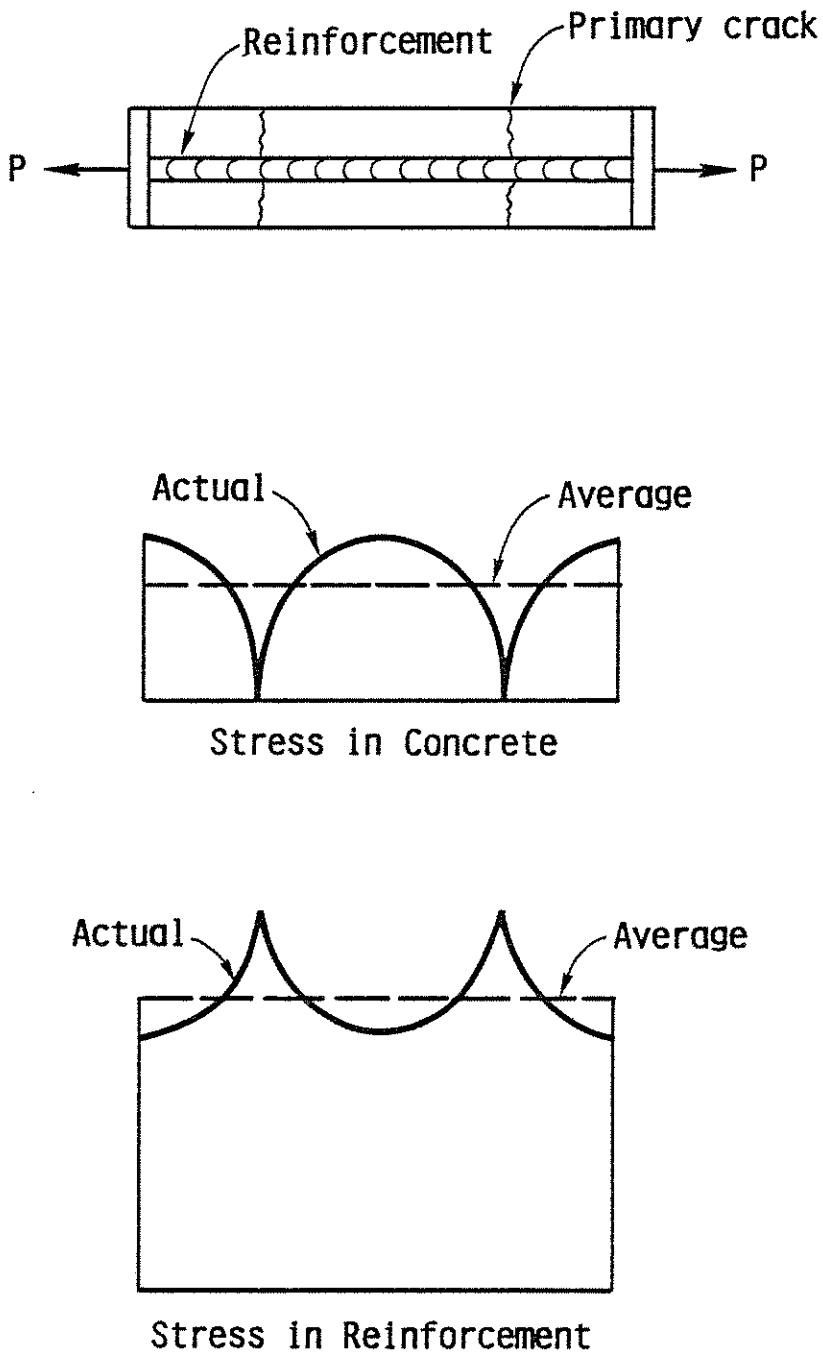

Figure 1.1. Stress Distribution in a Cracked Reinforced Concrete Element (26).

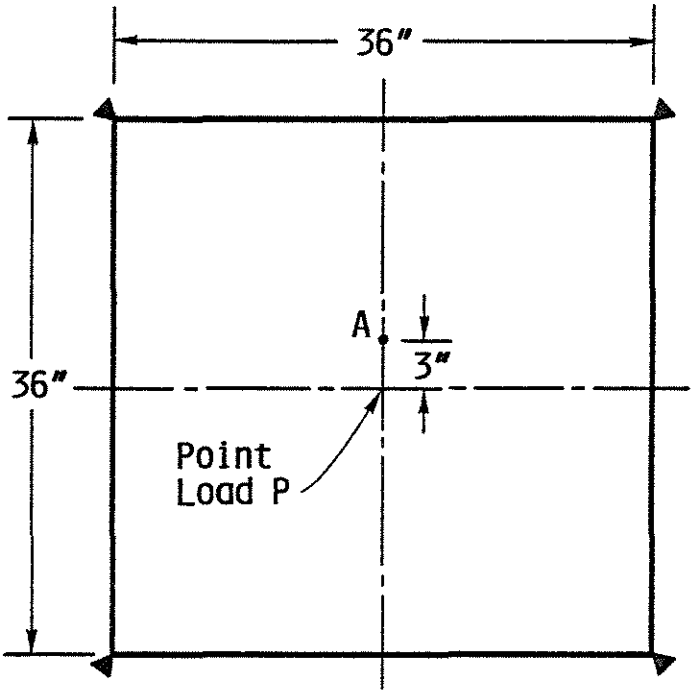

$f'_c = 5500$ psi

$E_c = 4.15 \times 10^6$ psi

$\nu = 0.15$

$\rho_x = \rho_y = 0.0085$

$E_s = 29 \times 10^6$ psi

$H = 1.75"$

$d = 1.31"$

Figure 1.2. Corner Supported, Center-Point Loaded Two-Way Slab, McNeice (23).

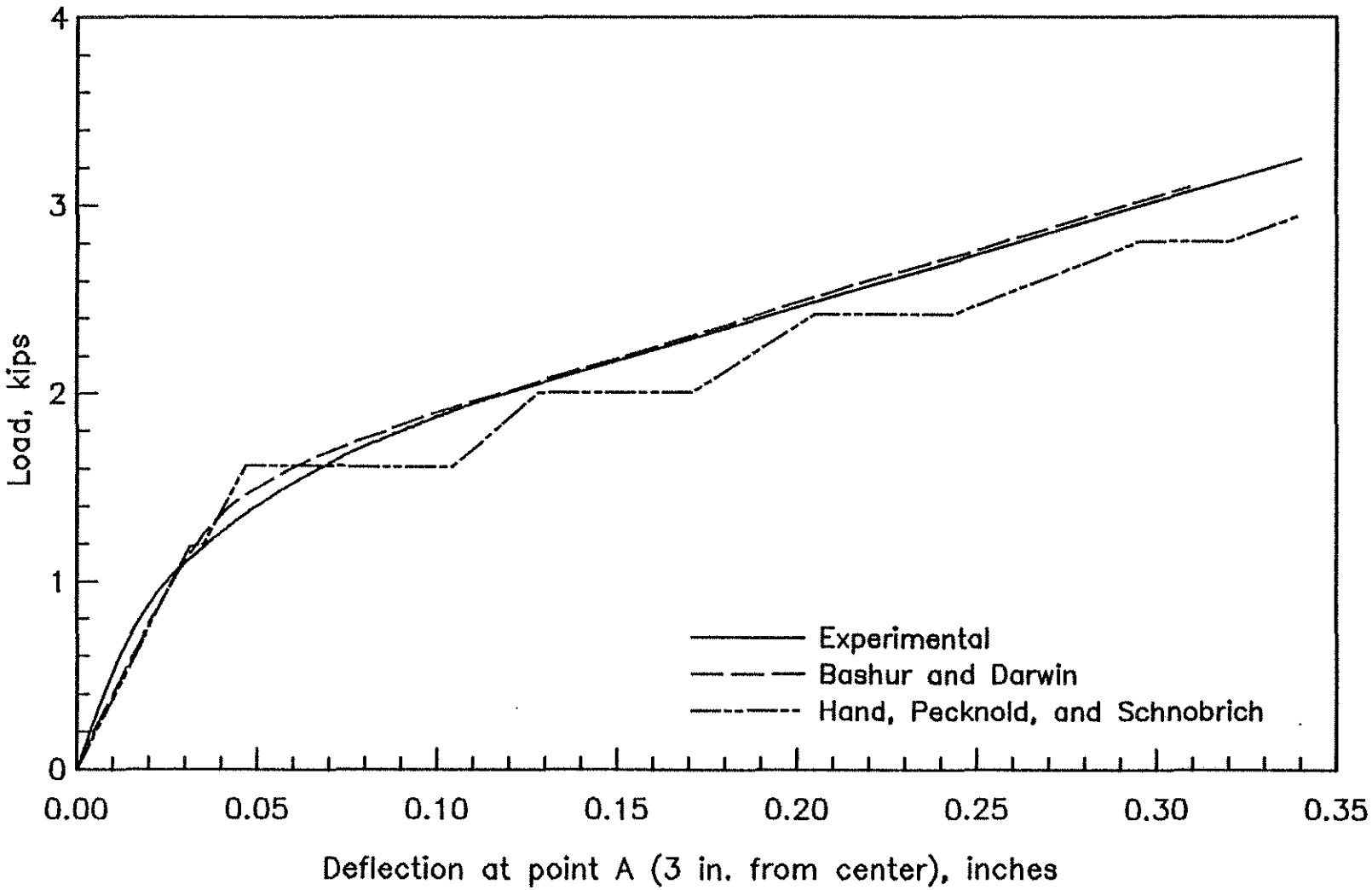

Figure 1.3. Load-Deflection Curves for Two-Way Slab Supported at Corners, Hand, Pecknold, and Schnobrich (19), and Bashur and Darwin (1,23).

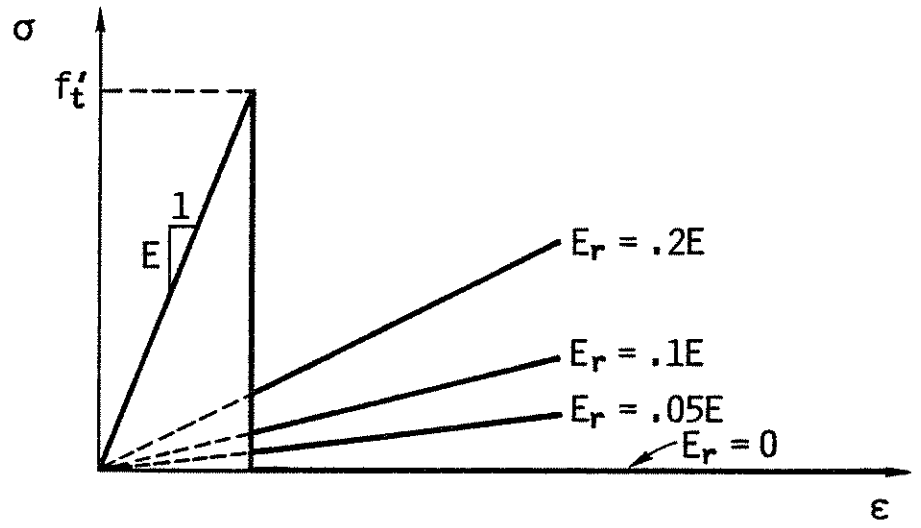

(a)

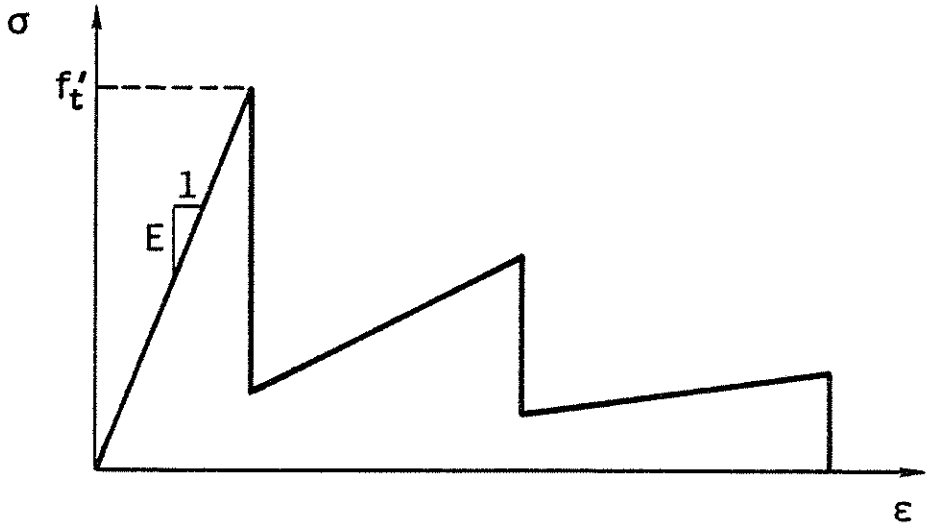

(b)

Figure 1.4. Assumed Concrete Tensile Response, Scanlon (44): (a) Post-cracking Modulus Reduced to 20, 10, 5, or 0% of Initial Value: (b) Stepped Representation.

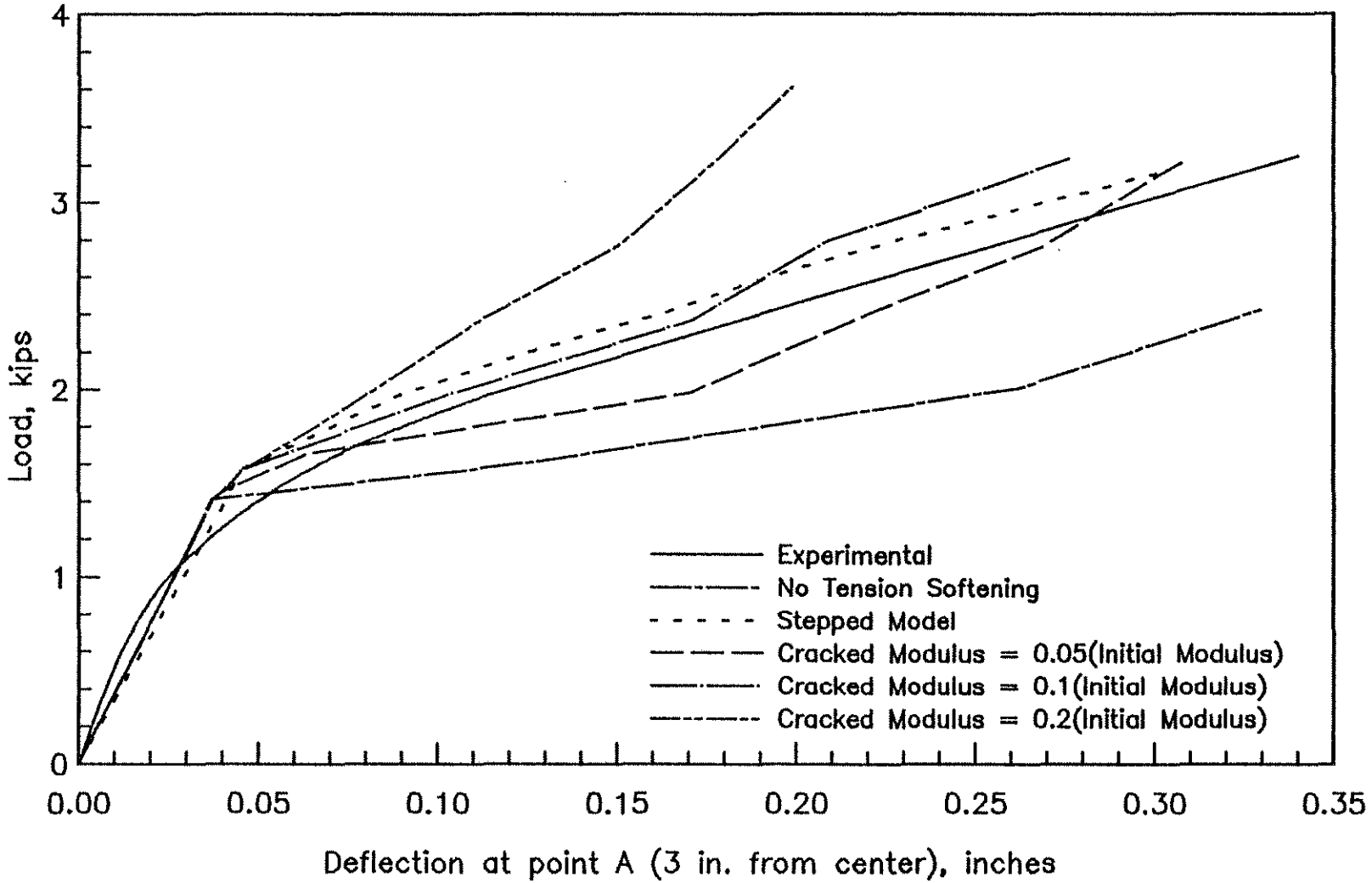

Figure 1.5. Load-Deflection Curves for Two-Way Slab Supported at Corners, Scanlon (23,44).

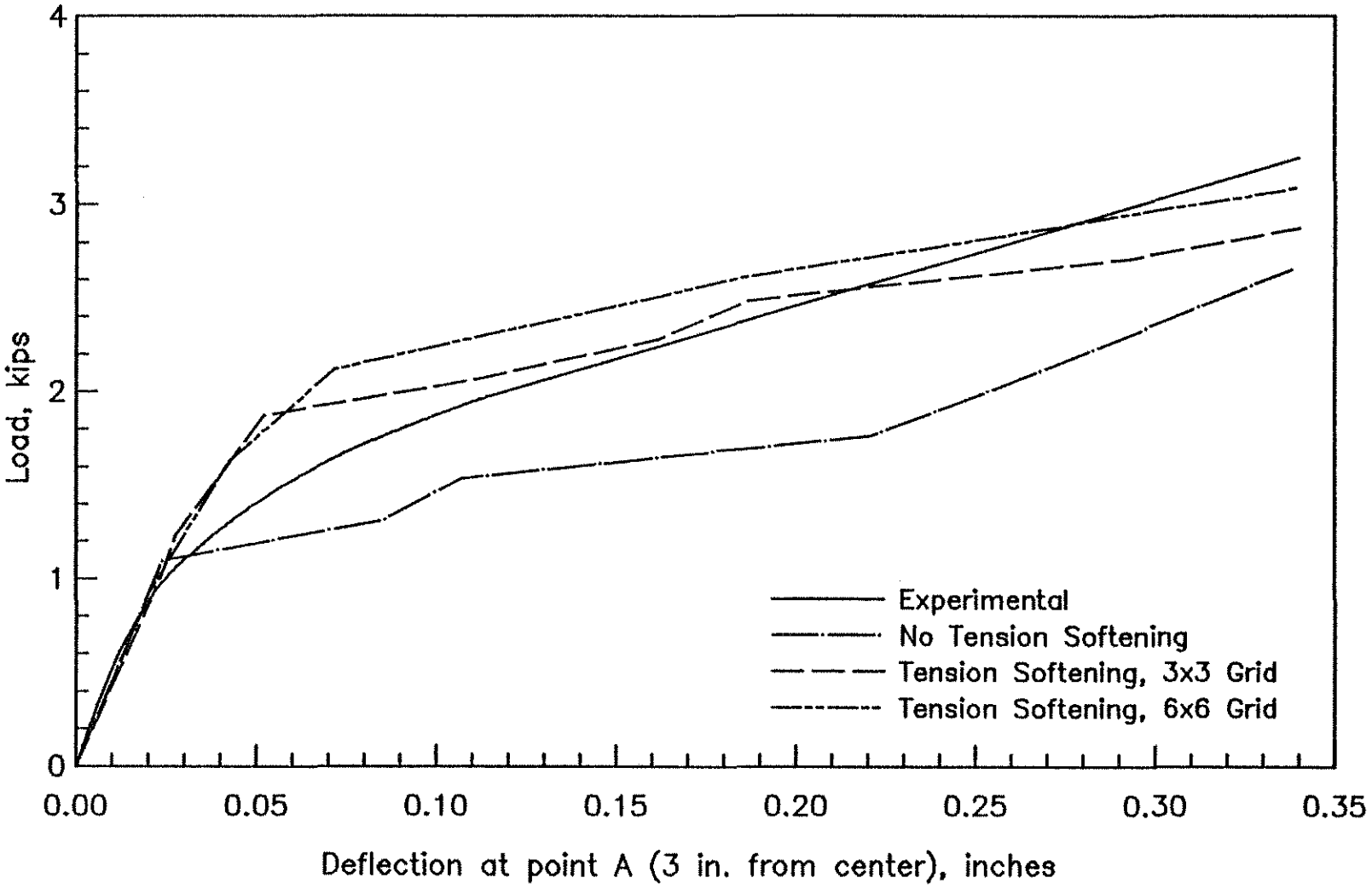

Figure 1.6. Load-Deflection Curves for Two-Way Slab Supported at Corners, Lin and Scordelis (23,26).

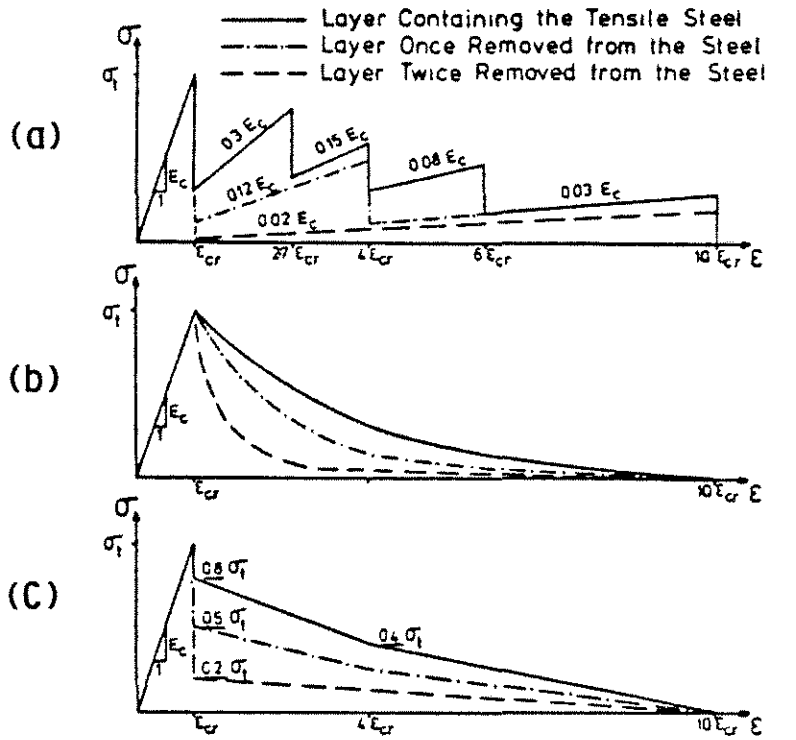

Material Modelling Law :

ε_1	ε_2	ε_3	ε_4	ε_5	ε_6	ε_7
ε_{cr}	$15\,\varepsilon_{cr}$	$3\,\varepsilon_{cr}$	$5\,\varepsilon_{cr}$	$8\,\varepsilon_{cr}$	$11\,\varepsilon_{cr}$	$14\,\varepsilon_{cr}$

E_1	E_2	E_3	E_4	E_5	E_6
$40\,E_s$	$27\,E_s$	$20\,E_s$	$16\,E_s$	$13.5\,E_s$	$10.5\,E_s$

Figure 1.7. Models Used by Gilbert and Warner (18) to Account for Tension Softening in Concrete After Cracking: (a) Scanlon's Stepped Model: (b) Lin's Gradually Unloading Model: (c) Discontinuous Model: (d) Modified Stress-Strain Diagram for Reinforcing Steel.

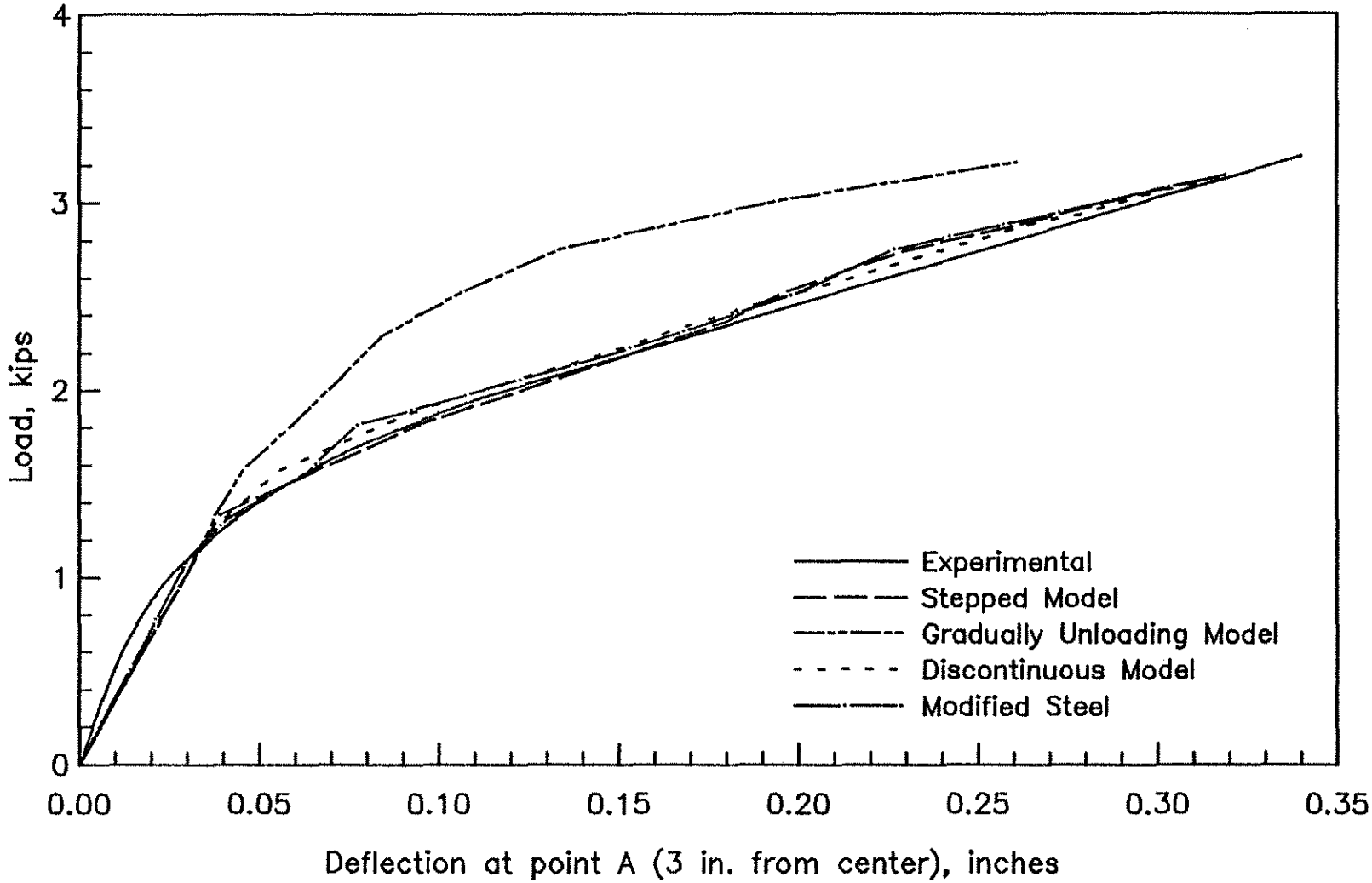

Figure 1.8. Load-Deflection Curves for Two-Way Slab Supported at Corners, Gilbert and Warner (18,23).

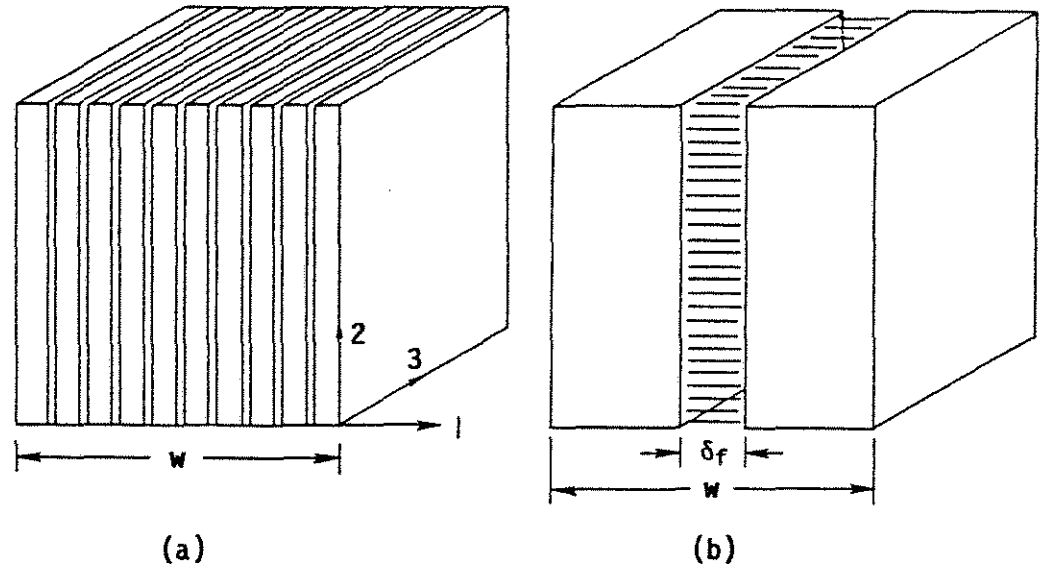

Figure 2.1. Interpretation of Smeared Crack Model: (a) Smeared Representation of Microcracked Element: (b) Lumped Approximation of Microcracked Element.

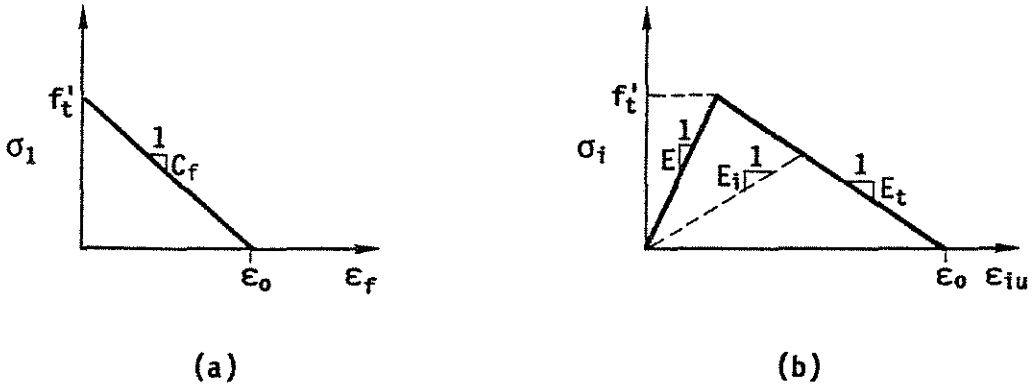

Figure 2.2. Stress-Strain Relationships for Fracture Process Zone: (a) Stress-Strain Relationship for Microcracked Material: (b) Equivalent Uniaxial Stress-Strain Curve for Tension Softening Material.

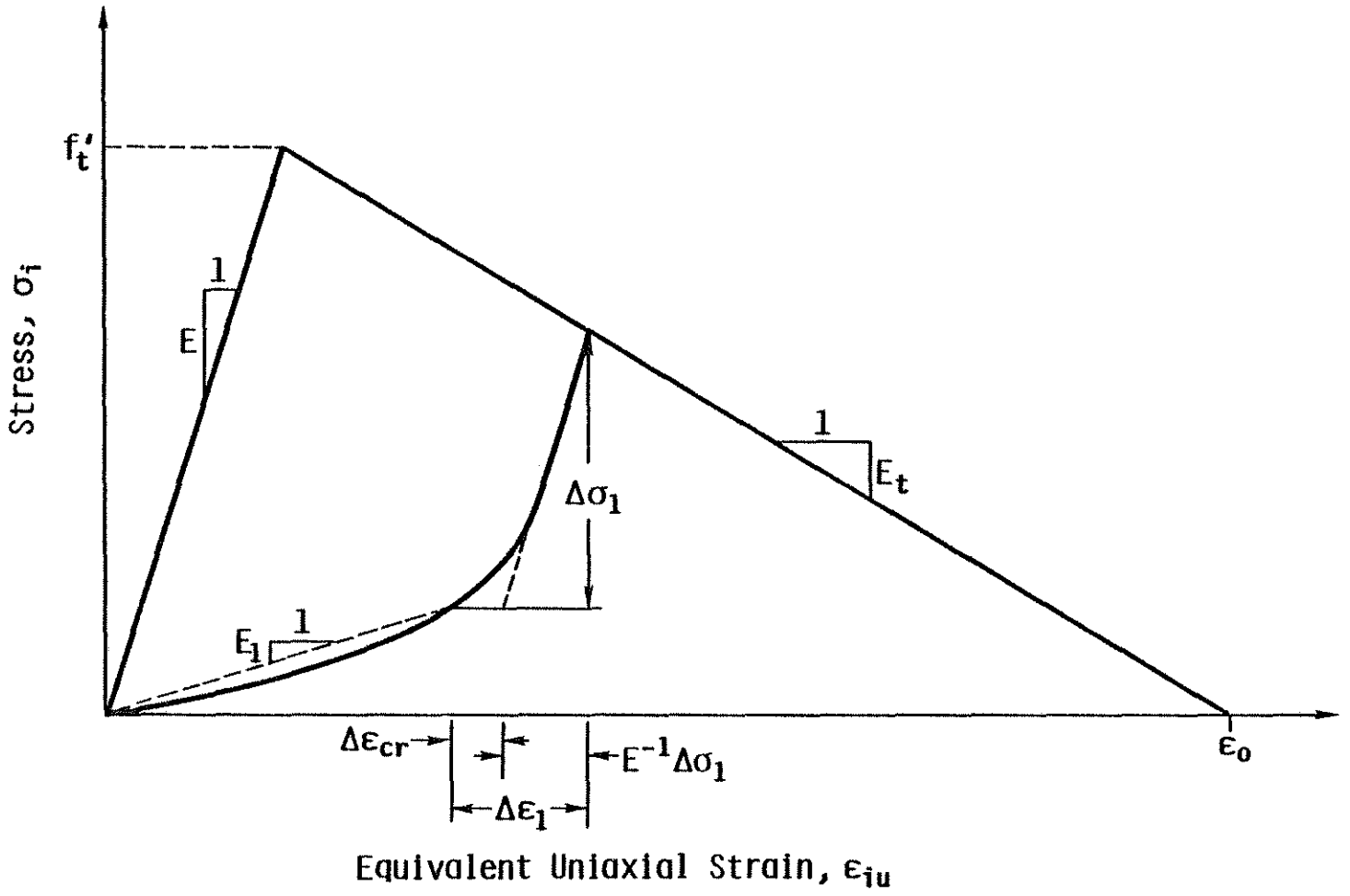

Figure 2.3. Equivalent Uniaxial Stress-Strain Curve for Tension Softening Material with Unloading.

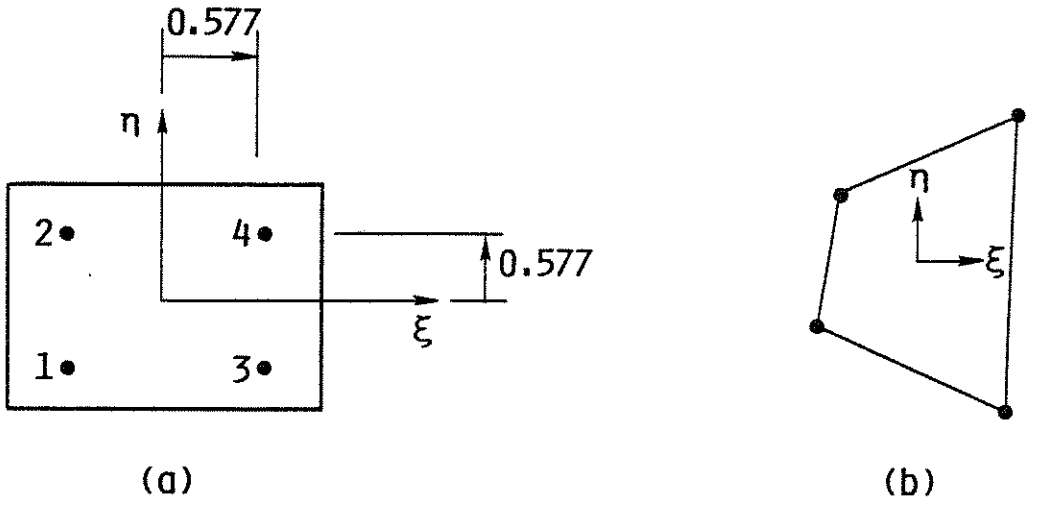

Figure 2.4. Linear, Four Node, Isoparametric Element: (a) Parent Element: (b) Element in Structure.

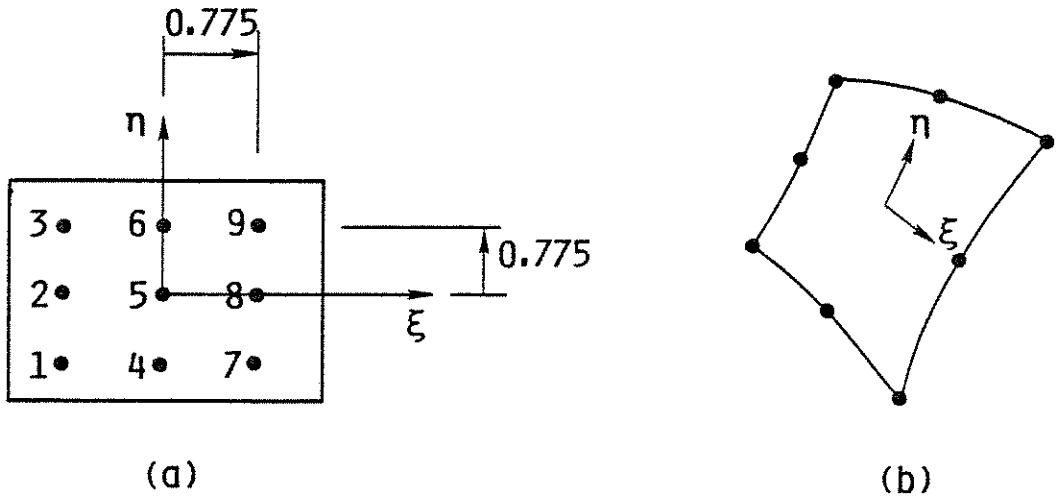

Figure 2.5. Quadratic, Eight Node, Isoparametric Element: (a) Parent Element: (b) Element in Structure.

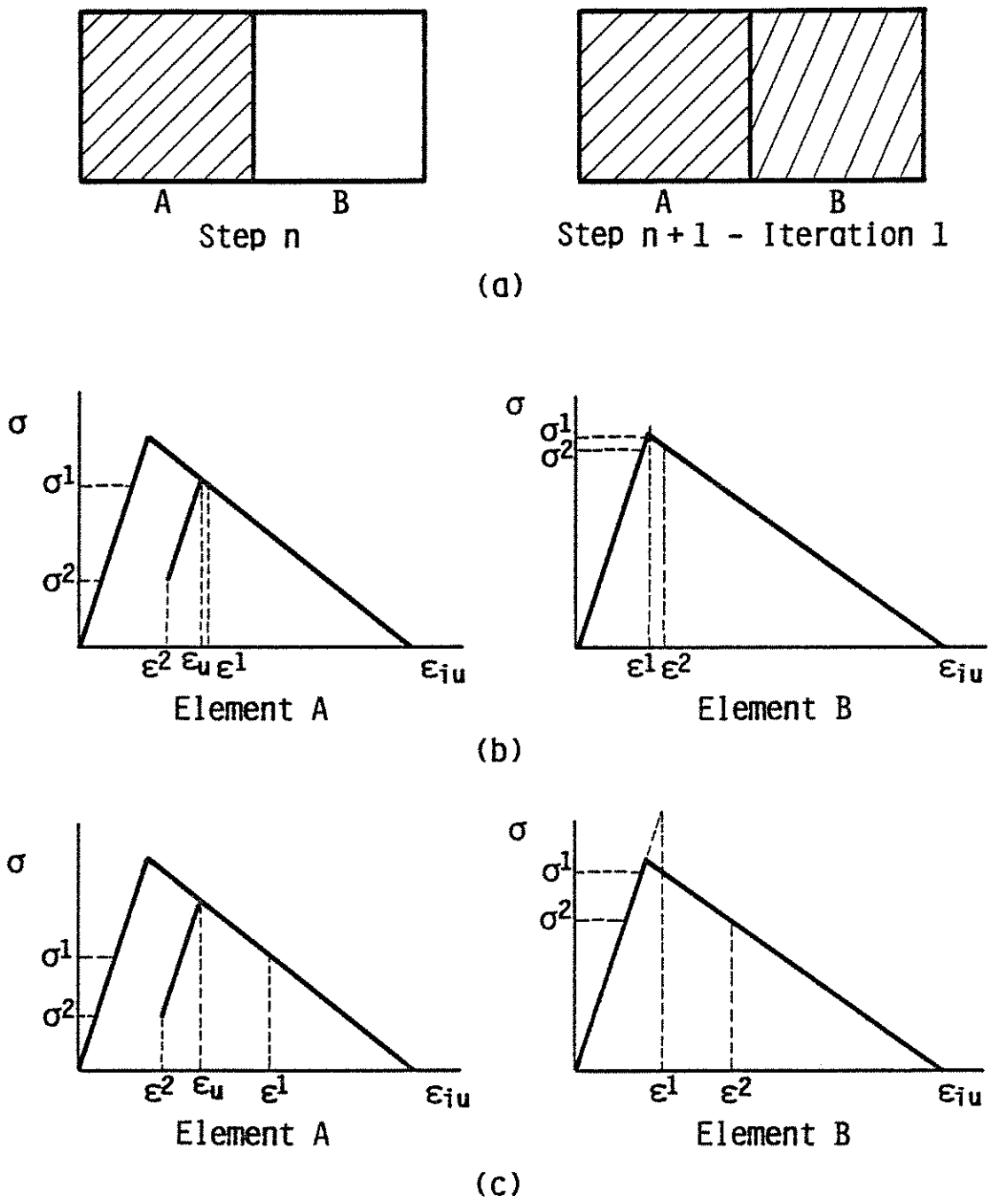

Figure 2.6. Determination of Envelope Strain from which Unloading Occurs.

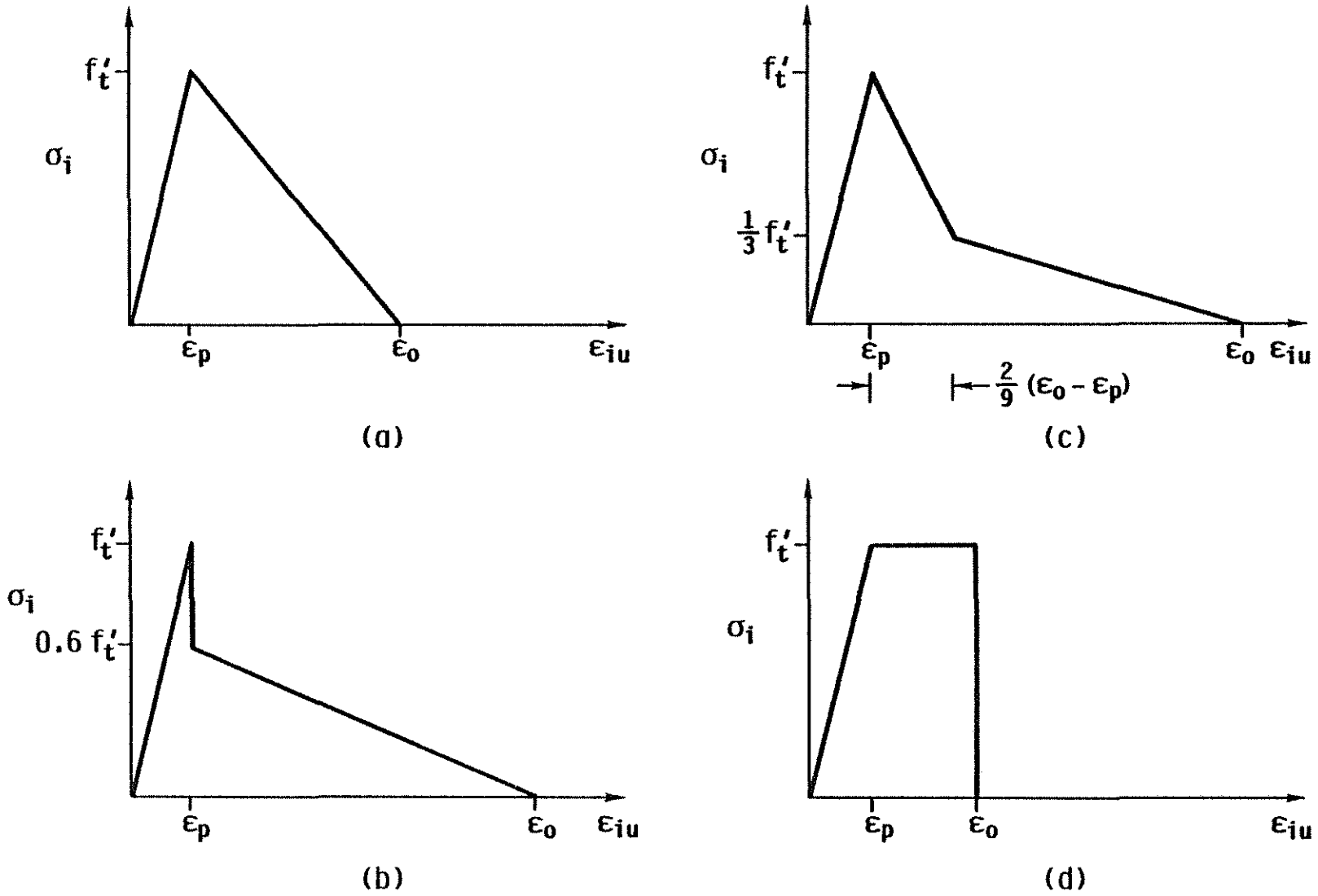

Figure 3.1. Assumed Concrete Tensile Responses: (a) Linear Softening: (b) Discontinuous Softening: (c) Bilinear Softening: (d) Dugdale Softening.

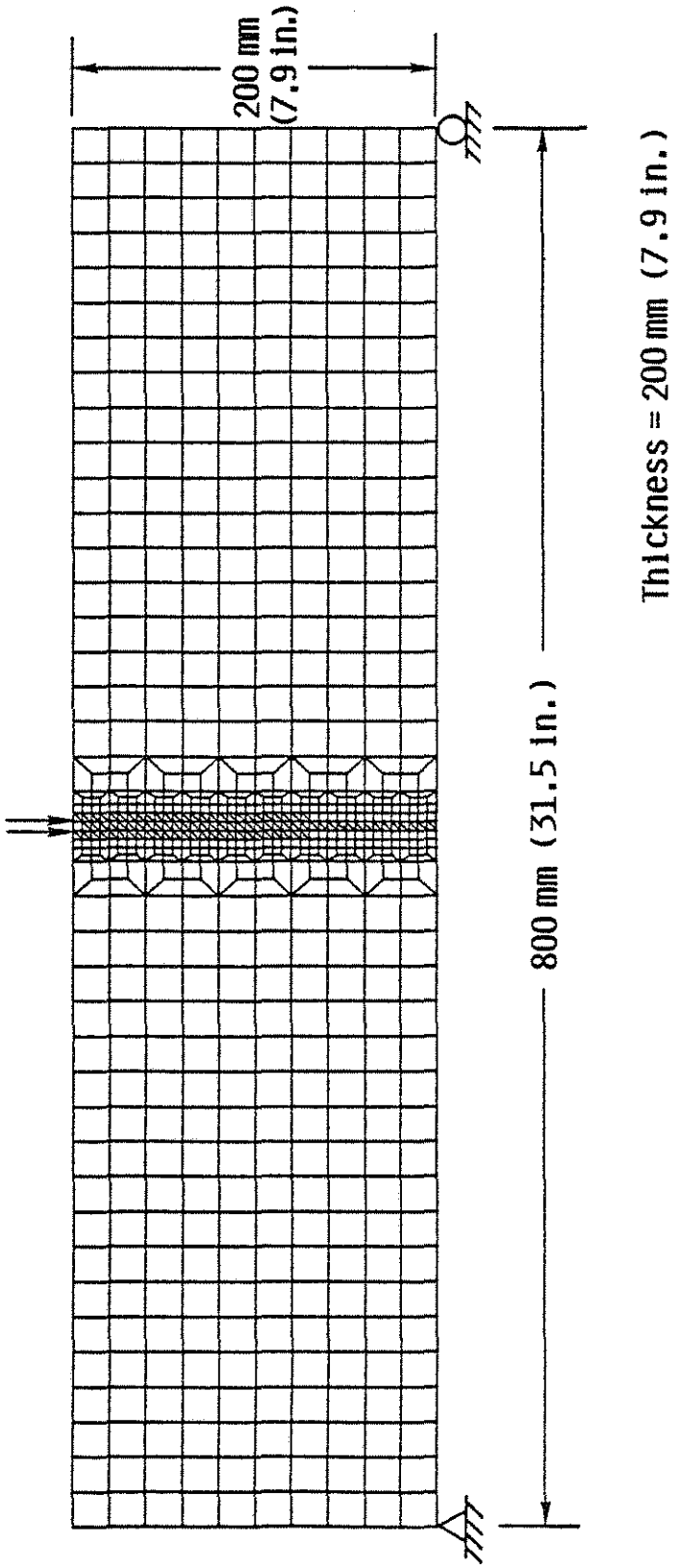

Figure 3.2. Finite Element Model of Notched Beam.

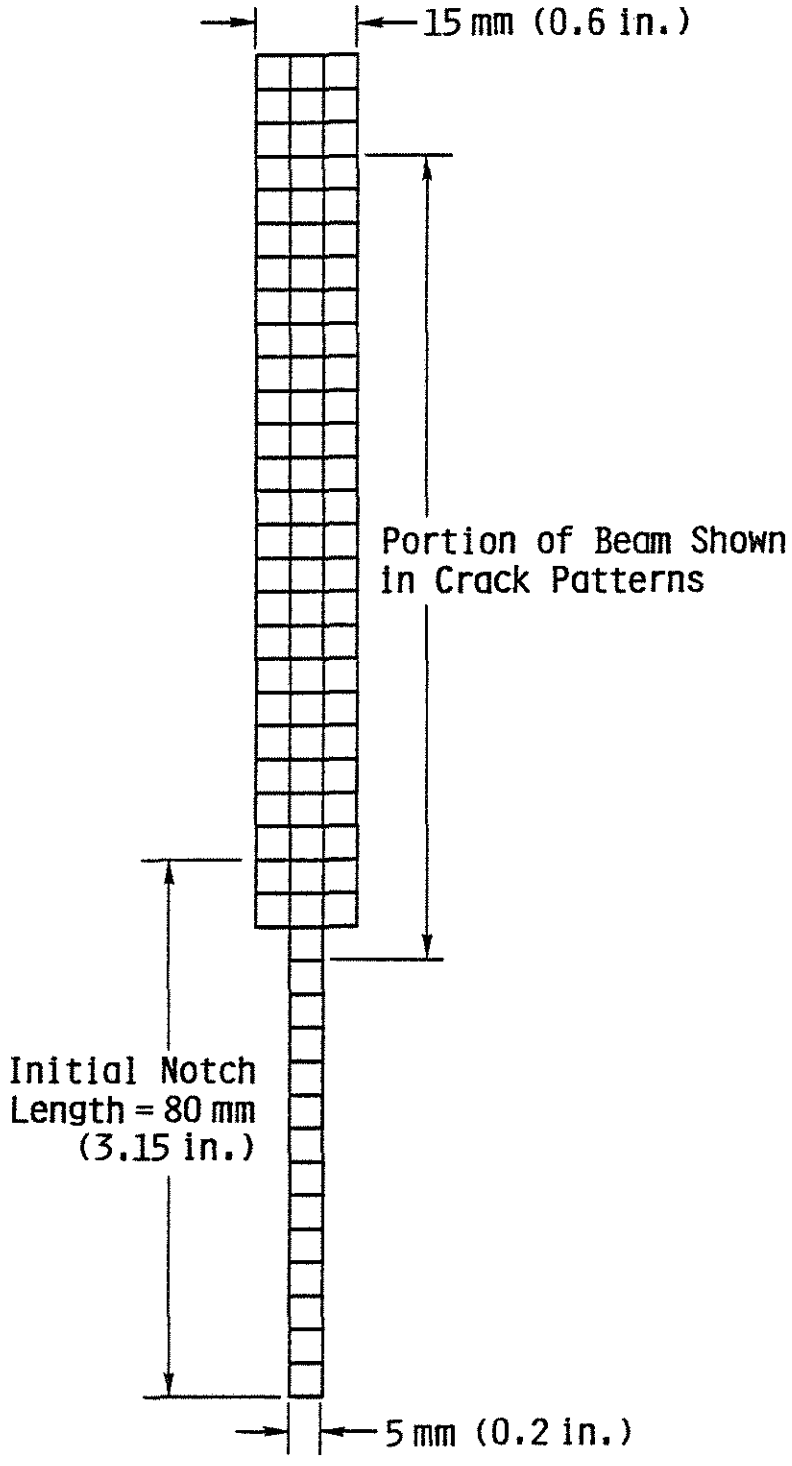

Figure 3.3. Nonlinear Portion of Finite Element Grid.

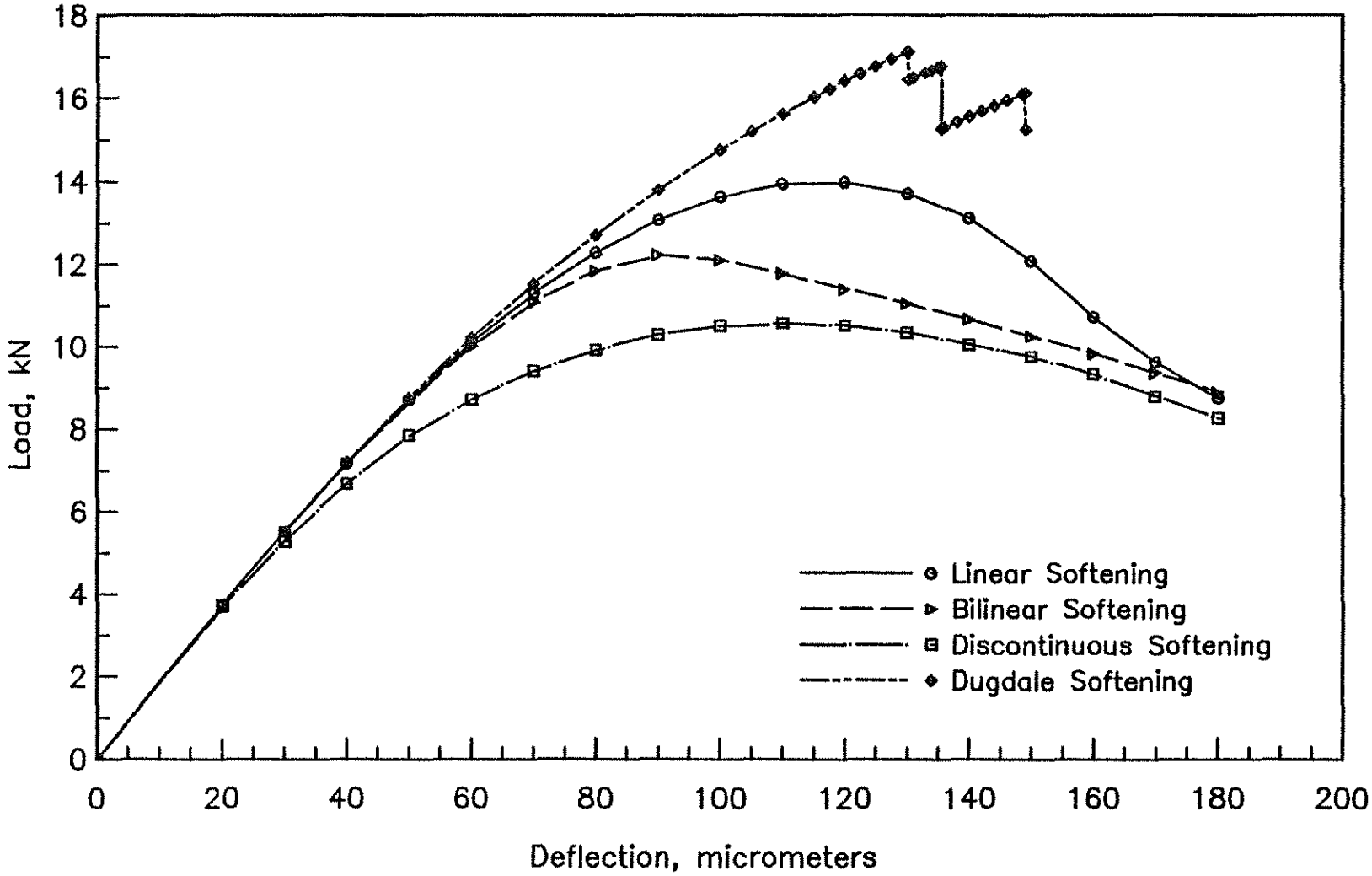

Figure 3.4. Effect of Assumed Concrete Tensile Response on Load-Deflection Curves (1kN = 0.225 kip, 1 μm = 3.9 x 10^{-5} in.).

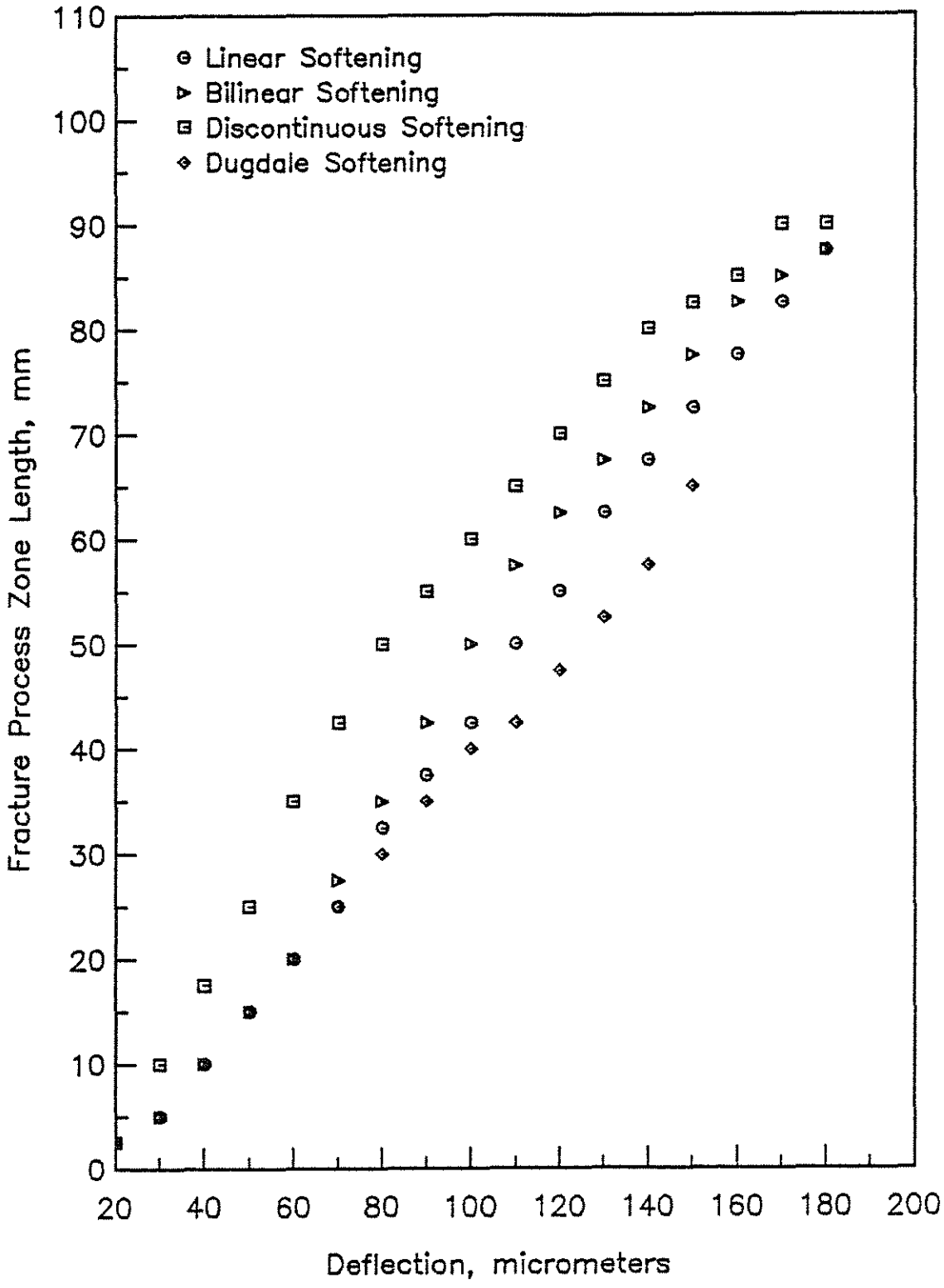

Figure 3.5. Effect of Assumed Concrete Tensile Response on Fracture Process Zone Length (1 mm = .039 in., 1 μm = 3.9 x 10^{-5} in.).

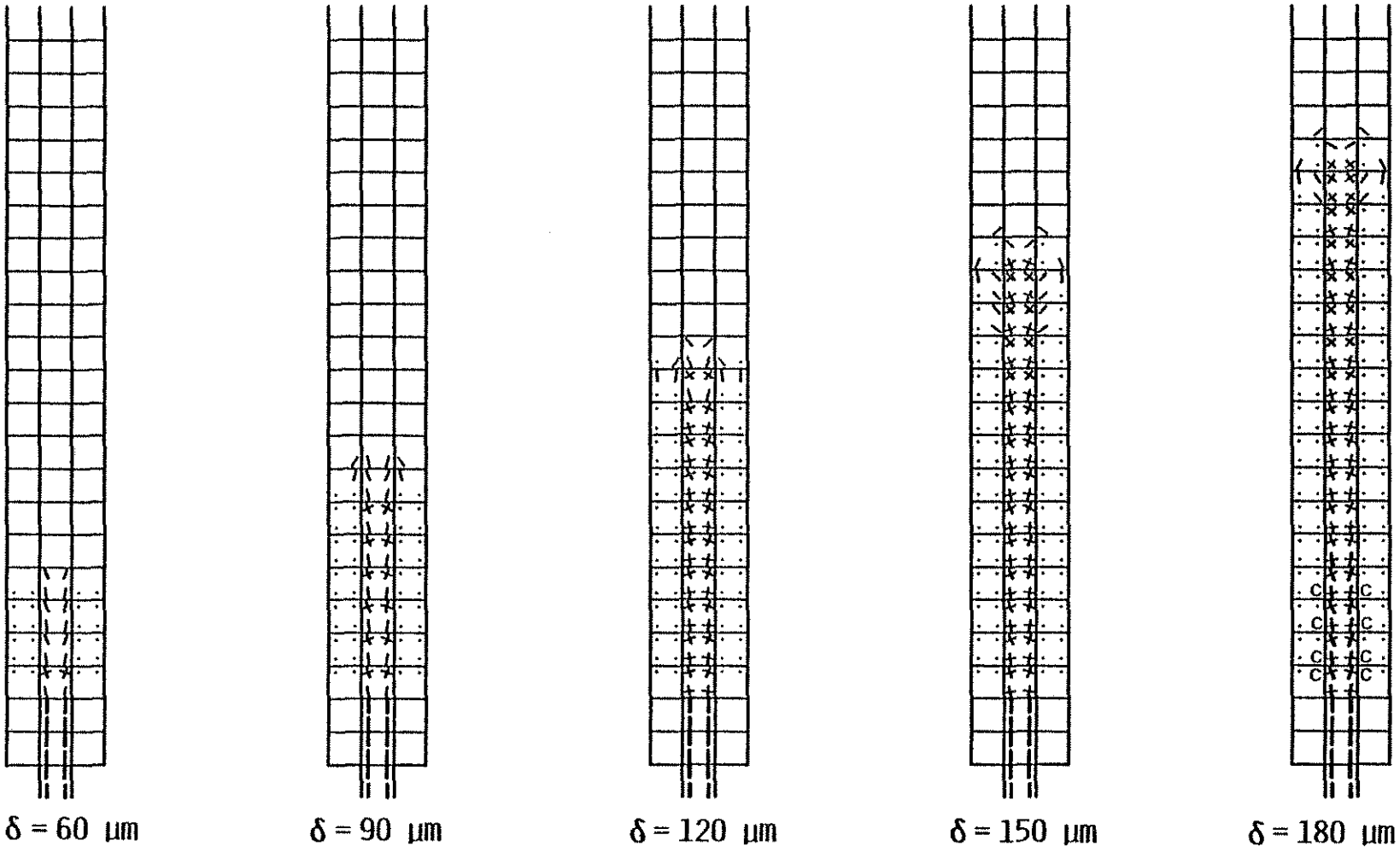

Figure 3.6. Crack Patterns for Beam with Linear Softening.

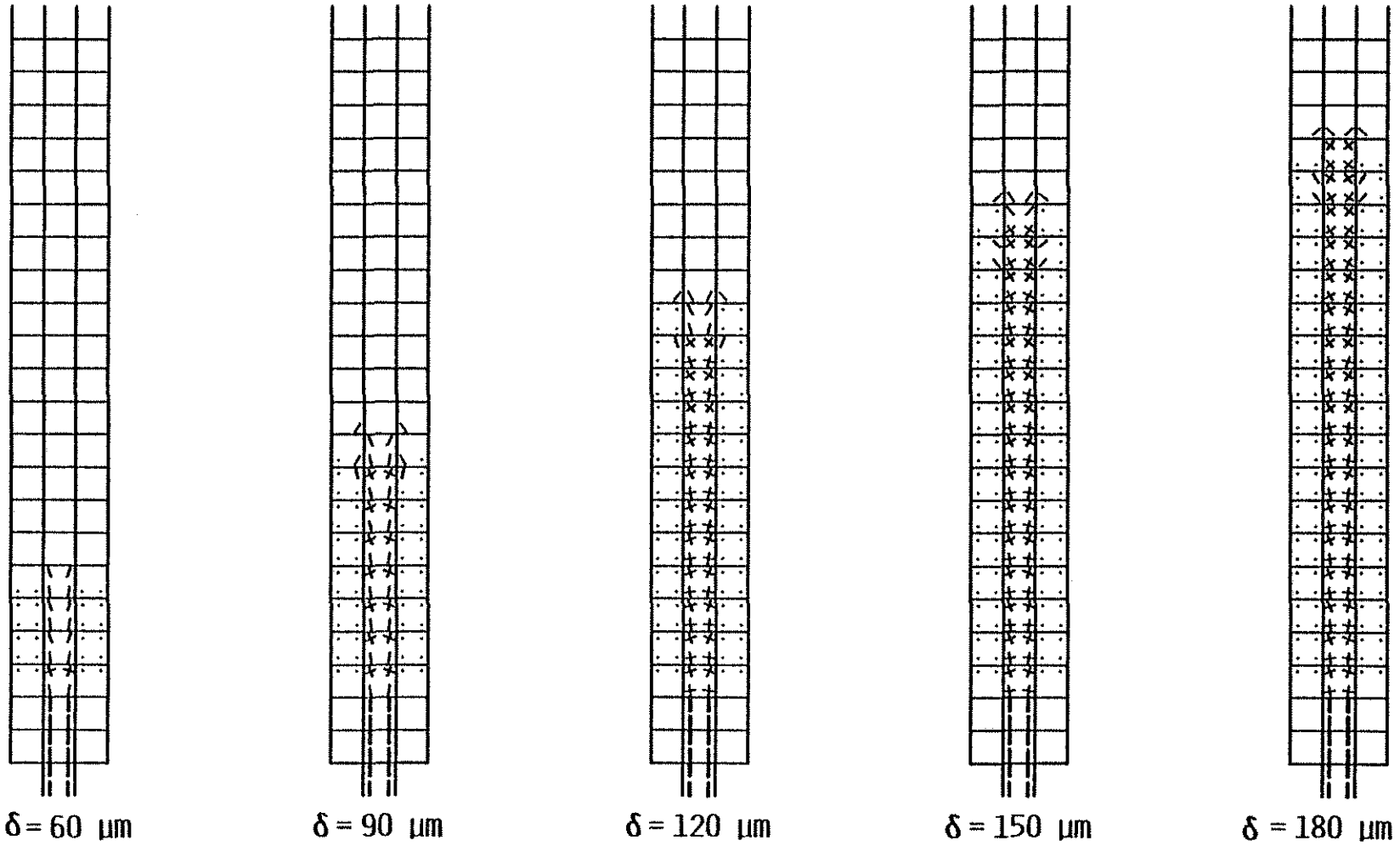

Figure 3.7. Crack Patterns for Beam with Bilinear Softening.

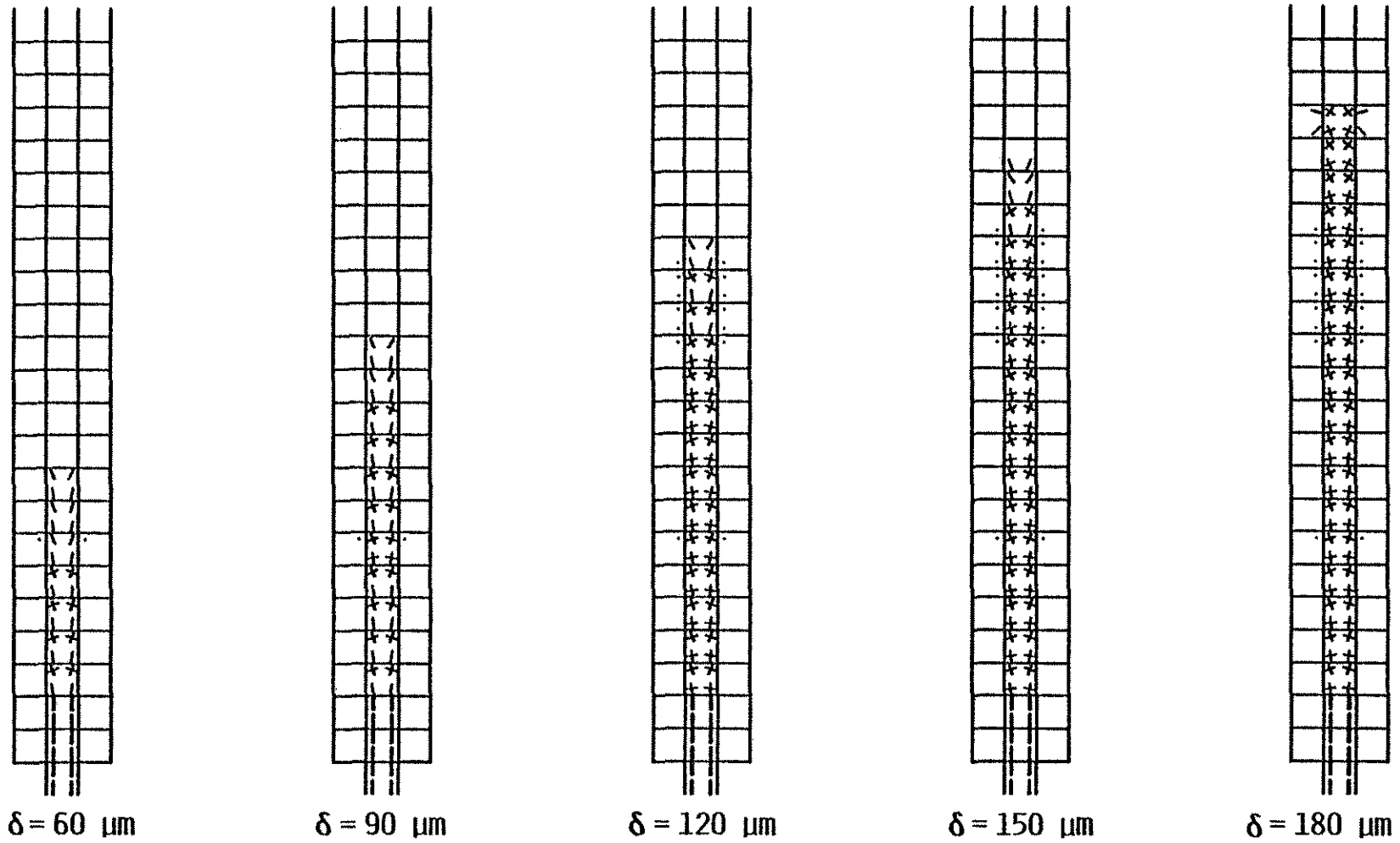

Figure 3.8. Crack Patterns for Beam with Discontinuous Softening.

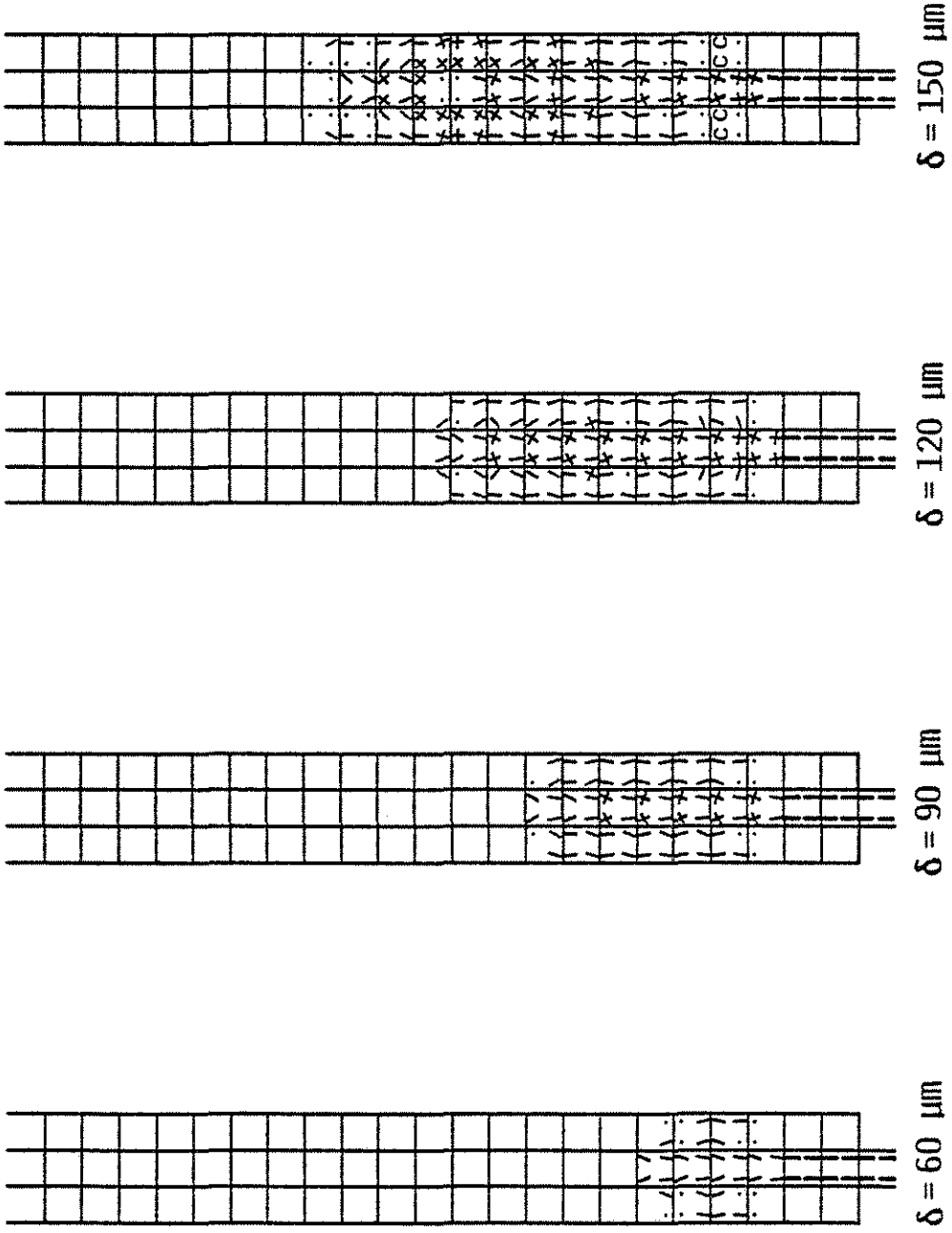

Figure 3.9. Crack Patterns for Beam with Dugdale Softening.

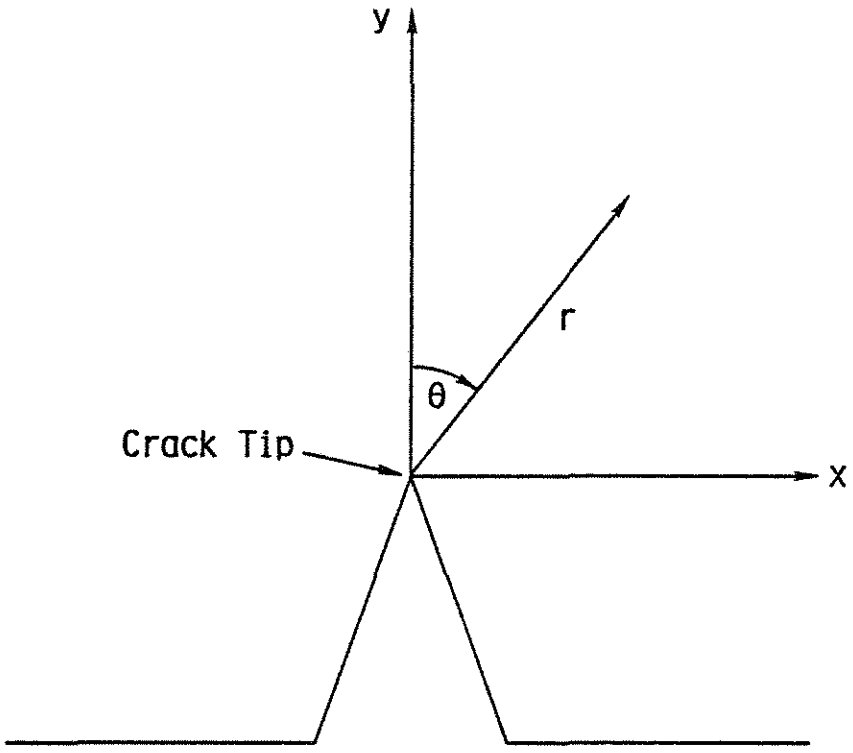

Figure 3.10. Coordinate System Describing Region Ahead of a Sharp Crack Tip.

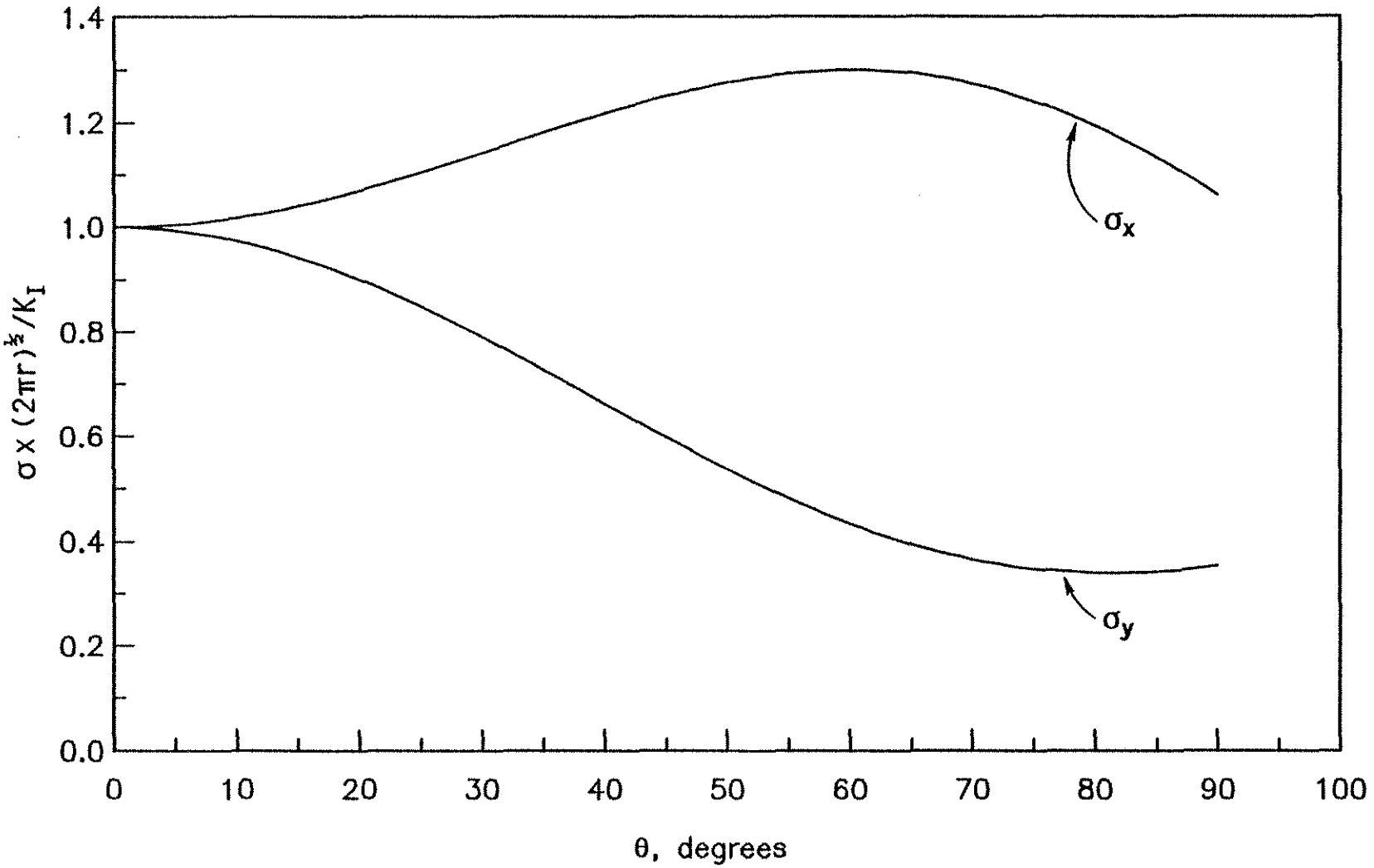

Figure 3.11. Stress Components Ahead of a Sharp Crack Tip.

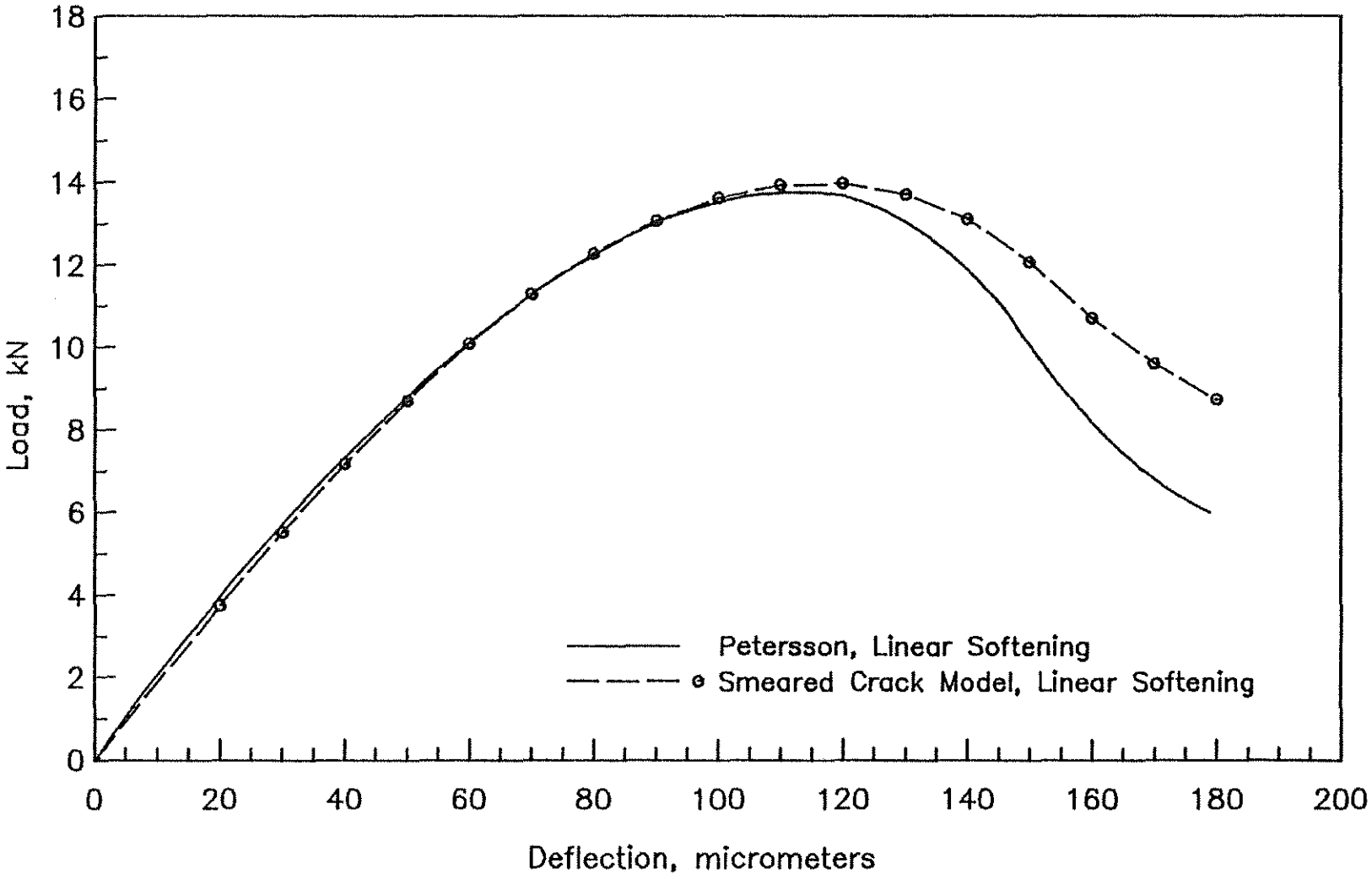

Figure 3.12. Comparison of Load-Deflection Curves of Discrete and Smeared Crack Models with Linear Softening (1 kN = 0.225 kip, 1 μm = 3.9 x 10^{-5} in.).

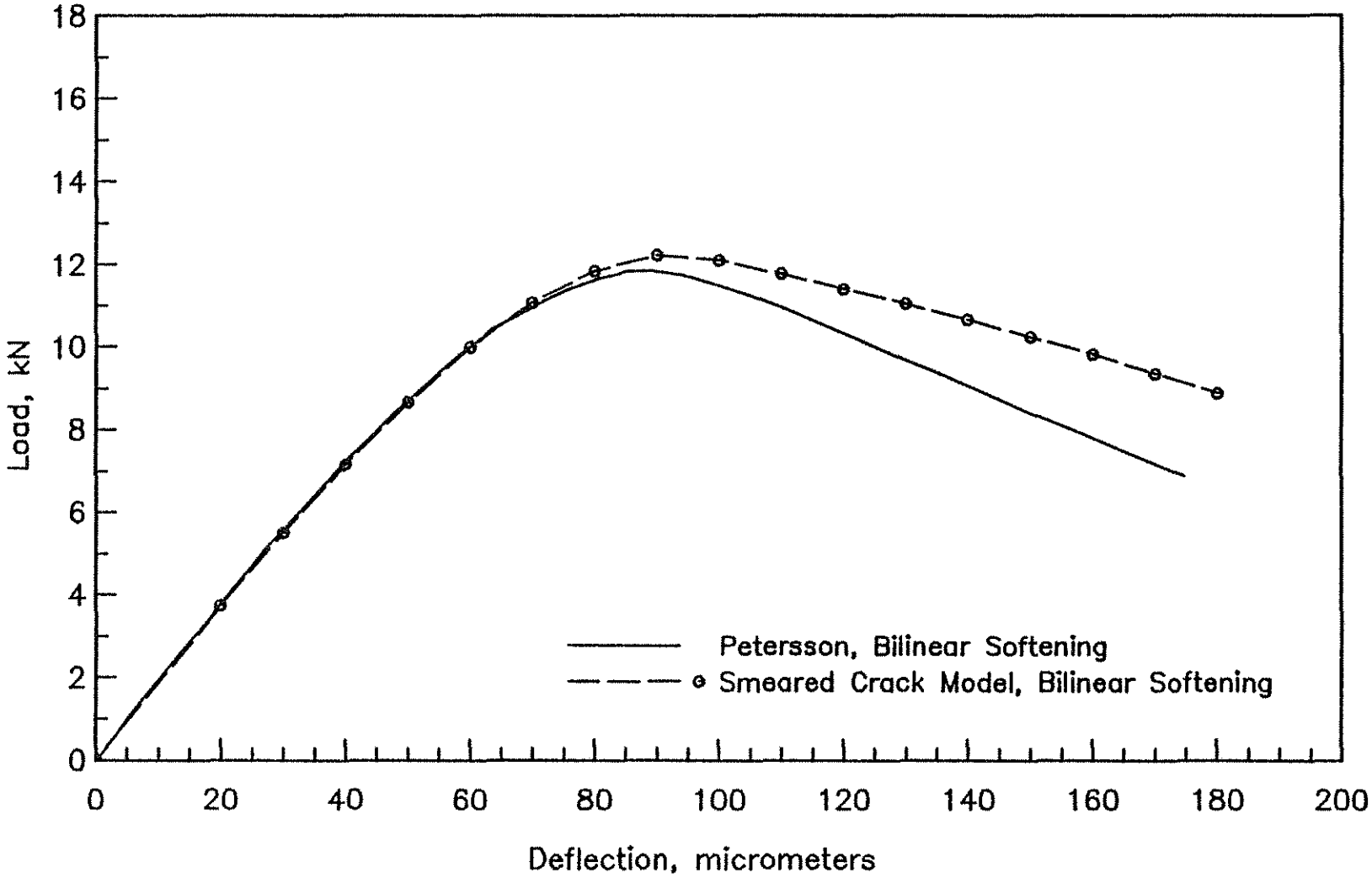

Figure 3.13. Comparison of Load-Deflection Curves of Discrete and Smeared Crack Models with Bilinear Softening (1 kN = 0.225 kip, 1 μm = 3.9 x 10^{-5} in.).

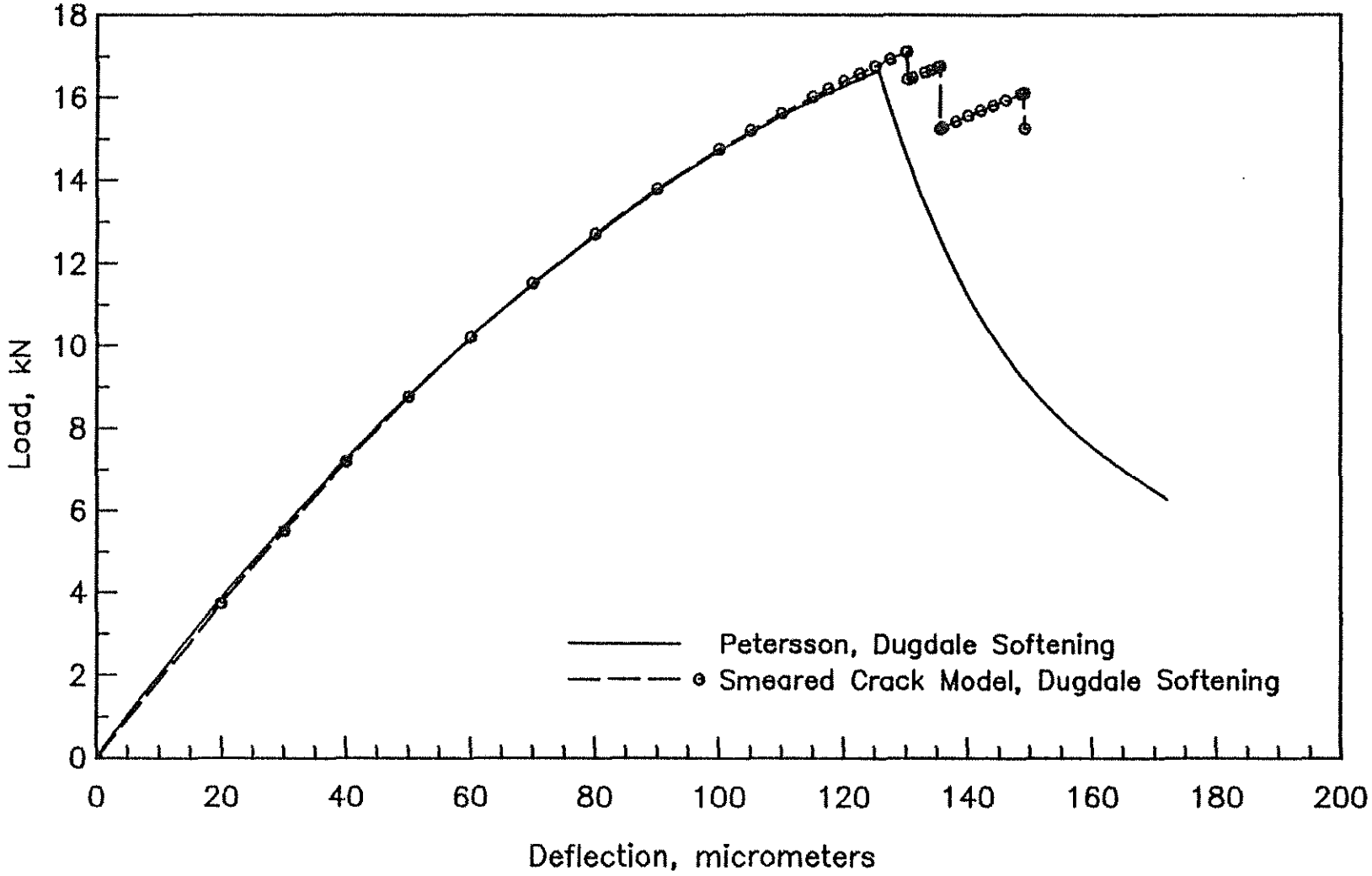

Figure 3.14. Comparison of Load-Deflection Curves of Discrete and Smeared Crack Models with Dugdale Softening (1 kN = 0.225 kip, 1 μm = 3.9×10^{-5} in.).

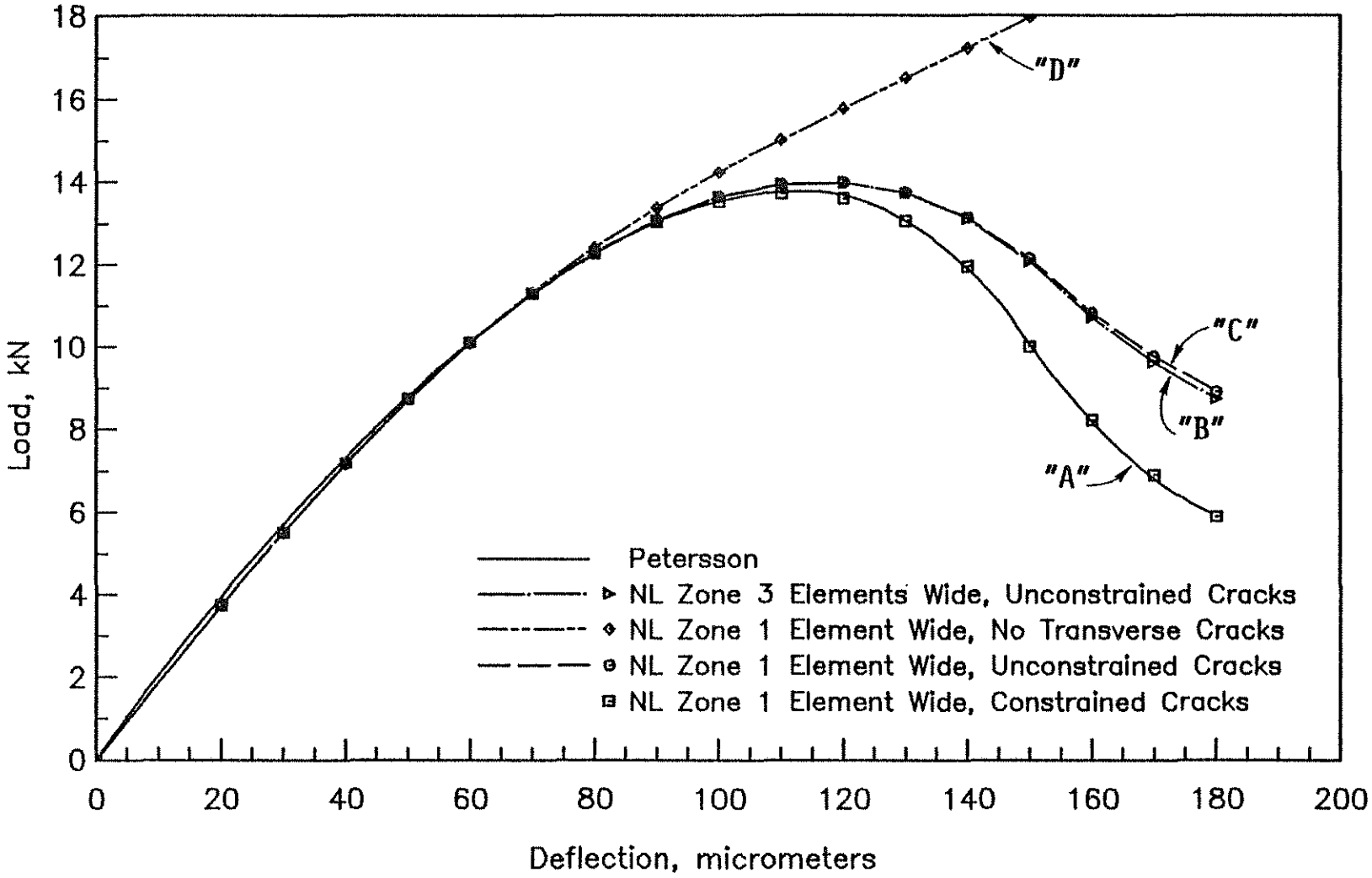

Figure 3.15. Effect of Crack Angle Constraint and Width of Nonlinear Zone on Load-Deflection Curves of Beam with Linear Softening (1 kN = 0.225 kip, 1 μm = 3.9 x 10^{-5} in.).

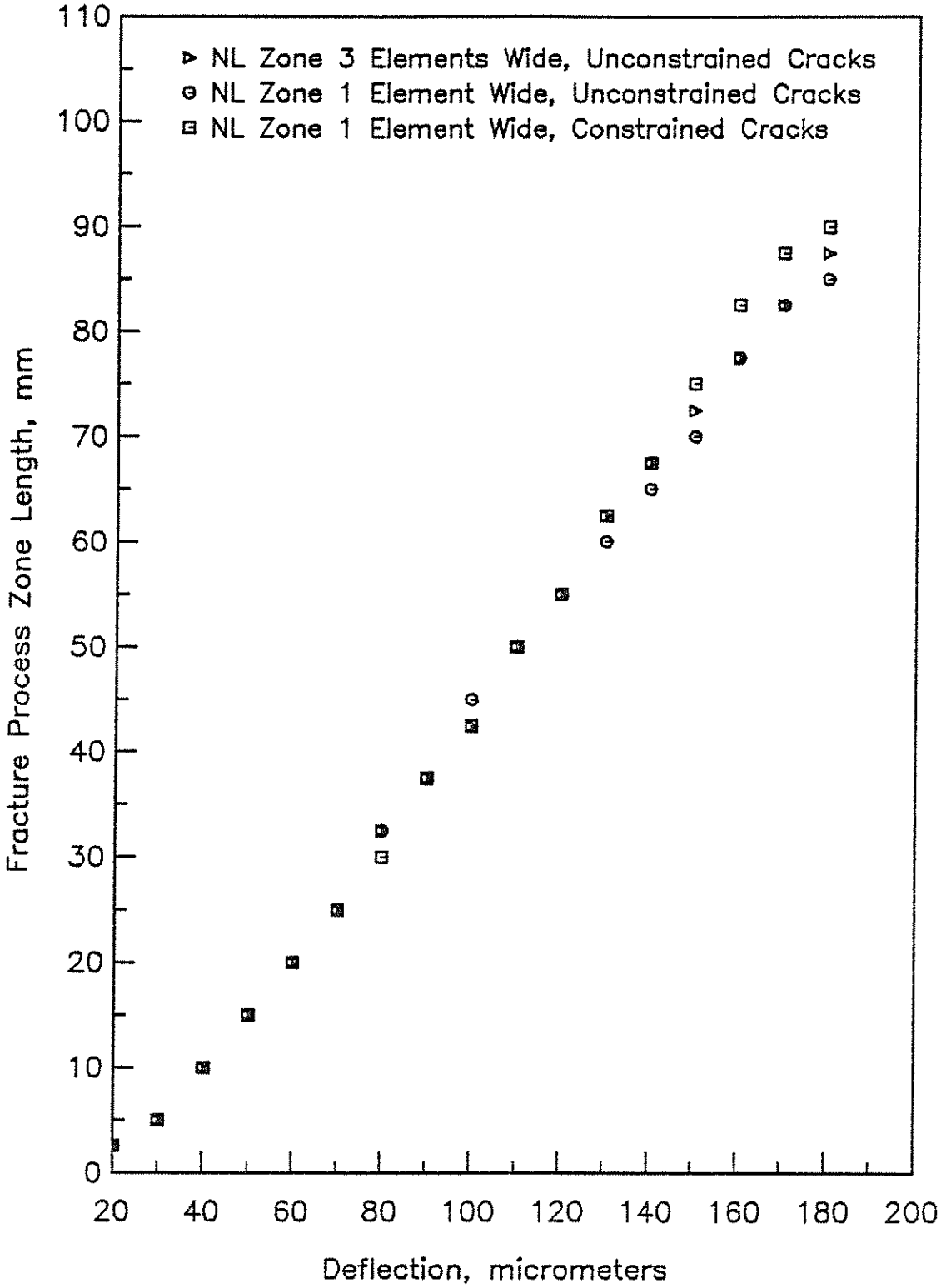

Figure 3.16. Effect of Crack Angle Constraint and Width of Nonlinear Zone on Fracture Process Zone Length in Beam with Linear Softening (1 mm = .039 in., 1 μm = 3.9 x 10^{-5} in.).

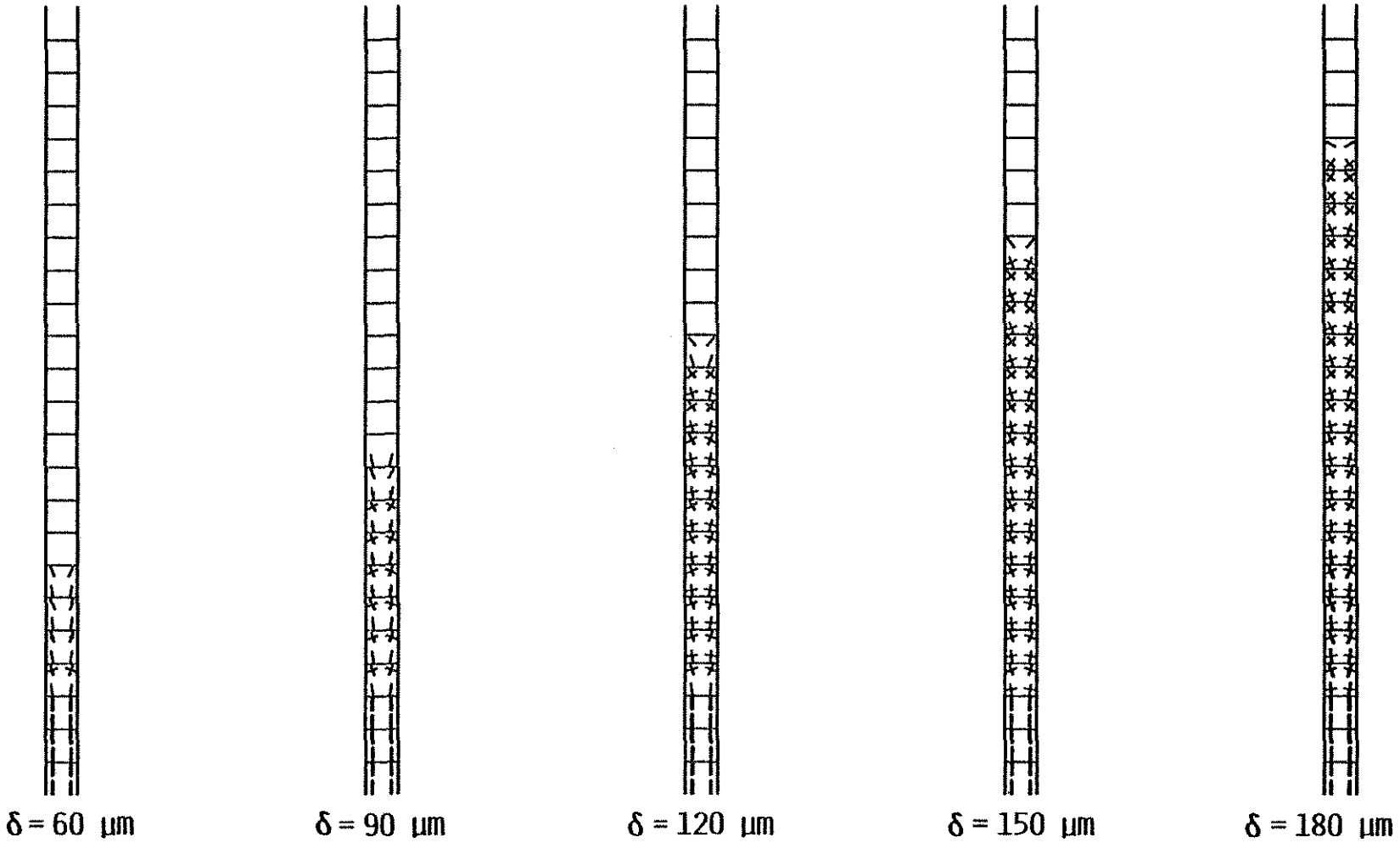

Figure 3.17. Crack Patterns for Beam with Linear Softening, 1 Element Wide Nonlinear Zone, Unconstrained Cracks.

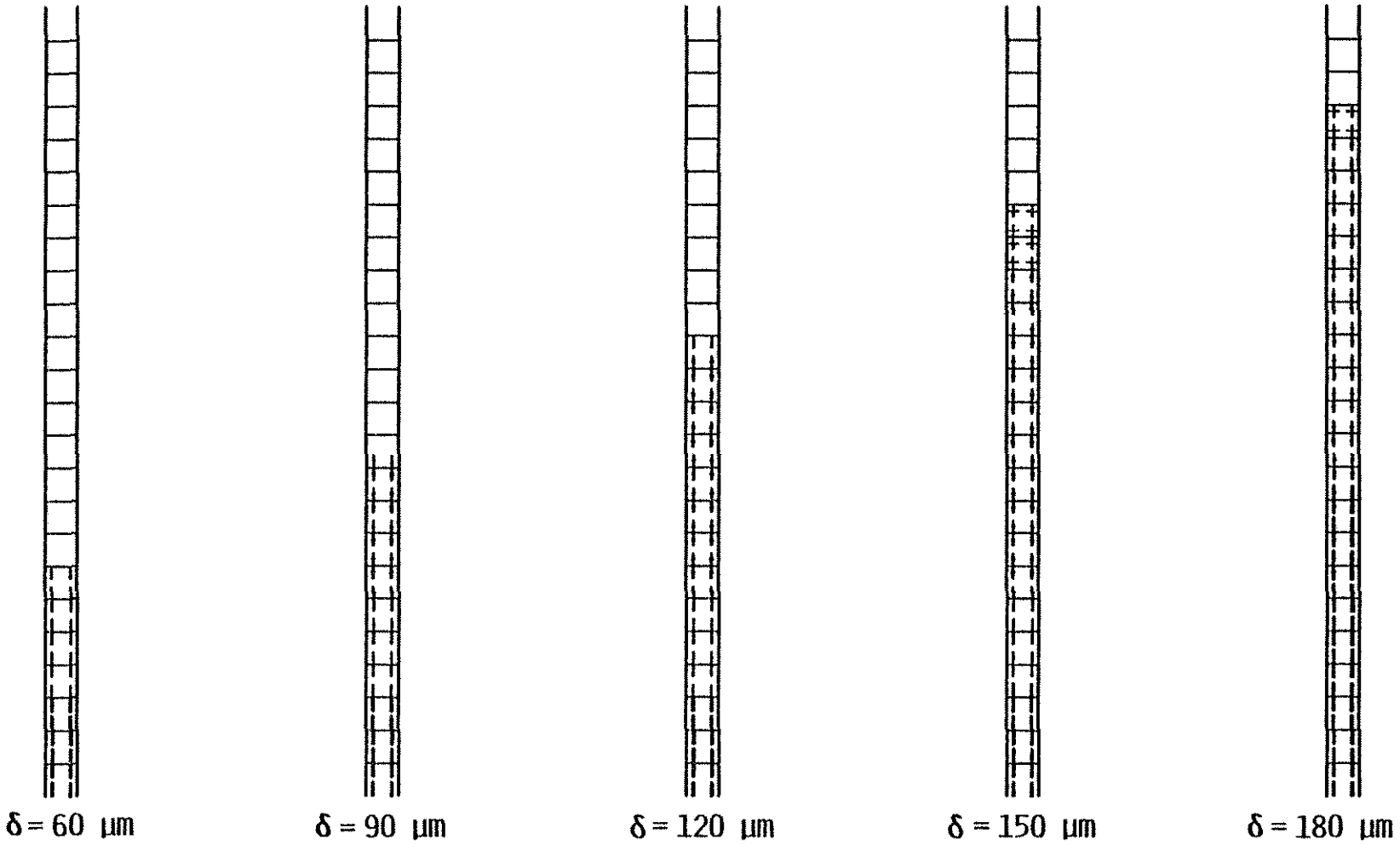

Figure 3.18. Crack Patterns for Beam with Linear Softening, 1 Element Wide Nonlinear Zone, Constrained Cracks.

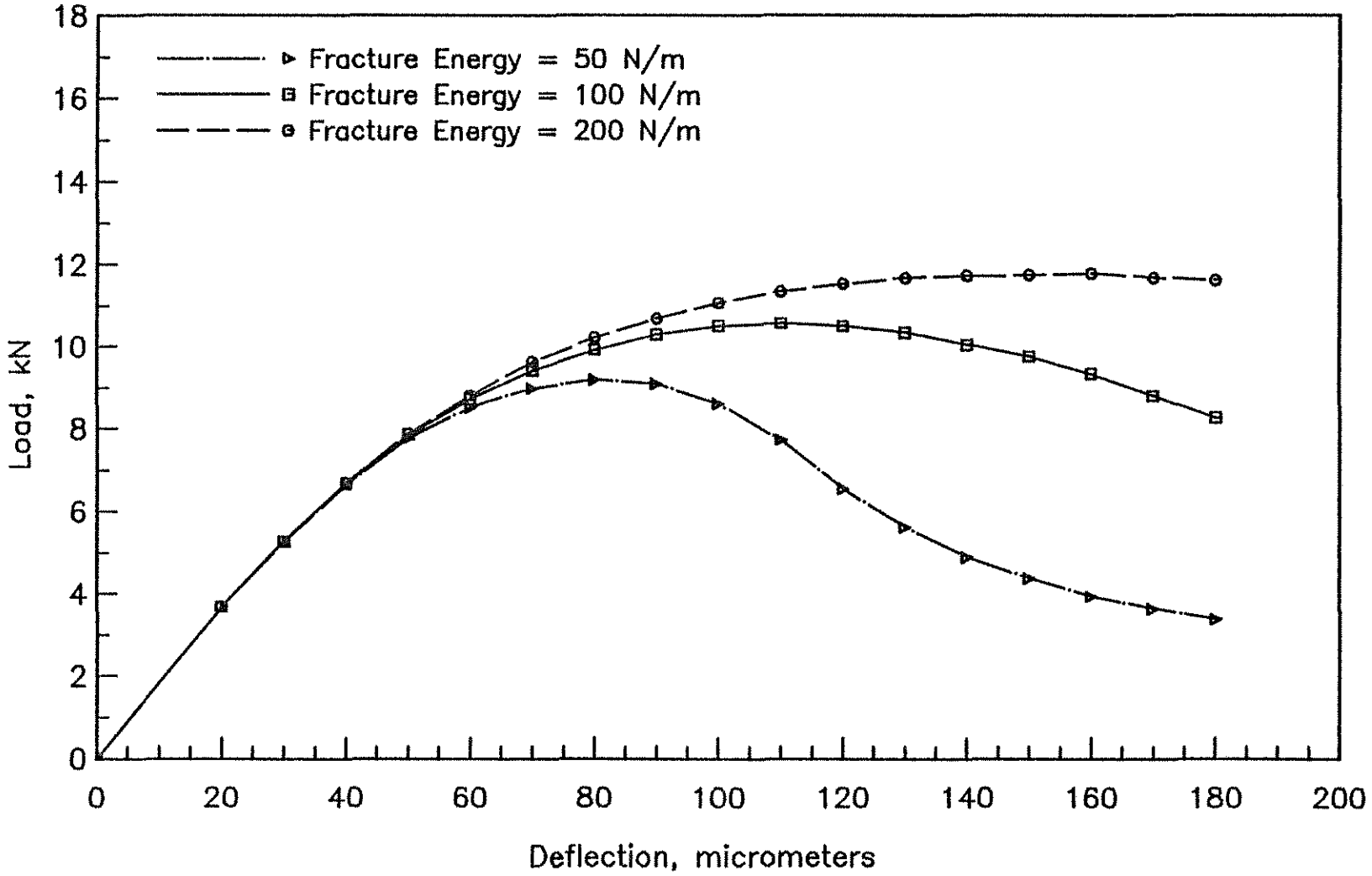

Figure 3.19. Effect of Fracture Energy on Load-Deflection Curves of Beam with Discontinuous Softening (1 N/m = .0057 lb/in, 1 kN = 0.225 kip, 1 μm = 3.9×10^{-5} in.).

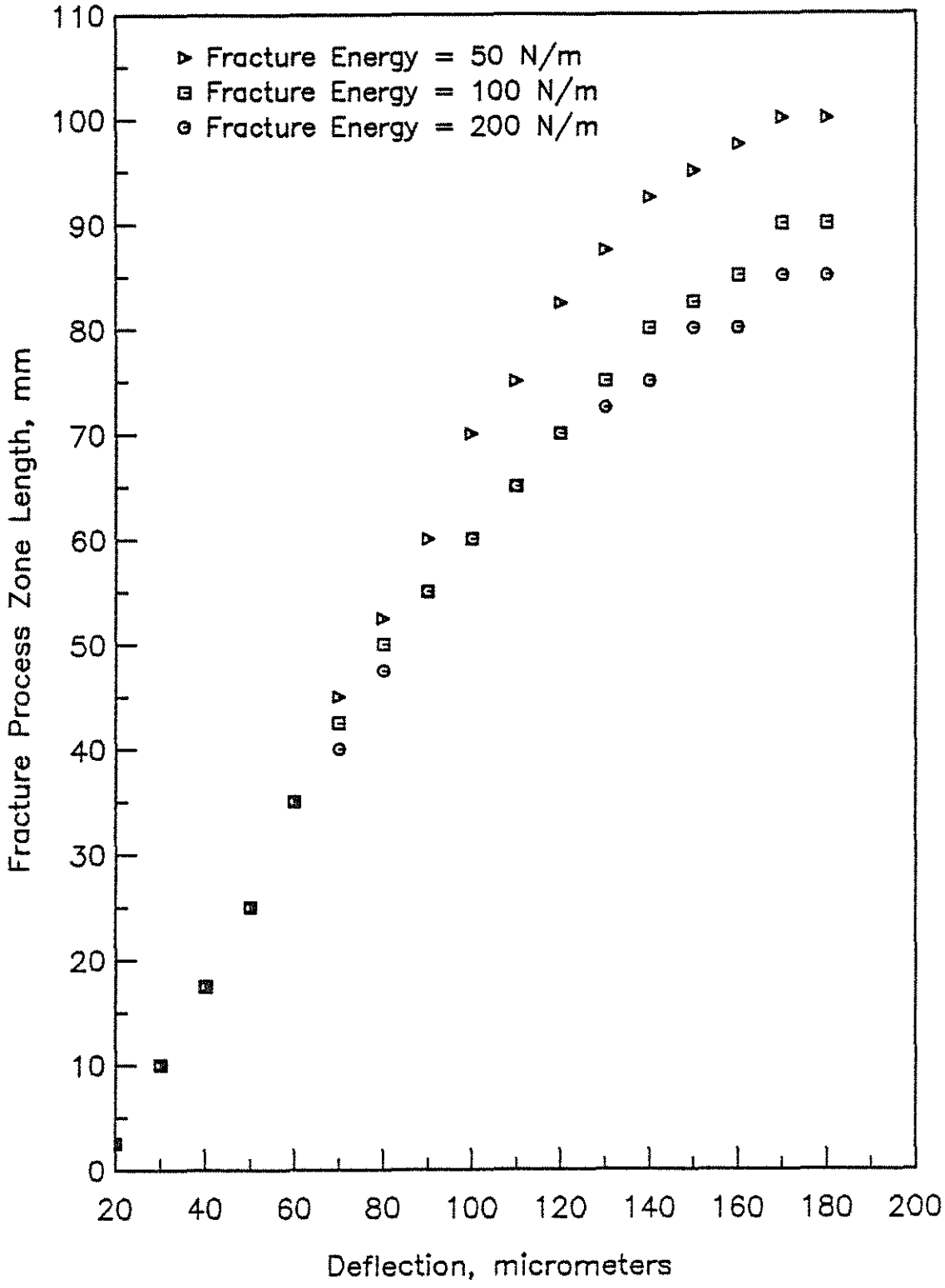

Figure 3.20. Effect of Fracture Energy on Fracture Process Zone Length in Beam with Discontinuous Softening (1 N/m = .0057 lb/in, 1kN = 0.225 kip, 1 μm = 3.9×10^{-5} in.).

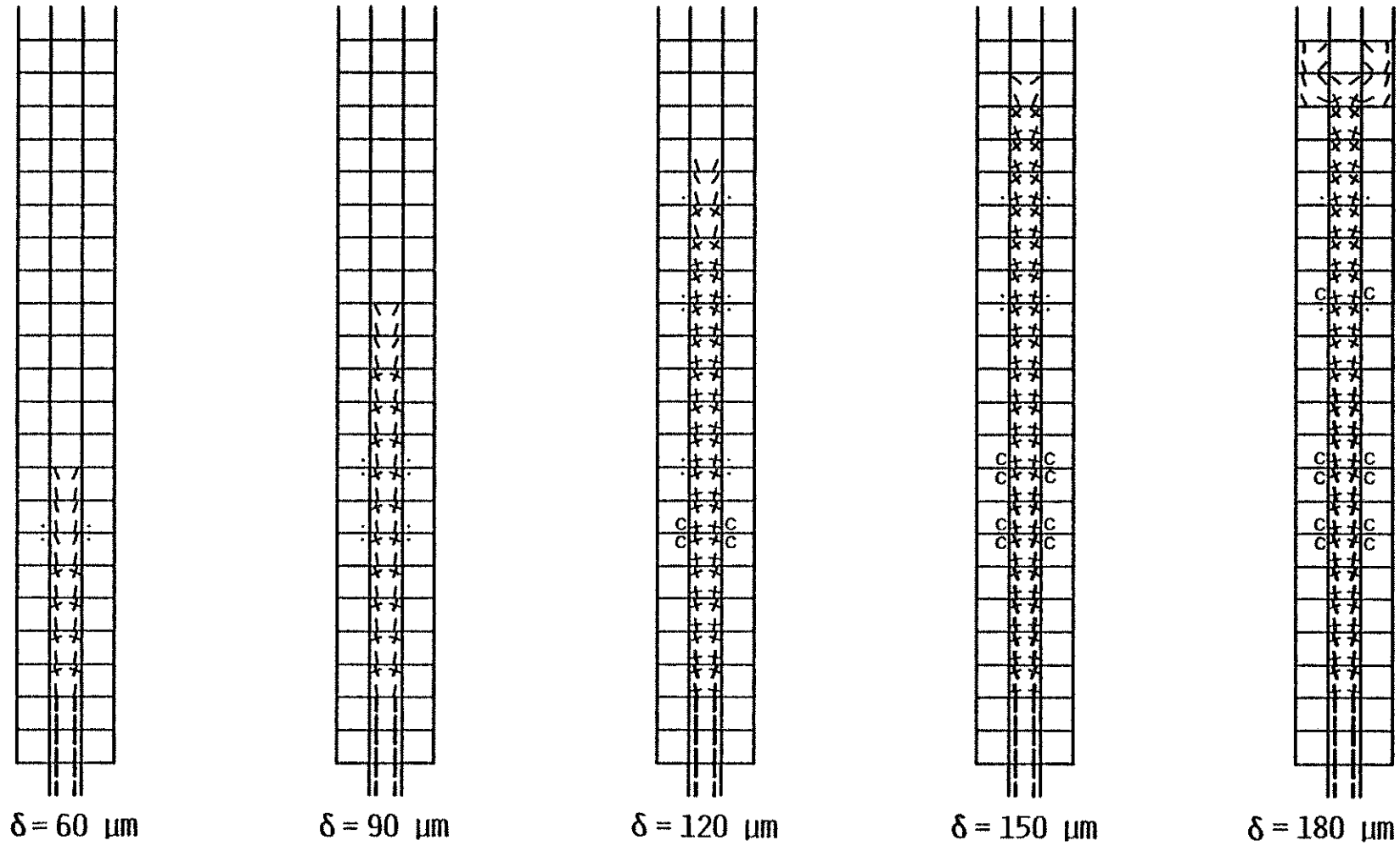

Figure 3.21. Crack Patterns for Beam with Discontinuous Softening, Fracture Energy = 50 N/m (0.285 lb/in).

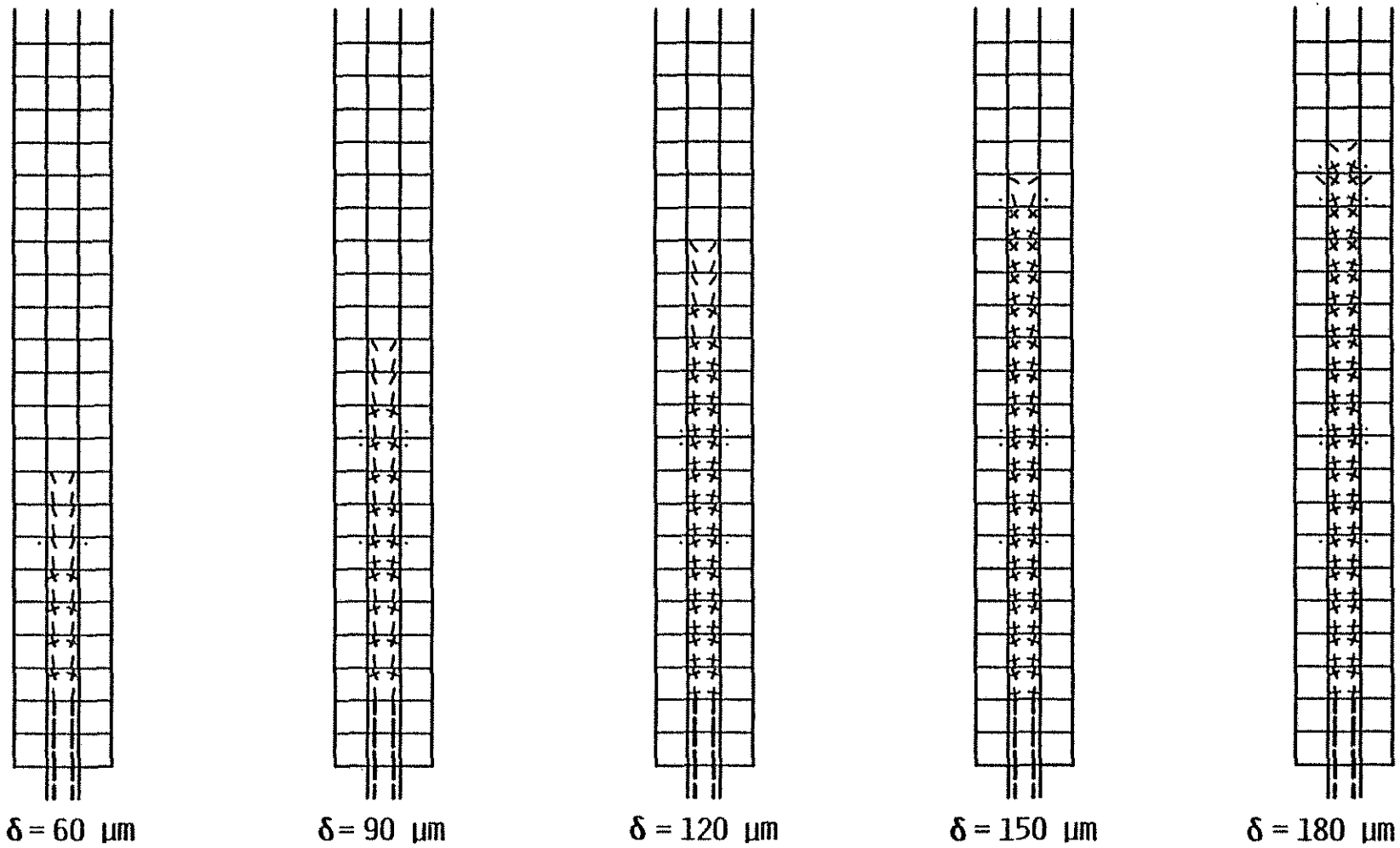

Figure 3.22. Crack Patterns for Beam with Discontinuous Softening, Fracture Energy = 200 N/m (1.14 lb/in).

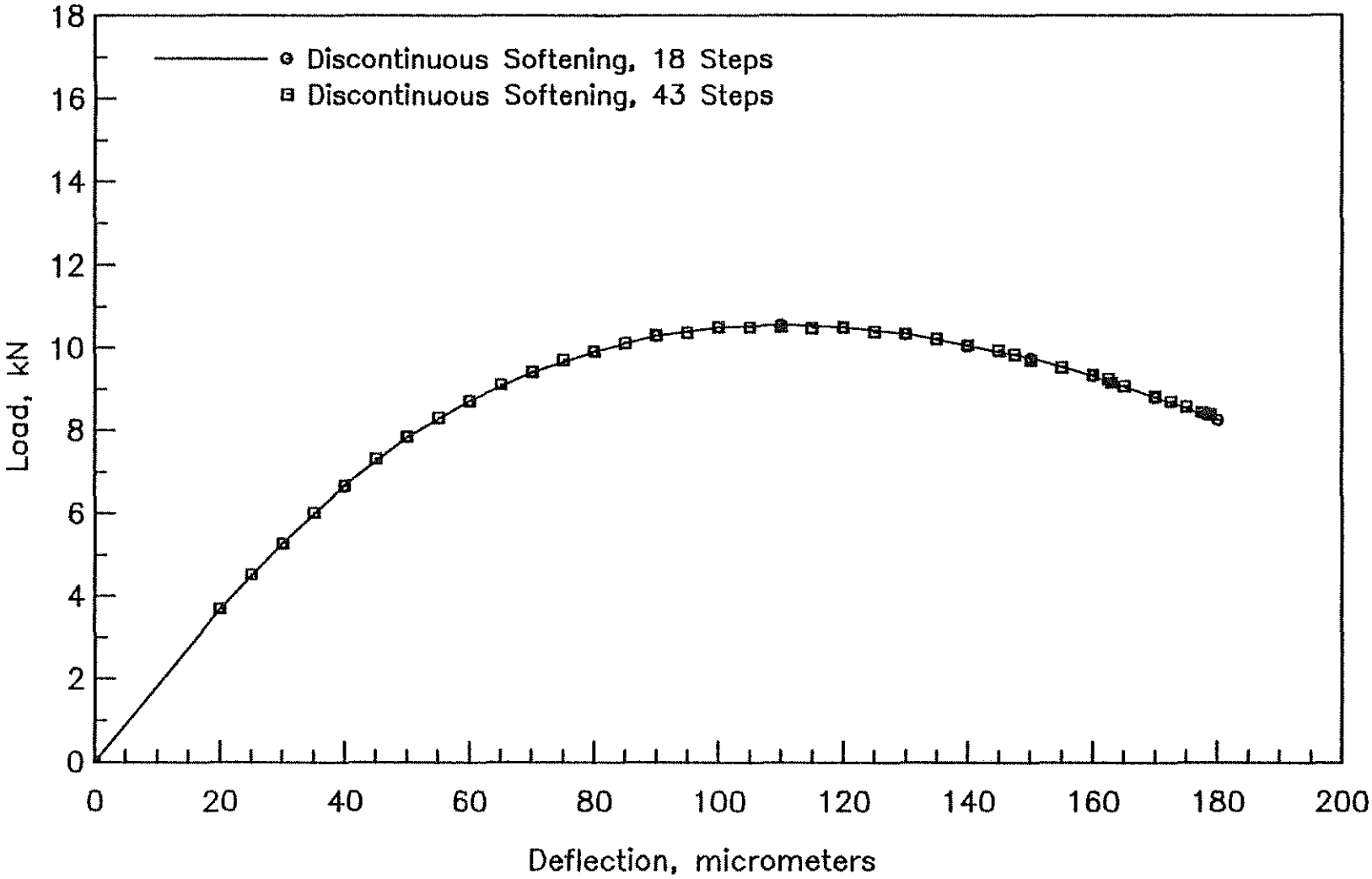

Figure 3.23. Effect of Load Increment Size on Load-Deflection Curves of Beam with Discontinuous Softening (1 kN = 0.225 kip, 1 μm = 3.9×10^{-5} in.).

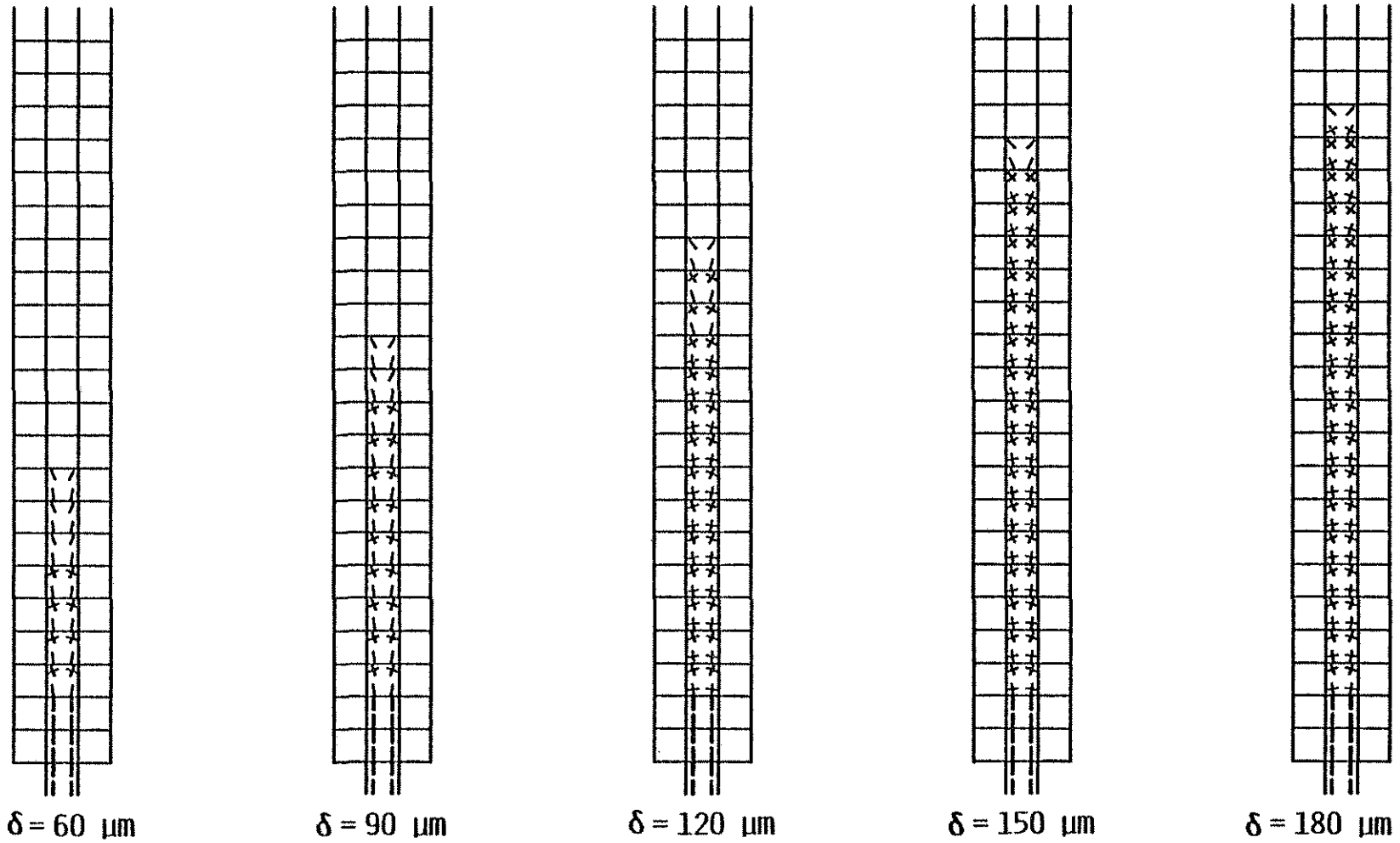

Figure 3.24. Crack Patterns for Beam with Discontinuous Softening, Load Applied in Small Increments (43 Steps) (1 kN = 0.225 kip, 1 μm = 3.9 x 10^{-5} in.).

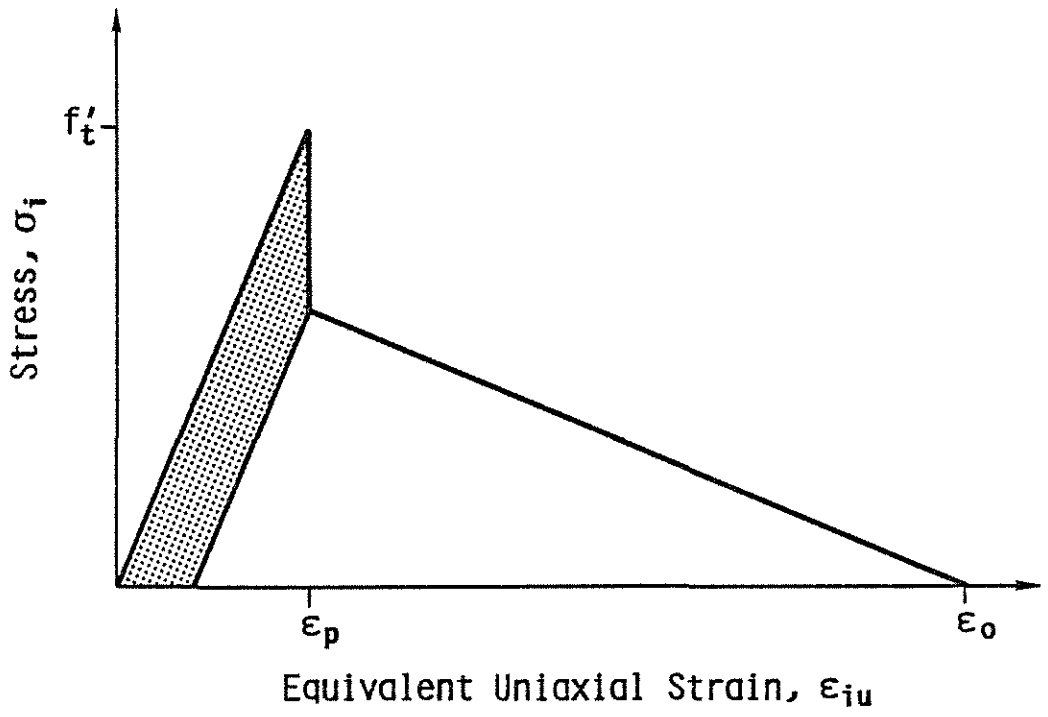

Figure 3.25. Nonrecoverable Energy after Crack Formation, Discontinuous Softening.

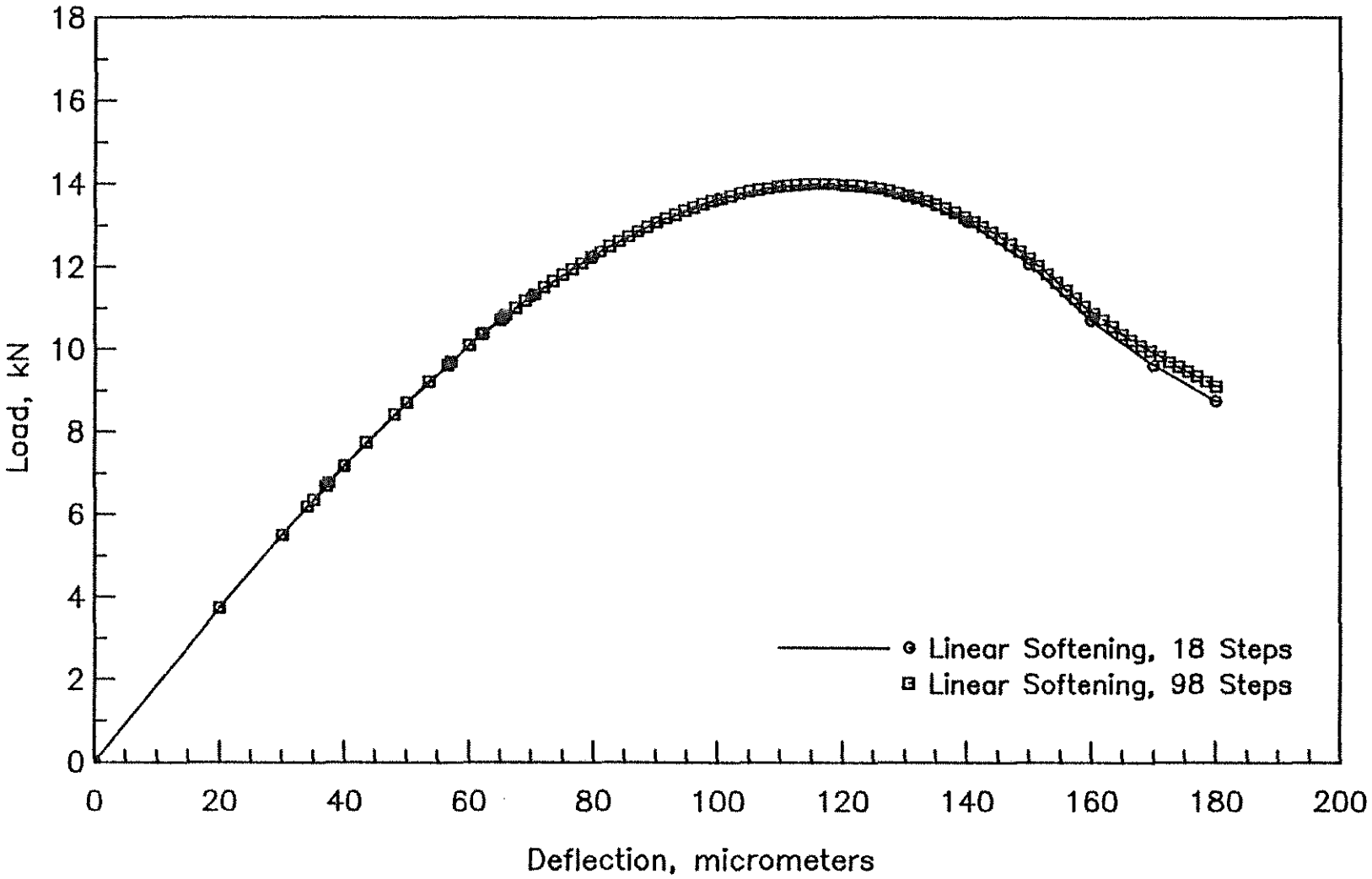

Figure 3.26. Effect of Load Increment Size on Load-Deflection Curves of Beam with Linear Softening, 3 Element Wide Nonlinear Zone, Unconstrained Cracks (1 kN = 0.225 kip, 1 μm = 3.9×10^{-5} in.).

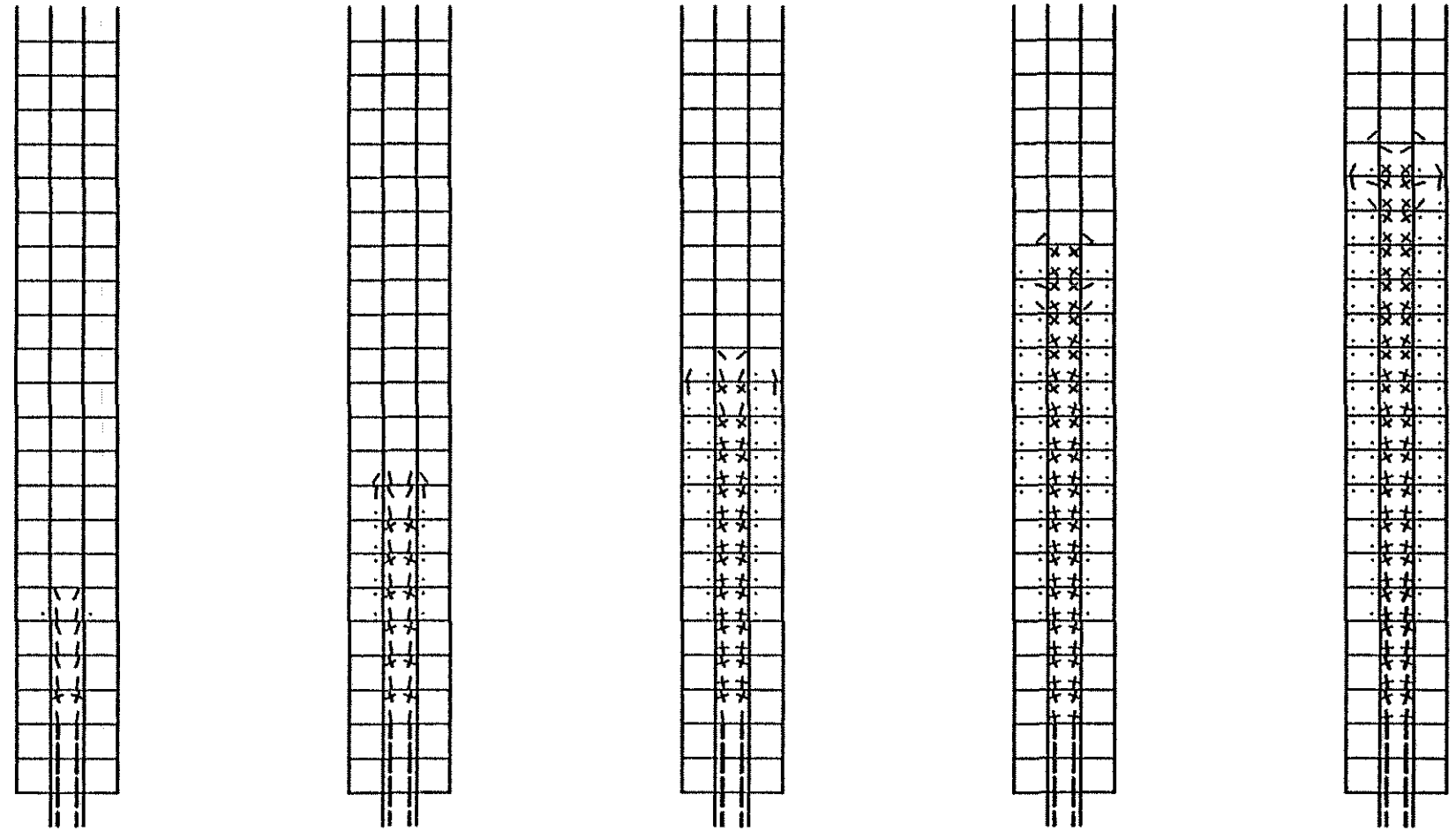

Figure 3.27. Crack Patterns for Beam with Linear Softening, Load Applied in Small Increments (98 Steps) (1 kN = 0.225 kip, 1 μm = 3.9×10^{-5} in.).

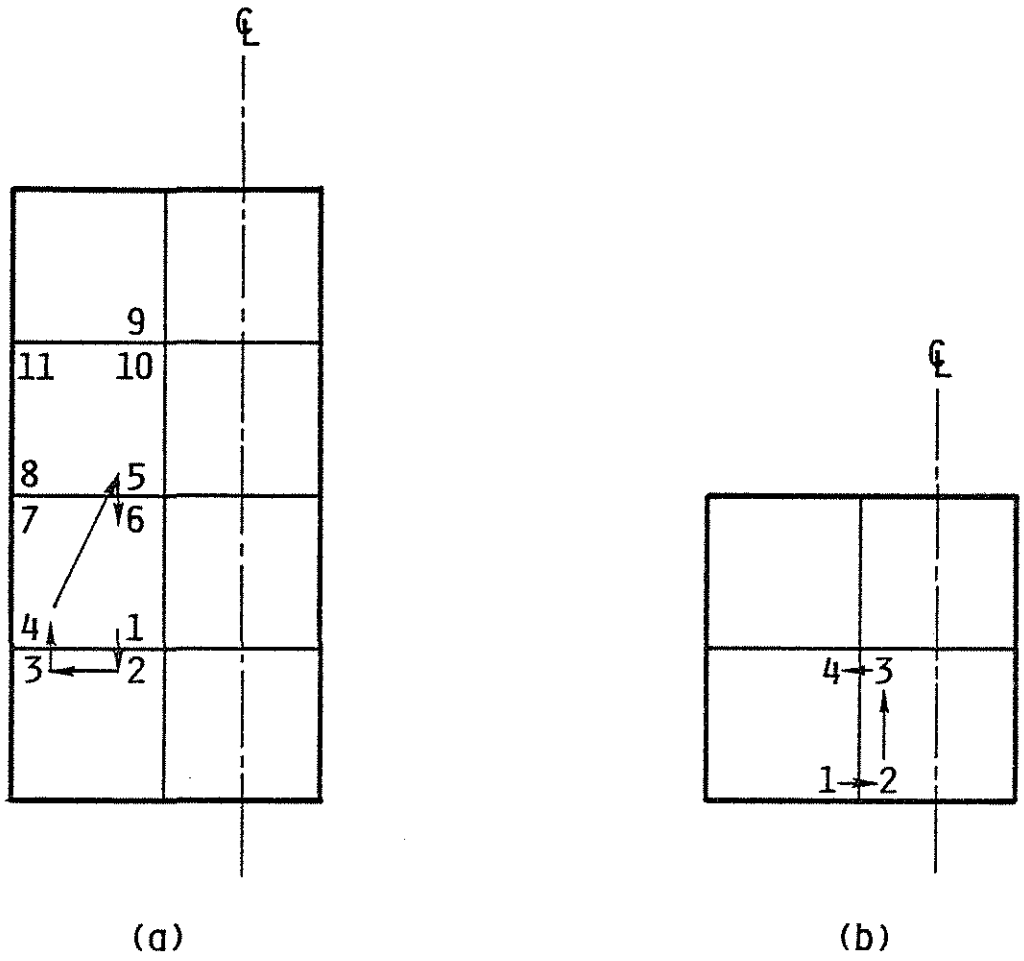

Figure 3.28. Cracking Sequence in Beam with Linear Softening: (a) Pattern in Side Column: (b) Pattern Along Boundary between Side and Center Column.

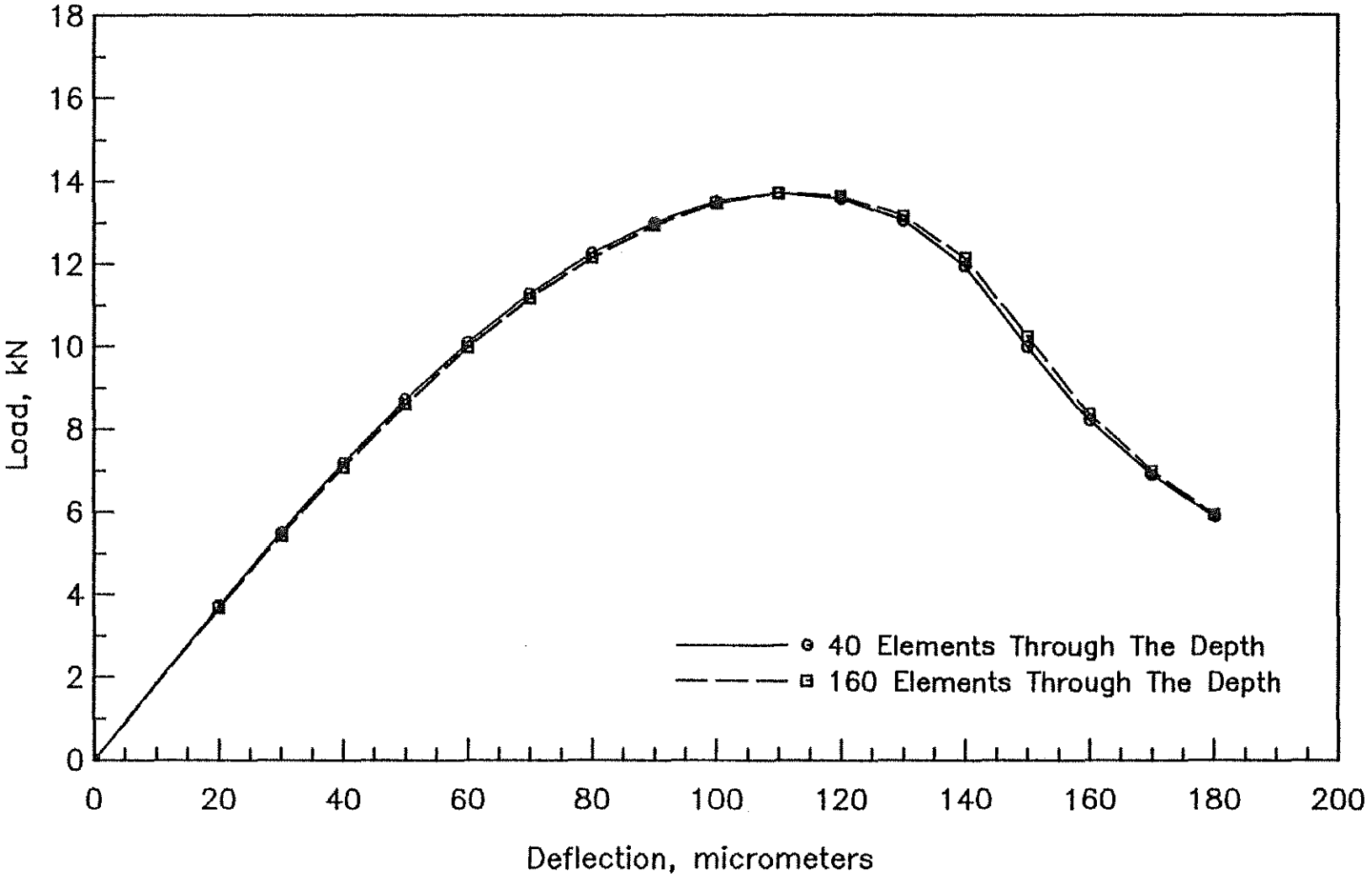

Figure 3.29. Effect of Grid Refinement on Load-Deflection Curves of Beam with Linear Softening, 1 Element Wide Nonlinear Zone, Constrained Cracks (1 kN = 0.225 kip, 1 μm = 3.9×10^{-5} in.).

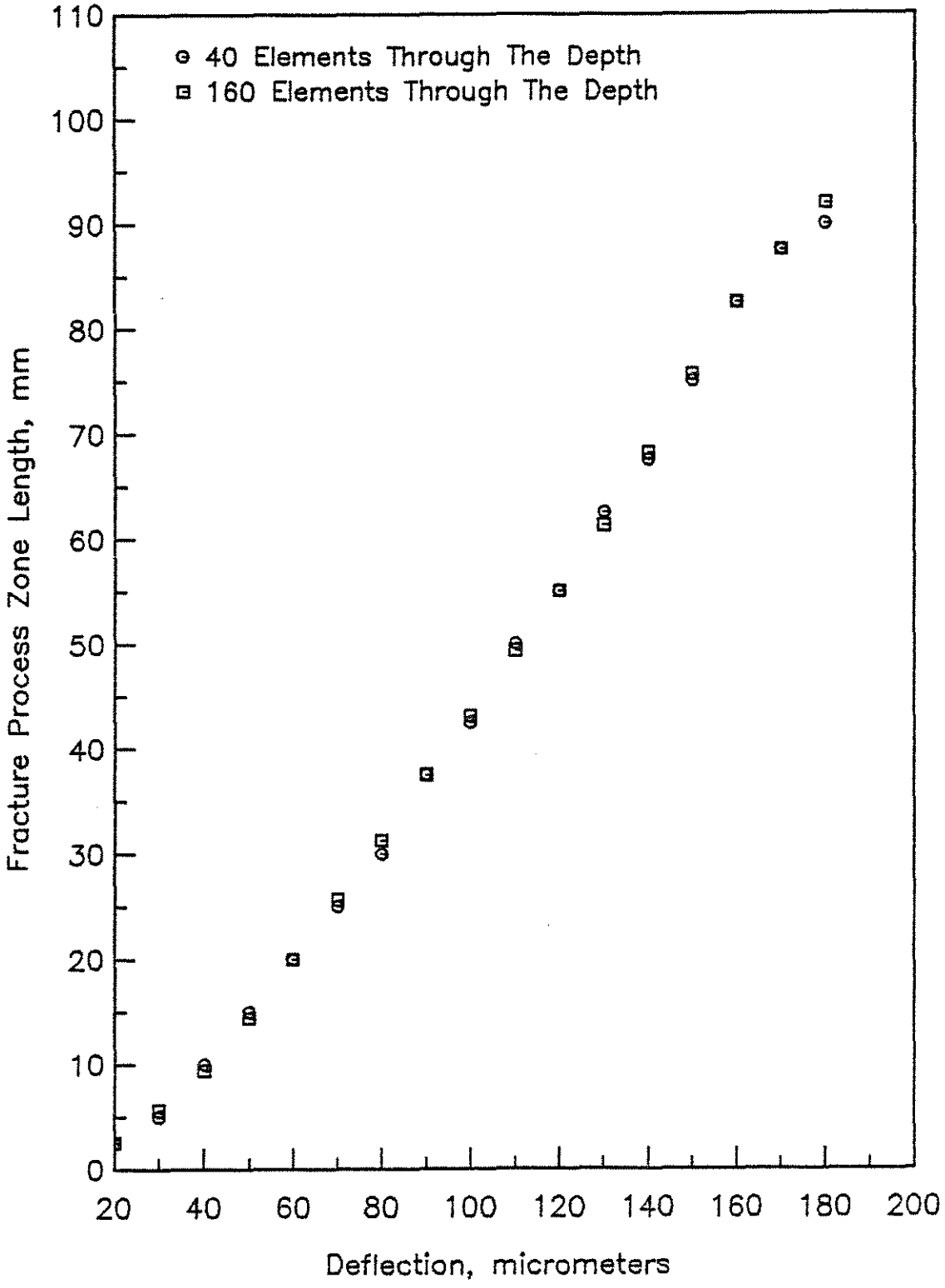

Figure 3.30. Effect of Grid Refinement on Fracture Process Zone Length in Beam with Linear Softening, 1 Element Wide Nonlinear Zone, Constrained Cracks (1 mm = .039 in., 1 μm = 3.9×10^{-5} in.).

Appendix A

NOTATION

$[B]$	matrix relating strains at a point to nodal displacements
C_f	f_t'/ε_0, slope of line relating strain due to opening of microcracks to stress normal to microcracks
C_w	crack width
$\{d\varepsilon\}$	differential strain vector in material coordinates: $d\varepsilon_1$, $d\varepsilon_2$, $d\gamma_{12}$ in local (element) coordinates: $d\varepsilon_x$, $d\varepsilon_y$, $d\gamma_{xy}$
$\{d\sigma\}$	differential stress vector in material coordinates: $d\sigma_1$, $d\sigma_2$, $d\tau_{12}$ in local (element) coordinates: $d\sigma_x$, $d\sigma_y$, $d\tau_{xy}$
$[D_S]$	secant constitutive matrix
$[D_T]$	tangent constitutive matrix
E	Young's modulus
E_i, E_1, E_2	secant modulus of equivalent uniaxial stress-strain curve, direction i
E_1, E_2	tangent stiffness in direction of material axes
E_t	slope of linear descending branch of tensile stress-strain curve

f'_t	concrete tensile strength
G	shear modulus
G	energy release rate
G_c	critical energy release rate
G_f	fracture energy
h	element width
{IF}, $\{IF_S\}$	vector of nodal forces required to maintain an element or structure in its deformed configuration
K_I, K_{II}	fracture toughness parameter for Mode I or Mode II deformation
K_c	critical stress intensity factor under plane stress conditions
K_{Ic}	critical stress intensity factor under plane strain conditions
$[K_T]$	tangent structure stiffness matrix
{P}	total nodal load vector
{R}	residual nodal load vector
{U}	total nodal displacements
w	width of crack front
α	crack angle, measured from horizontal axis
β	shear stiffness retention factor
δ_f	summation of openings of individual microcracks in element

$\Delta\varepsilon_{cr}$	change in strain due to closing of microcracks
$\Delta\varepsilon_{iu}$	total change in equivalent uniaxial strain during load increment
$\{\Delta P\}$	vector of incremental nodal loads
$\{\Delta U\}$	vector of incremental nodal displacements
$\{\varepsilon\}$	vector of strains at a point in material coordinates: ε_1, ε_2, γ_{12} in local (element) coordinates: ε_x, ε_y, γ_{xy}
ε_{env}	envelope strain from which unloading occurs
ε_f	strain due to opening of microcracks
ε_{iu}	equivalent uniaxial strain in ith direction
ε_{iu}^{beg}	total equivalent uniaxial strain at beginning of load step
ε_{iu}^{new}	total equivalent uniaxial strain for current iteration
ε_0	equivalent uniaxial strain at which microcracks no longer transfer stress
μ	E_i/E, ratio of current secant stiffness in direction i to Young's modulus
ν	Poisson's ratio
$\{\sigma\}$	vector of stresses at a point in material coordinates: σ_1, σ_2, τ_{12} in local (element) coordinates: σ_x, σ_y, τ_{xy}